SCHOOL OF MECHANICAL, INDUSTRIAL & AERONAUTICAL ENGINEERING

Tailoring Surface Finish and Residual Stress Profile of Aeronautical Additive Manufactured Parts by Laser Shock Peening

Laveshan Nayager

(Student number: 0309230H)

School of Mechanical, Industrial and Aeronautical Engineering

University of the Witwatersrand

Johannesburg, South Africa

Supervisor: Prof. C. Polese

A research **dissertation** submitted to the Faculty of Engineering and the Built Environment, University of the Witwatersrand, in fulfilment of the requirements for the degree of Master of Science in Engineering

October 2021

Declaration

I declare that this dissertation is my own unaided work. It is being submitted to the Degree of Master of Science to the University of the Witwatersrand, Johannesburg. It has not been submitted before for any degree or examination to any other University.

……

Signature: Laveshan Nayager

……15…….day of the month of……October……of the year of…2021……..

Abstract

This project was aimed at the advancement of the Laser Shock Peening (LSP) process for additive manufactured aluminium alloy, specifically AlSi10Mg, for aeronautical applications. The samples that were manufactured by Additive Manufacturing (AM) Selective Laser Melting (SLM) had thicknesses of 1.2, 2.6, 5.6, 9.6, and 13.6 mm and were then surface treated with LSP. The samples were treated with 3 different Power Intensities (PI) of 1.5 GW/cm^2, 3.0 GW/cm^2, and 4.5 GW/cm^2, with a fixed round spot size of 1 mm diameter and 80% coverage. It was found that there was an increase of the average surface roughness (Ra) from approximately 1.66 µm for the as-built AM samples to 3.77 µm for the AM and LSP'ed samples, and an increase of surface roughness with an increase in PI of the LSP was observed. However, the published data for surface roughness for AM aluminium alloy AlSi10Mg indicate a value of about 6-8 µm. The surface and the cross-section of the AM AlSi10Mg samples post-processed by LSP was characterized using optical and Scanning Electron Microscopy it was found that there were defects, such as cracks, pores and solidification of material that had not melted correctly, within the cross-section of the material for the as-built AM samples and the AM and LSP'ed samples. The published data of as-built AM aluminium alloy AlSi10Mg has a Vickers' hardness of 124Hv at 500 gf. The microhardness close to the surface of the AM aluminium samples that had undergone LSP experienced an increase of 33% for PI of 1.5 and 3.0 GW/cm^2 and an 18% increase in microhardness for a PI of 4.5 GW/cm^2 in comparison to the as-built AM sample. The Incremental Hole Drilling (IHD) technique was used to measure the residual stress of the as-built AM AlSi10Mg samples with different thicknesses and after LSP processing. The maximum tensile residual stress of the 9.6 mm thick as-built AM sample was 237.78 MPa. After LSP, the change in residual stress from tensile to compressive was 143% for a PI of 1.5 GW/cm^2, 165% for a PI of 3.0 GW/cm^2 and 183% for a PI of 4.5 GW/cm^2 for a 9.6 mm thick sample. The results compared favourably between the as-built samples and the peened samples concluded that LSP has not only the beneficial effect of removing the tensile residual stress of the as-built AM samples but also inducing compressive

residual stress. A clear trend of the curve of the residual stress depth profile after peening had shifted upward, which is attributed to the fact that there is less elastic material to respond to the plastic deformation induced by LSP. This corresponded to the trend for AA7075.

Dedication

In memory of my late father

Vinayagum (Brian) Nayager

Acknowledgements

It is inadequate to describe the contribution, support and assistance of the following people with a few sentences however I will attempt to do so. I will begin by thanking my supervisor Professor C. Polese, of the University of the Witwatersrand, whose assistance, guidance and wonderful personality, without which this project would not have been possible. Professor J. Nobre, of the University of the Witwatersrand, for his expert knowledge in Incremental Hole Drilling and stress calculation methodology, was invaluable for this project. Dr D. Glaser, of the Centre for the Scientific and Industrial Research (CSIR), for his input with regards to LSP and peening parameters. Mr C. Schulte-Brader and Mr M. Mistry, of the University of the Witwatersrand, for their assistance with the LSP processing of the samples and overall willingness to assist with any task required. Mr T. Strydom, of the University of the Witwatersrand, for his help with the optical microscope and the scanning electron microscope. Mr S. Moqabulane, of the University of the Witwatersrand, for his assistance with the microhardness testing machine. Ms P. Dinham for her expert knowledge in using the field-effect scanning electron microscope. Mr G. Lombard from Metal Heart manufactured the samples for this project. I must also thank the laboratory workshop staff who manufactured critical components for this project, Mr S. Riekert for manufacturing the baseplate for the samples to be printed on. Mr F. Pietra for his assistance throughout the project and his invaluable insights and inputs into the project.

Mrs Marina Labuschagne of the DSI-NRF CoE-SM, for her kindness in assisting me with administrative matters. The Centre for Scientific and Industrial Research - National Laser Centre (CSIR NLC) Rental Pool Programme (RPP), funded by the DSI. The DSI Collaborative Program in Additive Manufacturing (CPAM), the implementation programme for the South African Additive Manufacturing strategy, for the supporting research funds. Lastly, but hardly the least, I would like to thank my family for their support throughout this project.

Table Of Contents

List Of Figures

List Of Tables

Nomenclature

The units of quantities defined by a symbol are indicated in brackets following the description of the symbol. Quantities with no indicated units may be assumed to be dimensionless.

Ra	Average surface roughness (µm).
ε	Strain.
σ	Stress (MPa).
ν	Poisson's Ratio.
D	Strain Gauge Rosette Diameter [mm].
E	Beam Energy [J].
E	Young's Modulus [MPa].
PI	Power Intensity [GW/cm^2].
SS	Spot Size [mm].
AM	Additive Manufacturing.
ASTM	American Society for Testing and Materials.
CSIR	Council for Scientific and Industrial Research.
Cv	Coverage.
Hv	Vicker's Hardness.
IHD	Incremental Hole Drilling.
LSPwC	Laser Shock Peening without Coating.
LSP	Laser Shock Peening.
NLC	National Laser Centre.

PI	Power Intensity.
SLM	Selective Laser Melting
SEM	Scanning Electron Microscope.
SP	Shot Peening.
SS	Spot Size.

Preface

This dissertation is divided into 7 chapters and begins with chapter 1 by discussing the different processes of Additive Manufacturing, problems associated with additive manufacturing and post-process treatments such as Laser Shock Peening. Different experimental characterisation methodologies are presented in Chapter 1, such as surface roughness, optical microscopy, scanning electron microscopy, microhardness testing and residual stress measurement methods. The problem statement, research questions, and objectives are provided in Chapter 2. Chapter 3 provides the research methodology, experimental equipment description, and operation. Chapter 4 provides the results of the as-built AM sample and the AM and LSP samples. A discussion of the results, conclusions, future work with recommendations, and contribution to knowledge are supplied in Chapters 5 through 8.

Chapter 1: Literature Survey

In this section different Additive Manufacturing (AM) processes are introduced, as well as the advantages and disadvantages of each process are listed. The aluminium alloy is also investigated and the post-processing treatments available for AM are discussed, primarily Laser Shock Peening (LSP). The experimental methods of surface roughness, optical microscopy, scanning electron microscopy, Vickers microhardness, used for evaluating the performance of the investigated processes, are also introduced. Residual stress and residual stress measurement methods, such as Incremental Hole Drilling, are discussed.

Chapter 1.1: Additive Manufacturing

Additive Manufacturing (AM) describes processes in which the part to be produced is constructed by the addition of material [1]. AM is the industrial production name for 3D printing, a computer-controlled process that creates three-dimensional objects by depositing materials, usually in layers [2]. Every layer corresponds to a section of a 3D CAD model of the product [3]. AM technologies require the material to be used, or the feedstock must be in a state compatible with the process being used, such as powder, sheet, wire or liquid [4].

Additive manufacturing processes are classified into seven areas based on:

- Type of materials used
- Deposition technique, and
- The way the material is fused or solidified

These classifications have been developed by the ASTM International Technical Committee F42 on additive manufacturing technologies [5]

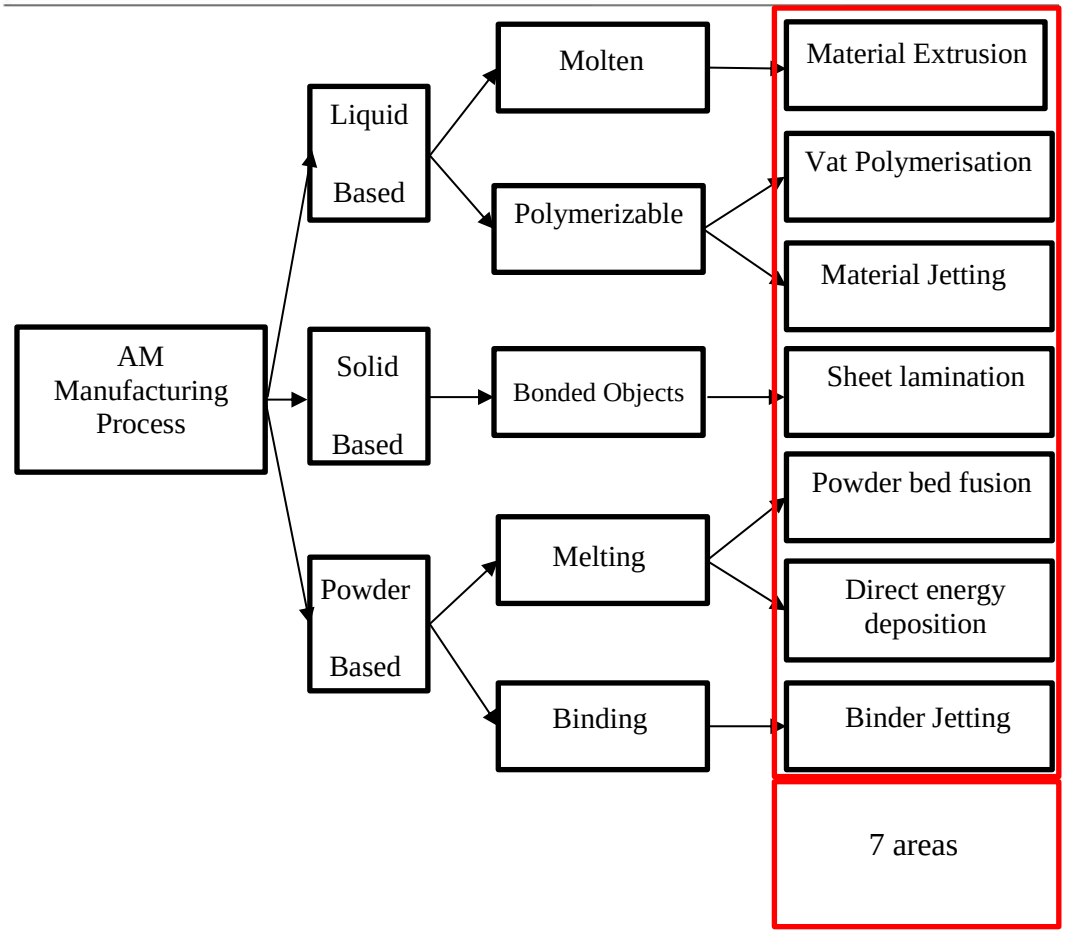

Figure 1: Classification of AM techniques *[5]*

AM processes always start the same way, with a CAD model which must be converted into a Stereolithography file (STL) and exported to the AM machine [6]. The purpose of the STL is to tessellate a solid body into triangles and generate a database of the triangular nodes. The AM machine then reads the STL file and then divides it into several layers. The part is then manufactured on a layer by layer basis until a full 3-D part is completed [3].

Some of the seven areas of the AM manufacturing process are listed in the sections below.

Chapter 1.1.1: Stereolithography (SLA)

Stereolithography (SLA) falls under vat polymerization and is one of the first technologies in the AM field [7].

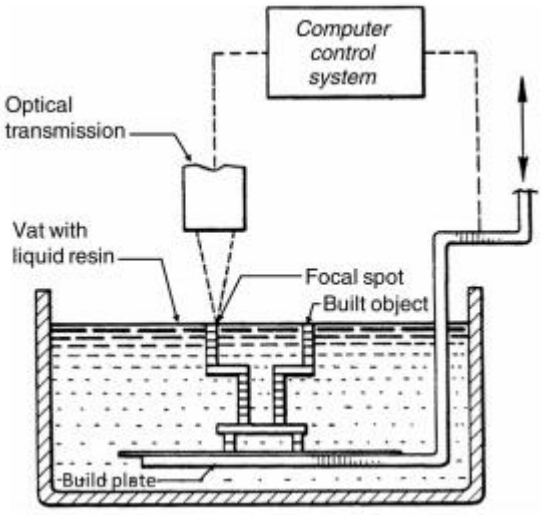

Figure 2: Schematic of stereolithography *[8]*.

A curable liquid is exposed to a pattern of laser to generate and solidify a layer of a cross-section of a 3-D part [8]. The generated layer of the 3-D cross-section is then lowered by the layer thickness, below the surface level of the liquid, and then a laser scans over the curable liquid to generate a new layer. By lowering the build plate the liquid is allowed to backfill for curing and bonding of subsequent layers. The process is then repeated until the full 3-D part is manufactured.

Chapter 1.1.2: Selective Laser Melting (SLM)

Selective laser melting (SLM) falls under powder bed fusion. Within an SLM machine, the confined build chamber is filled with metal powder, which is spread across a movable platform, in thin layers, by a recoater arm or roller [9]. A laser is scanned over the metal powder, using the lenses and the X-Y scanning mirror. The laser melts the metal powder which then fuses to create a layer. The movable platform is then lowered and the recoater arm then coats the layer with metal powder again before the process is repeated until a 3-D part is manufactured. This process is illustrated in figure 3.

Considering a layer that has been printed onto a previous layer of a sample, the second layer shrinks when it undergoes the phase change from liquid to solid, while the first layer underneath the second layer has already solidified. This solid first

layer constrains the second layer and prevents further shrinking which induces tensile residual stress within the second layer [10].

This happens to each layer of the sample being produced which results in large tensile residual stresses being induced throughout the sample. Typically, some processes are used after the manufacture of a sample to reduce the residual stress within a sample such as heat treating the sample for stress relaxation [11].

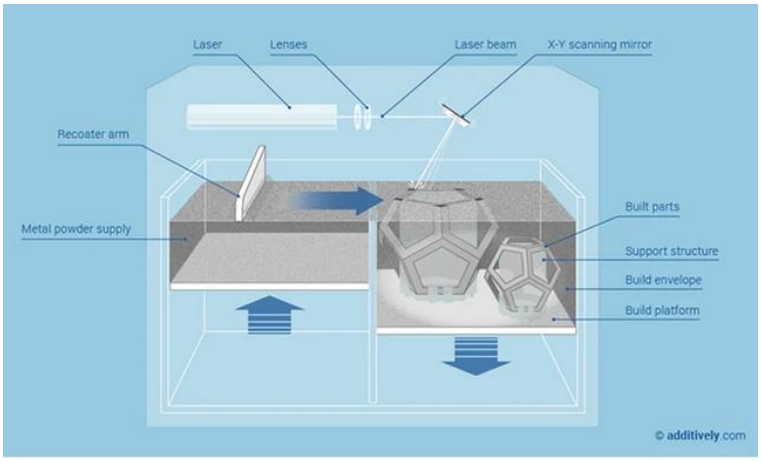

Figure 3: Selective laser melting process *[9]*

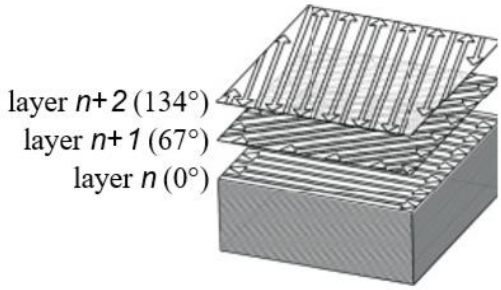

Figure 4: Layer build in AM *[10]*

In the figure above the different layers are shown with the rotation of the laser head by 67°. The reason for rotating the laser head by 67° is to reduce the tensile residual stress [12].

Chapter 1.1.3: Selective Laser Sintering (SLS)

Selective Laser Sintering (SLS) falls under powder bed fusion and is similar to SLM. SLS is used for plastics and glass. SLS uses the laser to melt and fuse the powders and then stack layer by layer to form a printed part based on 3D model data [13].

The difference between SLS and SLM is that sintering does not fully melt the plastic powder, but heats it to the point that the powder fuses on a molecular level whereas with SLM the metallic powder is melted into a homogenous material [14].

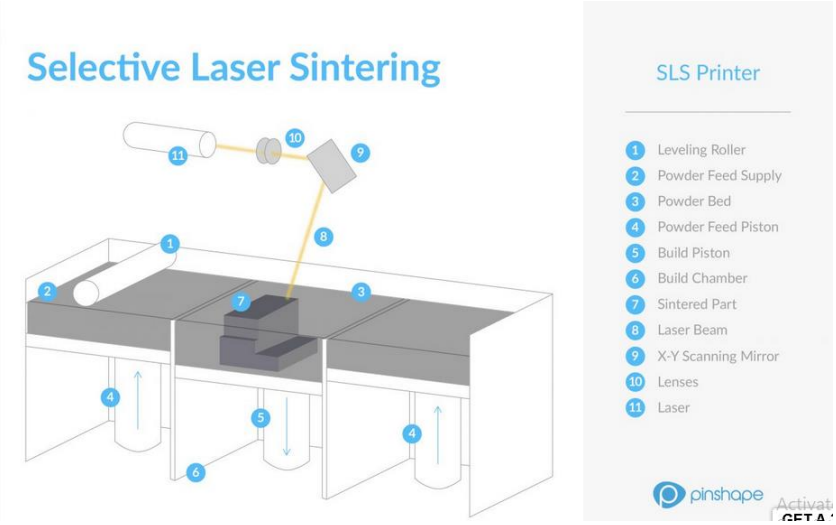

Figure 5: Schematic of SLS *[15]*

Chapter 1.1.4: Laminated Object Manufacturing (LOM)

The process of laminated object manufacturing (LOM) falls under sheet lamination. During the LOM process, layers of plastic or paper are fused, or laminated using heat and pressure, and then cut into the desired shape with a computer-controlled laser or blade [16]. It is possible to use any material in sheet form in LOM, such as metals and ceramics, if there is a suitable binding agent [7].

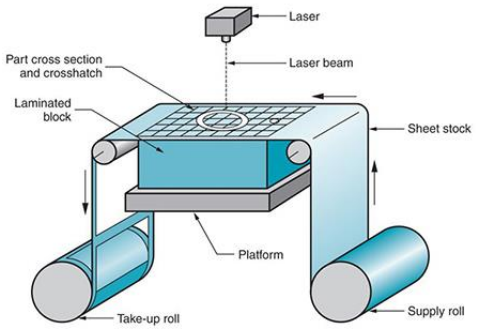

Figure 6: Schematic of laminated object manufacturing *[17]*.

Chapter 1.1.5: 3-D Printing

The process of 3-D printing falls under material jetting.

3-D printing has a powder within a build chamber that is supplied by a powder roller. An inkjet printhead supplies a liquid binder to the powder to form the 3-D part. The adhesive is removed by inserting the component in a furnace.

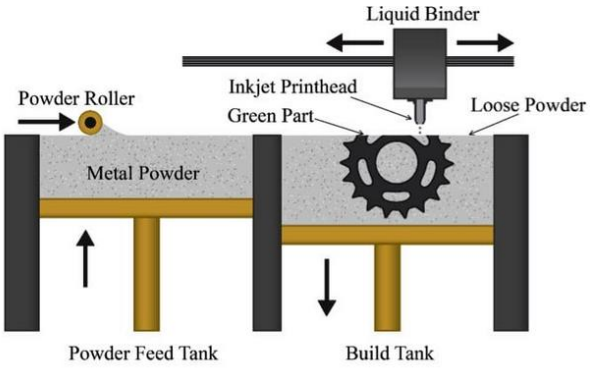

Figure 7: Schematic of 3-D printing process *[18]*

Chapter 1.1.6: Direct Metal Deposition (DMD)

The process of direct metal deposition (DMD) falls under direct energy deposition. An industrial laser beam under CNC/robotic control is focused over a metal base plate, producing a melt pool into which a small amount of powder metal is injected, building up the part in a thin layer [19]. The beam is moved to the next location based on CAD geometry, tracing out the part layer by layer without the need for additional manufacturing steps such as a recoating arm for powder bed dispensing.

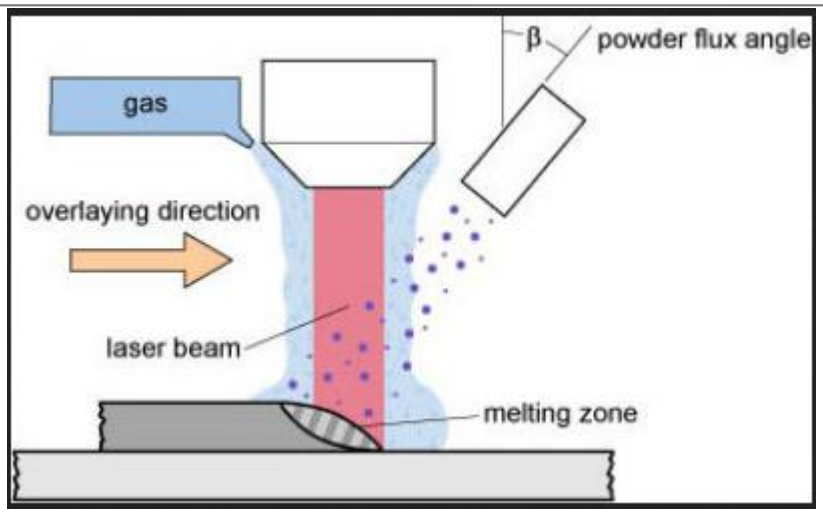

Figure 8: Schematic of direct metal deposition *[20]*.

Chapter 1.1.7: Advantages And Disadvantages Of AM Technologies

The advantages and disadvantages of each of the above technology are shown below.

Table 1: Advantages and disadvantages of different AM technologies *[3]*

No.	Technologies	Advantages	Disadvantages
1	Stereolithography	- Suitable for production of concept prototypes. - Fast processing times. - Good surface finish and geometrical accuracy.	- Limited to process non-functional materials, such as resins or plastics. - Resins are expensive and limited in availability. - Unable to process functional materials such as metals. - Requires support structure.
2	Selective laser melting	- Good geometric accuracy. - No support structures are required.	- The size of produced components are limited by the dimensions of the enclosing chamber. - The availability of materials is limited. - Slow build-up rate.

		- Suitable for processing metallic materials. - Produced components are suitable for functional use.	- Machining may be required for accurate dimensioning and surface roughness improvement.
3	Selective laser sintering	- Materials that can be processed are plastics, sands, glass and some metals. - No support structures are required. - Components produced are suitable for functional testing.	- The availability of metallic materials is low. - The size of produced components are limited by the dimensions of the enclosing chamber. - Metal sintering leads to porous and mechanically weak components.
4	Laminated object manufacturing	- Suitable for processing medium and large-sized components. - Wide choice of readily available materials in sheet form.	- Poor layer bonding carries the risk of delamination. - The strength of the components in the perpendicular direction to the layers is much less than in other directions. - Post-processing is required to improve surface roughness and geometric accuracy.
5	3-D printing	- High productivity - Good geometrical accuracy. - No support structures are required.	- Time-consuming post-processing is required. - Furnace heating is required to eliminate the adhesive. - Sintered parts are porous. - The mechanical strength of produced parts are low. - Limited choice of materials.

6	Direct metal deposition	- A layer can be fabricated in any orientation, - Variety of materials in powder form. - Large components can be manufactured. - Higher deposition rates are possible.	- Geometrical accuracy is low. - Post-processing options may be required.

Chapter 1.2: AM Alloys

The reason for alloying is that pure metals do not possess the desired applicability of physical and metallic properties such as melting point, density, specific gravity, high malleability, ductility, heat, and electrical conductivity, for certain purposes [21]. To improve these properties, alloying pure metals with other metals or non-metals can be done. The advantages of alloying are that it improves the hardness of a metal, lowers the melting point for easier fusibility, enhances tensile and corrosion strength [21].

One of the reasons for alloying in AM, specifically SLM are the castability and weldability of the material [22]. There are significant differences between these processes, such as the solidification rates associated with SLM are much steeper than those associated with casting. The repetitive melting and solidification experienced in the material during the SLM process are significantly different to those faced by the same material during laser welding [22].

Currently, only a few alloys, namely AlSi10Mg, TiAl6V4, CoCr and Inconel 718, can be reliably printed [23]. The reason why the vast majority of alloys commonly used in industry are not able to be used in the AM process is that the melting and solidification dynamics during the printing process lead to intolerable microstructures with large columnar grains and periodic cracks [24].

Chapter 1.3: Problems Associated With SLM

It has been observed that occasionally during the SLM process the material deforms, warps or cracks due to tensile residual stress that occurs during the manufacturing process [10]. The tensile residual stress is induced in the material when the material undergoes a phase change from liquid to solid. These tensile residual stresses are typically responsible for the detachment of the sample from the baseplate [25]. Large aerospace manufacturers using additive manufacturing presented the need for a more refined and enhanced surface finish on their AM parts, to improve aerodynamics [26]. Another concern with using AM alloys is the surface roughness of the part as it has a direct impact on a material's fatigue and stress corrosion cracking properties, to improve the material's surface roughness, typically reduction methods such as grinding, polishing and abrasive etching are used [27].

Chapter 1.4: Post-Processing Treatments

To remove high tensile residual stresses, some post-treatment processes are listed below.

- Post-process heat treatment

  The component is annealed in a furnace.

- Hot Isostatic Pressing Processing (HIPP)

  HIPP subjects a component to both elevated temperature and isostatic gas pressure in a high-pressure containment vessel. [28]

- Shot Peening (SP)

  Shot Peening is a cold working process used to produce a compressive residual stress layer and modify the mechanical properties of metals and composites. It entails impacting a surface with shot (round metallic, glass, or ceramic particles) with force sufficient to create plastic deformation. [29]

- Ultrasonic Shot Peening (USP)

Ultrasonic Shot Peening introduces beneficial compressive stresses into the component being treated at depths of 2 to 4 times that of traditional SP. As opposed to compressed air or centrifugal wheels, USP uses a mechanical vibration at ultrasound frequency (20 kHz) [30].

- Laser Shock Peening (LSP)

  Laser Peening (LP), or Laser Shock Peening (LSP), is a surface engineering process used to impart beneficial residual stresses in materials. The deep, high magnitude compressive residual stresses induced by LSP increase the resistance of materials to surface-related failures, such as fatigue, fretting fatigue and stress corrosion cracking [31].

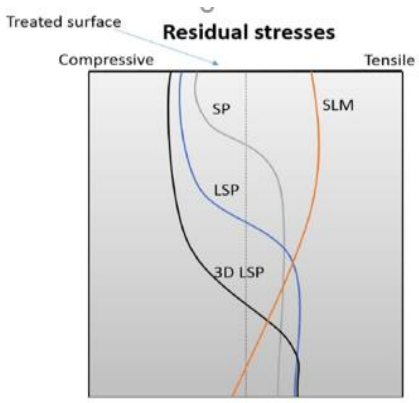

Figure 9: Schematic representation of residual stresses in SLM parts, showing the influence of shot peening, laser shock peening and 3D laser shock peening.

For this specific project, the post-processing treatment of Laser Shock Peening will be used and is described below. 3-D laser shock peening is out of scope for this work and will not be considered.

Chapter 1.4.1: Laser Shock Peening

This section describes a basic laser operation and its creation, as well as the laser shock peening (LSP) process. LSP is a surface treatment that is conceptually similar to Shot Peening and Ultrasonic Shot Peening, which are used to induce beneficial compressive residual stress [32].

The benefits of the LSP surface treatment is that the tensile residual stress within a sample may be entirely removed or reduced throughout the depth of several millimetres of the sample being processed [33].

The removal of the tensile residual stress also decreases the rate of crack propagation, which has an immediate effect on the fatigue life of the sample that has been produced [34].

The benefits of LSP has been investigated in depth for different materials, such as aluminium [35], titanium [36] and tool steels [37] to mention a few. It can be proven that the fatigue life of a sample can be directly related to the residual stresses and that compressive residual stress is beneficial to the material's mechanical properties [38].

The deeper the penetration of compressive residual stress, then the better performance of the material with respect to fatigue life [39].

The deeper the compressive residual stress is within the sample, the longer the interaction between the surface cracks and the layer cracks will be. The longer this interaction duration is then the slower the crack propagation and the better the fatigue life.

Chapter 1.4.2: Basic Description Of A Laser

In this section, the basic operation of a laser and how it is formed is described.

The term *laser* is an acronym for "light amplification by stimulated emission of radiation" [40].

This radiation is a form of light that is a single colour, the same wavelength and the waves are parallel. Such an ideal light would extend infinitely, however that is not possible due to diffraction [41]. To generate a laser with high pulse energy and duration a solid crystal or gain medium is chemically doped to emit light waves that are required for experimentation [42]. One of the most commonly used types of laser is Nd: YAG (neodymium-doped yttrium aluminium garnet) [43] and Nd: glass

(neodymium-doped glass) [44]. The Nd: YAG type will be under consideration for this project.

Figure 10: Quanta Ray, green laser *[45]*

The laser in the figure above produces a beam at a wavelength that corresponds to green light, hence the term "green" laser. The specific laser used for the processing of samples is a near-infrared 1064 nm, 20Hz laser, with a similar setup as the one above.

Chapter 1.4.3: Laser Shock Peening Parameters

To have successful LSP on a material, the laser beam, absorbent and transparent overlays must be characterised. For the laser parameters the wavelength, the duration of the laser pulse, laser energy and the laser spot diameter must be known [46].

The most important LSP process parameters and equations are listed below. The Power Intensity (P.I.) (GW/cm^2) is expressed as a function of average power (P_{ave}), frequency (*f*), pulse time (p.t.) (s) and spot area (S_a)

$$P.I. = \frac{P_{ave}}{f \times (p.t.) \times S_a}$$

The pressure (P) (GPa) that is generated on the surface of the material is a function of the power intensity (GW/cm^2), the equation is listed below

$$P = 1.02 \times \sqrt{P.I.}$$

Inside the substrate, it has also been observed that the Hugoniot elastic limit of the material must also be taken into account for the material to yield plastically once the laser is applied to the material. This equation takes into account Poisson's ratio and the dynamic yield stress. The shock waves produce strain rates exceeding 10^6 s^{-1} within the target material. At such high strain rates, the material behaves differently than under a quasi-static state and exhibits an increase in yield strength. When the amplitude of the shock wave is greater than this dynamic yield stress, it results in plastic deformation [47].

$$H.E.L = \frac{1-\nu}{1-2\nu} \times \sigma_y^{dynamic}$$

The coverage of the LSP is characterised as a function of the spot size area (S_a) and the pulse time (s). The coverage (C_v) determines how much the spots overlap with each other.

$$C_v = 1 - \frac{S_a}{\sqrt{p.t.}}$$

Chapter 1.4.4: Effects Of LSP On Materials

LSP imparts a load on the treated sample that is above the yield strength of the material. This causes strain hardening to occur and plastically deforms the sample and causes a residual stress field to be established and alters the surface morphology at the treated area [48]. It has also been found that the depth of penetration of LSP is by far deeper than other processes such as Shot Peening [49].

In 2018, research was carried out on the effects of LSP on aluminium alloy 7075 at the University of the Witwatersrand [48]. In the research samples of aluminium alloy 7075 with thicknesses of 1.6, 3, 6, and 10 mm were peened with LSP parameters of power intensity of 1.5, 3 and 4.5 GW/cm^2, a spot size of 1 mm diameter and coverage of 70 % with a peened area of 13 mm x 13 mm. The residual stress of the peened samples was measured using multiple methods, such as Incremental Hole Drilling, Neutron Diffraction, Synchrotron Energy-Dispersive X-Ray Diffraction, Laboratory XRD and Synchrotron Angle-Dispersive XRD. The

parameters of the previous research formed the basis of this dissertation with the use of LSP parameters and thickness of materials as well as the size of the samples that were printed.

Chapter 1.5: Surface Roughness

The measurement of the surface roughness of a material is important as it has a direct correlation to the crack propagation on the surface of a material. Typically, the profile roughness parameters R_a illustrated in Figure 11, and the arithmetic average of the deviation from the mean of the profile of the surface R_z. R_a is expressed mathematically by the equation below [50] and is used to characterise the surface of a sample.

$$R_a = \frac{1}{L}\int_0^L |f(x)|dx$$

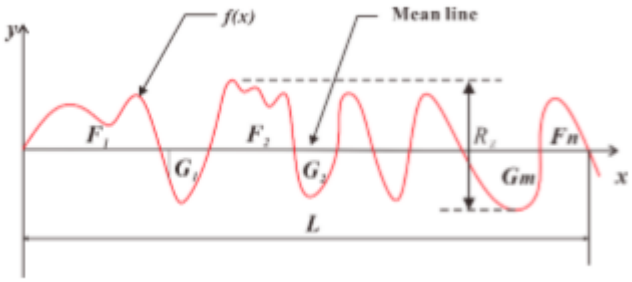

Figure 11: Surface roughness profile *[50]*

AM parts are often built with high surface roughness, which necessitates some post-processing steps to refine the resultant roughness and makes it suitable for a wide range of engineering applications [51]. One of the proposed surface treatments for surface roughness improvement is Laser Shock Peening, which is an innovative surface enhancement technology, without any surface preparations [52].

It has been found that the surface roughness of AlSi10Mg, increased from an as-built sample of average surface roughness (Ra) of 0.336 µm to a value of 14.501 µm for a peened sample. The PI of the LSP was 6 GW/cm^2, with a spot size of 0.8 mm diameter and coverage of 90 % [53].

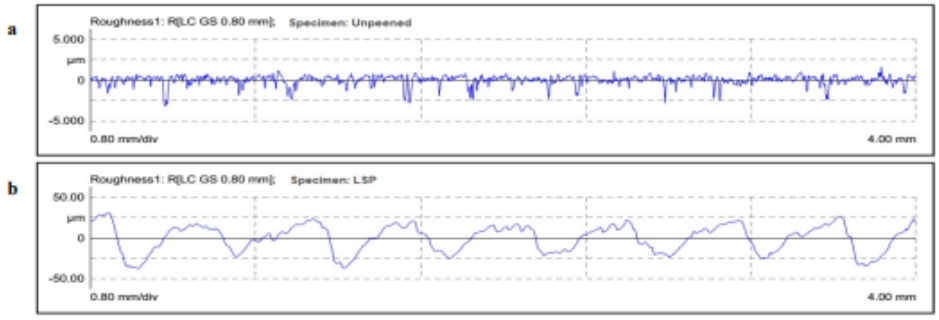

Figure 12: Surface roughness profile for (a) as-built and (b) peened samples *[53]*.

From previous work conducted at the University of the Witwatersrand, the surface roughness of AA7075-T6 before and after LSP is shown with the PI of 1.5 and 3 GW/cm^2 [48].

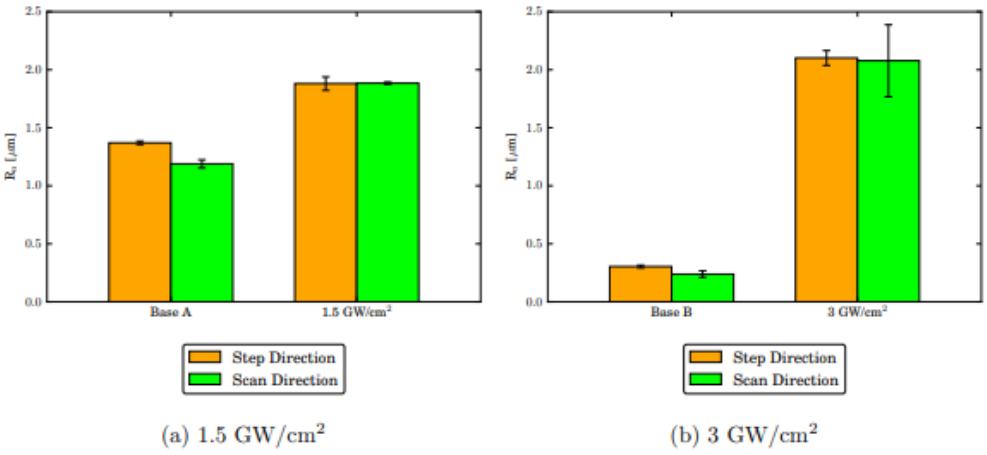

(a) 1.5 GW/cm^2 (b) 3 GW/cm^2

Figure 13: Surface roughness of AA7075 before and after LSP *[48]*

Chapter 1.6: Optical Microscopy

With optical microscopy, it is possible to magnify the surface of any material which will provide information on the grain size and lattice structures of the material, which are important to the mechanical properties of a material.

An image of a typical optical microscope is shown in Fig. 14. This setup provides the real-time capture of images which are then converted to digital media for processing.

Figure 14: A modern microscope with a mercury bulb for fluorescence microscopy. The microscope has a digital camera and is attached to a computer *[54]*

Typical images produced from optical microscopes are shown in Fig. 15 [55]. This image is for a common 3-D printing alloy, AlSi10Mg, and shows the pores that are formed after manufacturing. With these types of images, it is possible to observe microscopic cracks which can lead to fatigue failure.

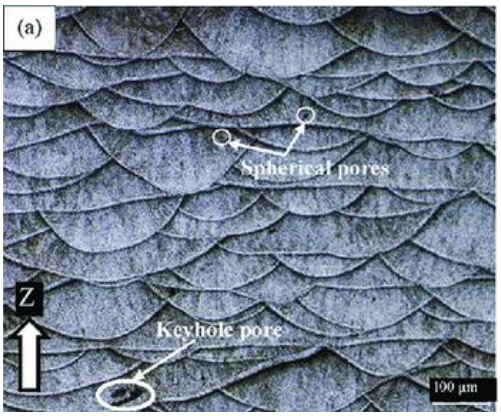

Figure 15: Optical microscopy image of as-built AlSi10Mg *[55]*.

It has been found that the microstructure of a cross-sectional LSP surface, the PI of the LSP was 6 GW/cm^2, a spot size of 0.8 mm diameter and coverage of 90%, shows semi-circular microstructure in a repeatedly curving pattern at a magnification of 20X. Due to the laser beam energy on micro parts of the Al matrix, there was uniform diffusibility of the metal atoms.

Comparing Figure 16 (a) to Figure 16 (b), there appears to be grain refinement at a micro-level. This is due to the effect of shock waves produced during laser shock peening. Due to these grain refinements, grains are divided into micro grains and

are closely packed. The presence of closely packed grains has the effect of improving microhardness in the sample [53].

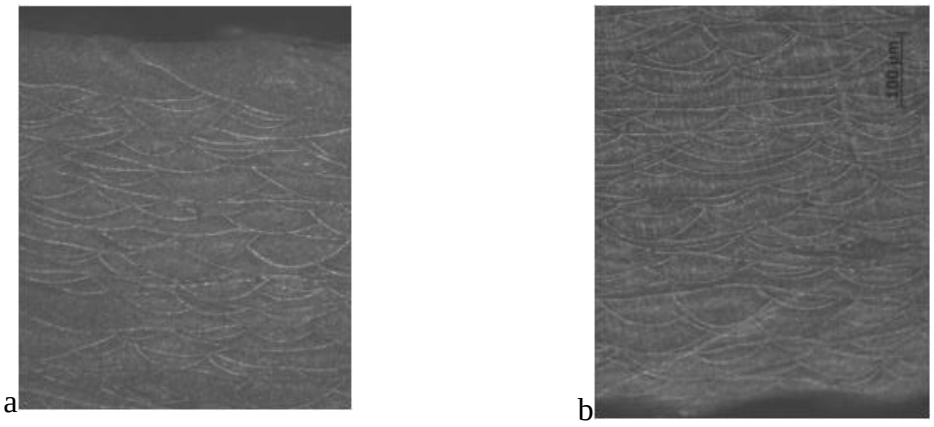

Figure 16: Cross-sectional optical microscopic images of as-built (a) and peened sample (b) *[53]*

Optical microscopy images of AA 6065, unpeened and LSP'ed are shown below. The author peened the sample at a PI of 1.5 GW/cm^2, with a spot size of 2 mm diameter and coverage of 50% [56].

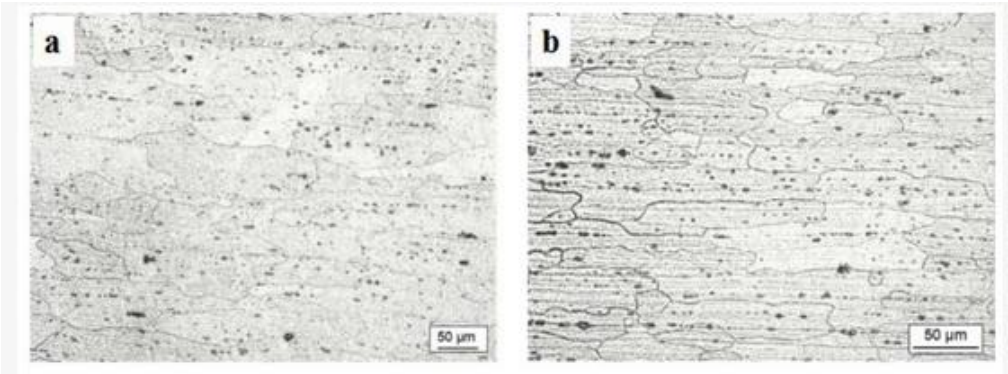

Figure 17: Optical microscopy of AA6065, un-peened (a) and LSPeened (b) *[56]*

The author noted that the grain size of the un-peened sample was larger than the peened sample. The average size of the grains was 200 µm for the un-peened sample and the LSPeened sample was approximately 150 µm [56].

Chapter 1.7: Scanning Electron Microscope

There is a limitation on optical microscopy magnification due to the diffraction of light [57]. An option to overcome this limit and increase the magnification is a Scanning Electron Microscope (SEM). An SEM is a microscope that scans the surface of the material under observation with a focused beam of electrons. This beam of electrons interacts with the atoms within the material to produce different signals. The signals are then correlated with the surface topology and the material composition [57]. To produce an image, the intensity of the signal, position of the beam and the scanning pattern is required [57].

It is possible to measure the residual stress of a sample using an SEM by making use of the electron back scattering method however, this is out of the scope of this project. Readers are advised to refer to [58] to learn more about this method.

Comparing the resolution of an SEM to XRD and IHD in terms of depth it is observed that the SEM can get closer to the surface of a sample as opposed to IHD, this is illustrated in Figure 18.

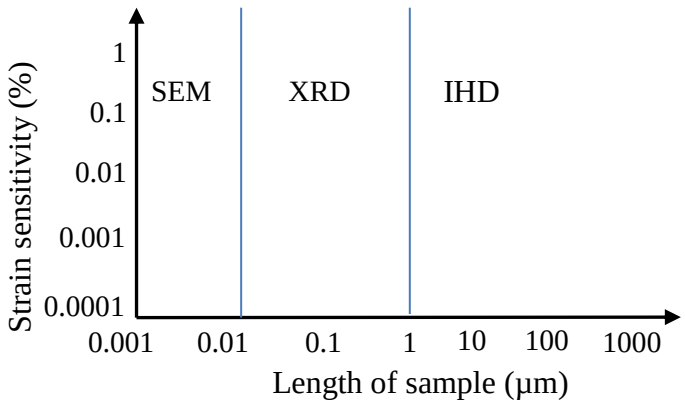

Figure 18: Resolution of different RS methods

Readers are advised to refer to [59] for an understanding of the effects of LSP on the microstructure of a sample.

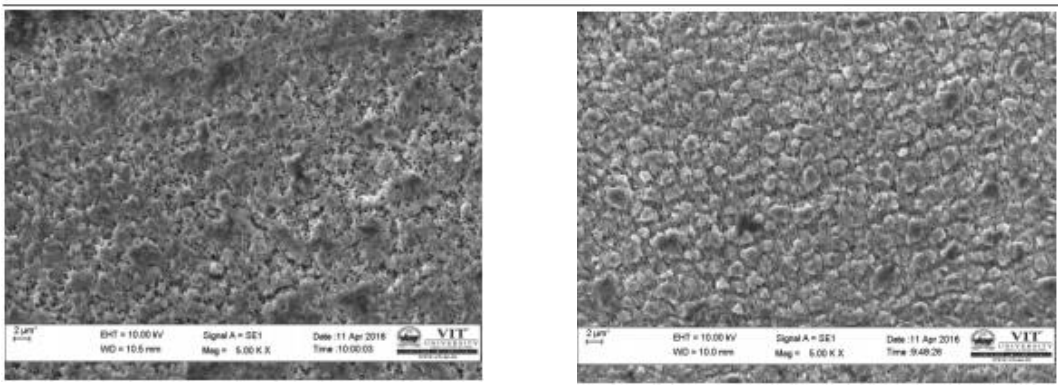

Figure 19: SEM of top surface of the as-built sample (a) and LSPeened sample (b) *[53]*.

Figure 19 shows the SEM images of an as-built and LSPeened sample, the PI of the LSP was 6 GW/cm^2, a spot size of 0.8 mm diameter and coverage of 90%. It is observed that the larger grains in the un-peened sample have been refined to micro grains after LSP. In the as-built sample, the grains appear to be in a seaweed structure with high porosity. The refinement is due to severe plastic deformation induced by LSP [53]. There appears to be a reduction in porosity in the peened sample due to an increase in dislocation density. After LSP, there appear to be particles that are overcrowding with a precipitate of metal atoms in an island of micro atoms in the Al matrix. During LSP the surface melts and re-solidifies while cooling. This phenomenon takes place in a region less than 1 micrometre from the surface. The LSP layer appears to be different from the normal surface due to shock wave compression. [60] Observed that the improvement of surface characteristics such as hardness was due to the solidified ablated surface after LSP.

A study of the effects of LSP on AA6061-T6 was conducted and the SEM images of the top surface of the samples are shown in Figure 20 [61]. The LSP was conducted at 6 GW/cm^2, 0.8 mm diameter spot size and coverage of 11 %.

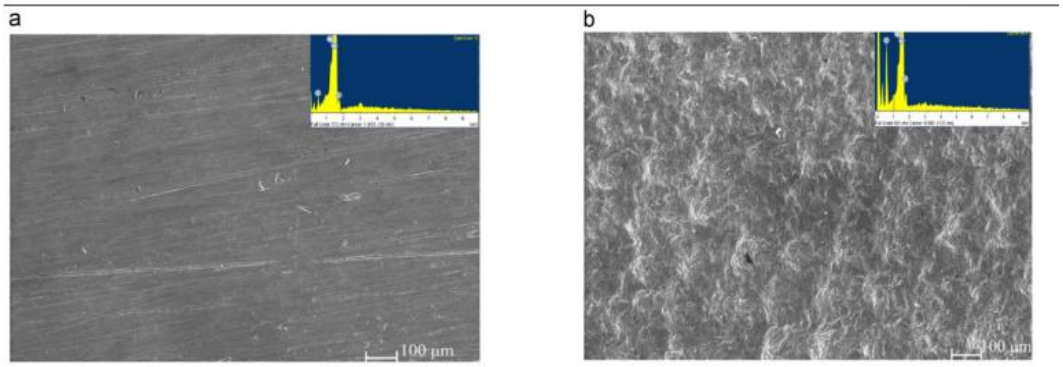

Figure 20: SEM of the surface of AA 6065 un-peened (a) and LSPeened (b) *[61]*

The author noted that the un-peened surface was relatively smooth in comparison to the peened surface as well as there was no appearance of micro-cracks on the peened surface, which had been previously reported in the literature [61].

Chapter 1.8: Microhardness Testing

The mechanical hardness of a material is a measure of the resistance to localized plastic deformation induced by either mechanical indentation or abrasion [62]. Material hardness is dependent on many material properties such as ductility, elastic stiffness, plasticity, strain, strength, toughness, viscoelasticity, and viscosity. [63]. There are different types of hardness measurements such as scratch, indentation and rebound hardness.

For this project specifically, indentation hardness is the focus and measured via the Vickers microhardness testing method. The Vickers hardness testing calculation method is independent of the size of the indenter and the indenter can be used on all materials irrespective of hardness [64].

The underlying principle of testing is to observe the material's ability to resist the plastic deformation to an applied load from the indenter and is measured in Vickers pyramid number (Hv). This hardness value should not be confused with a pressure value even though the value can be converted to a Pascal number. The reason for this is that the hardness value is calculated from the load over the surface area of the indentation and the area of the indentation, which is not the area *normal* to the force applied [65]. LSP has an effect of improving a materials microhardness. It has

been found that the metal microhardness can be significantly increased to more than 80% for AA7075 by increasing the laser intensity and the number of laser shots irradiated per unit area [66]. Please refer to Figure 22 for an illustration of this.

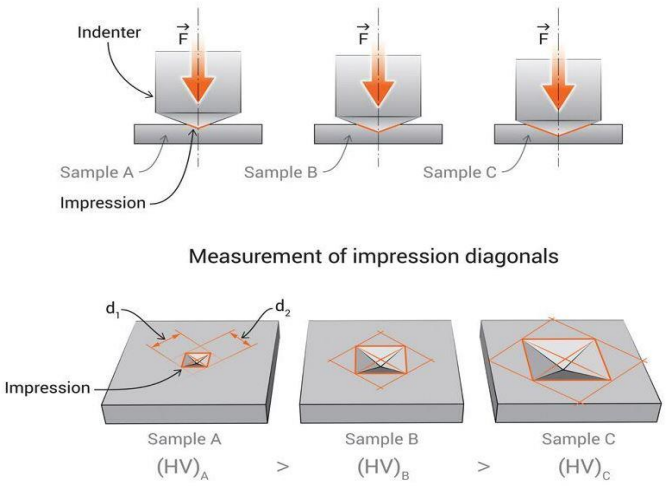

Figure 21: Vickers hardness test indenter *[65]*

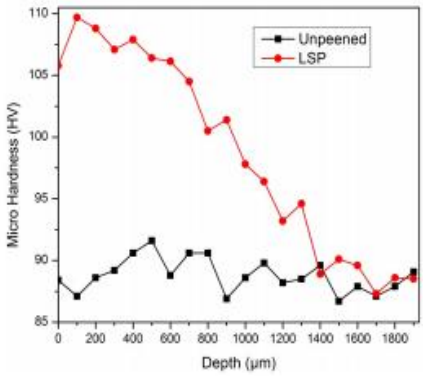

Figure 22: Vickers microhardness for AlSi10Mg as-built and peened sample *[53]*.

The average microhardness of the AM AlSi10Mg as-built sample was found to be 88.79 Hv at 200-gram force (gf) with a dwelling time of 10 seconds and 5 seconds for loading and unloading. Depth wise microhardness was measured for twenty indentations (100μm apart) and the same was repeated five times at different positions from the laser-ablated surface. The average value of microhardness implies that there is an effect of work hardening due to laser shock peening, the PI of the LSP was 6 GW/cm^2, a spot size of 0.8 mm diameter and coverage of 90%. The maximum value of micro-hardness is 109.7 Hv which is obtained at a depth of

100µm from the surface (indicating an increase of 22.6 Hv from the as-built surface which is 25.9% higher). The effect of work hardening due to LSP is found till a depth of 1300 µm from the surface as shown in the figure above [53].

The microhardness of AA 6065-T6 for an un-peened and peened sample is shown below. The LSP parameters were 6 GW/cm^2, a spot size of 0.8 mm diameter and coverage of 11 % [61].

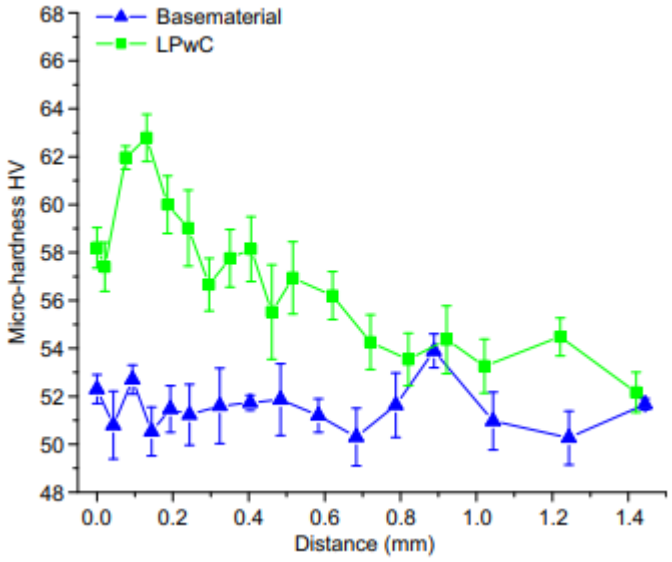

Figure 23: Microhardness of AA6065-T6 *[61]*

The author reported that there was an increase of approximately 10 Hv near the surface of the peened sample in comparison to the un-peened sample.

Chapter 1.9: Residual Stress

It has been previously noted that if a material is loaded beyond the yield strength of the material then there will be permanent deformation of the material. Once the material is unloaded, this permanent deformation results in stress within the material, this stress is termed *residual stress* and has an impact on the material characteristics. An understanding of residual stress is important as they arise after the material has exited a machining process to become the final product. Examples of finished products are turbine blades, connecting rods between the cylinder and the crank shaft within an engine block, among others.

Noting Figure 24, where the material is loaded beyond the yield strength and then unloaded, the following stress-strain diagram becomes relevant.

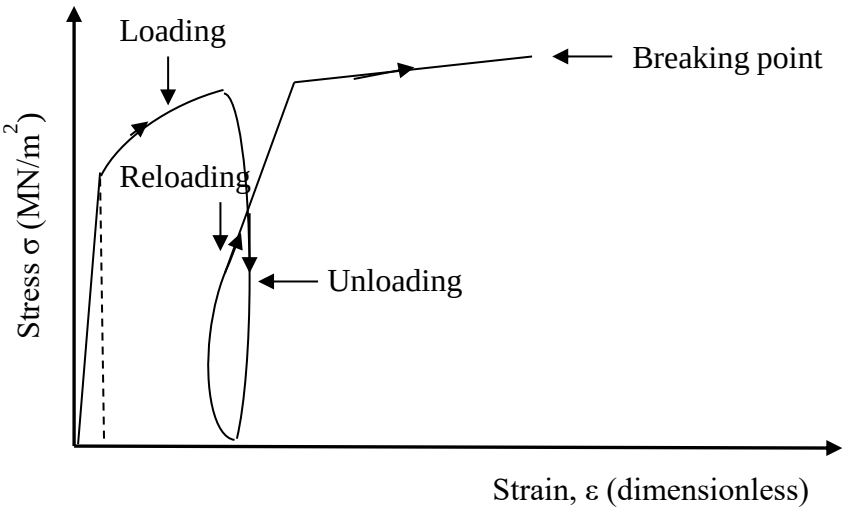

Figure 24: Loading and unloading of a material in the inelastic region [1]

There are typically three types of residual stress which are measured according to length. These types are listed below:

- Type I – Macro residual stresses which are developed larger than the crystal structure of the material
- Type II – Micro residual stresses which are developed on the crystal structure of the material
- Type III – The residual stresses that are on the atomic level of the material.

Chapter 1.9.1: Residual Stress Measurements

Residual stress measurement techniques invariably measure strains rather than stresses, and the residual stresses are then deduced using the appropriate material parameters such as Young's modulus and Poisson's ratio [67].

There are many methods to measure residual stress and some are listed below.

- Hole Drilling Method

- X-ray Diffraction

- Electron Back Scattering

- Neutron X-ray Diffraction

The hole-drilling method is discussed in greater detail in the following section.

Chapter 1.9.1.1: Hole Drilling Method

The Hole Drilling Method (HDM) is a semi-destructive technique that is based on the elastic stress relief from material removal, namely a hole being drilled at the centre of a strain gauge rosette, which measures the relieved strain of the material and using the relationship between stress and strain, as well as various empirical coefficients, the residual stress at each depth of the hole drilled is calculated.

The HDM is relatively cheaper, quicker and more versatile than the above listed residual stress measurement techniques.

There is currently an ASTM standard that provides details about how to perform the HDM and how to select strain gauge rosettes [68].

The HDM is divided into three different sequential steps.

1) The hole is first drilled into the surface where the residual stress is to be measured via high-speed drilling.
2) The relieved strain from the material being removed is measured.
3) The residual stress is calculated by converting the measured strains via the material property relationships.

During this process, the diameter of the hole and the incremental depth of the hole are important parameters used to calculate the residual stress.

The ASTM E837-13a standard provides detailed lists of hole diameters and incremental hole depths. The standard also provides specifications for the types of strain gauges to be used, for the material being measured as well as the expected residual stress profiles that should be determined throughout the hole

Due to the relieved strains being measured at the surface of the material under consideration, there is a maximum depth at which the hole can be drilled before the

relieved strains can no longer be measured at the surface. A typical rule of thumb when measuring the residual stress is to drill to a depth of *half* the diameter of the hole being drilled.

The recorded strains are converted to maximum, most tensile (+), and minimum, most compressive (-), principal stresses:

$$\sigma_{max}, \sigma_{min} = -E\left[\frac{p}{\bar{a}(1+\upsilon)} \pm \frac{\sqrt{q^2+t^2}}{\bar{b}}\right]$$

where p, q, and t are combined strains calculated from the recorded strains. The calibration constants $\bar{a}$ and $\bar{b}$ are found from the tables provided in the standard and the relevant hole diameter. E is Young's modulus and ν is Poisson's ratio.

These principal stresses indicated if the residual stress was in compression or tension. Typically, a negative measured strain corresponds to tensile residual stress and a positive measured strain corresponds to compressive residual stress.

The strain gauge rosette used to measure the residual stresses in this project is shown below. The strain gauge selected is specifically used to measure aluminium as it takes into account the thermal expansion of the material while it is undergoing the drilling process.

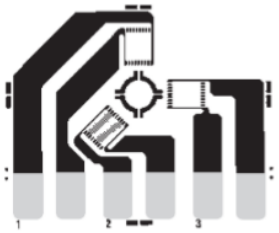

Figure 25: Strain gauge CEA-13-062UL-120 made by Vishay is an ASTM standard E837 Type A rosette

From literature, the residual stress of samples, with supporting structure and without supporting structure by SLM, was measured by Incremental Hole Drilling (IHD) [10] and is shown in Figure 26.

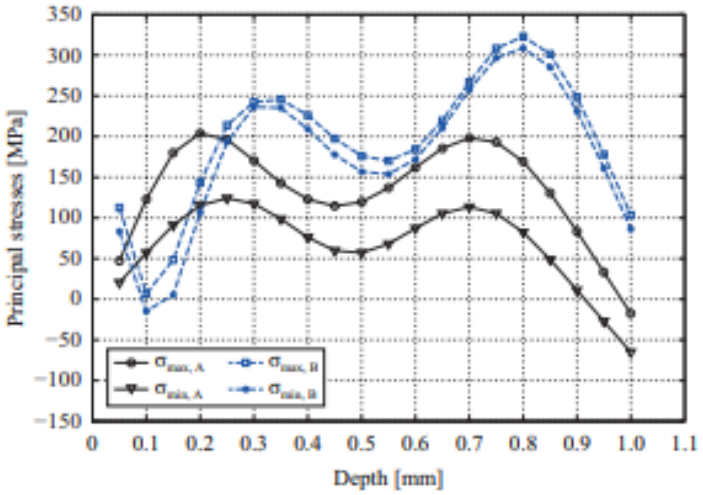

Figure 26: Residual stress measurement by IHD of AlSi10Mg *[10]*

Salmi et al. [10], noted that a sample built with supports by SLM (B), had a greater stress state than a sample without supports (A) in Figure 26. It was theorized that the sample without a supporting structure had a higher heat transmission during the SLM build (A), whereas the sample with the support structure (B) had a limited heat transmission due to the support structure. Due to the higher heat transmission for sample (A), the thermal gradient was lower and as a consequence, the residual stress state was lower.

In the previous work done at the University of the Witwatersrand, the residual stress of AA7075, which was LSP'ed with a PI of 3 GW/cm^2 was measured via IHD, and the results are presented below [48].

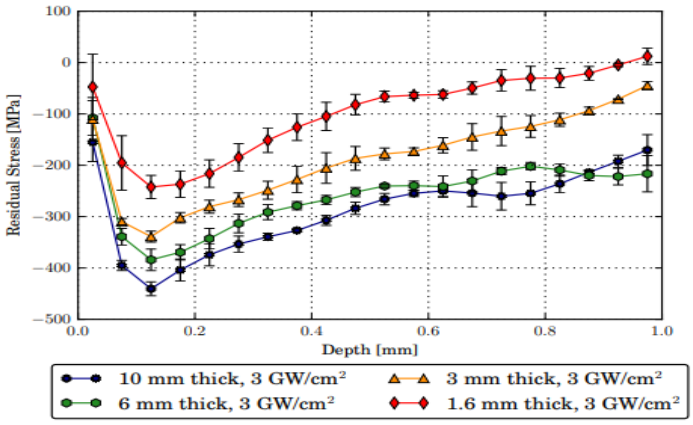

Figure 27: Residual Stress vs Depth for 10, 6, 3 and 1.6 mm Thick Samples Peened with a PI of 3 GW/cm^2 *[48]*.

The author noted that with a decrease in the sample thicknesses the curve of the residual stress shifted upward, which was attributed to the fact that there was less elastic material to respond to the plastic deformation induced by LSP which resulted in deformed samples with a lower magnitude of residual stress [48].

Chapter 2: Problem Statement, Research Questions and Objectives

In this section, the problem statement, research questions, and research objectives are provided.

Chapter 2.1: Problem Statement

Additive Manufacturing (AM), specifically Selective Laser Melting (SLM), has an inherent negative issue with high tensile residual stress and poor surface finish after manufacture. Laser Shock Peening (LSP) is a surface treatment that not only induces a compressive residual stress state of a component but can also improve the surface finish. It is possible to combine AM and LSP beneficially.

Chapter 2.2: Research Questions

1. To what extent can LSP be effective in reducing the surface roughness and tensile residual stress of an SLM sample?
2. If LSP is effective in reducing the surface roughness and tensile residual stress of an SLM sample, what are the LSP parameters that are most effective in doing so?

Chapter 2.3: Research Objectives

1. Define the surface integrity, microstructure, and residual stress field of the as-built SLM aluminium AlSi10Mg.
2. Define the surface integrity, microstructure, and residual stress field of the SLM and LSP aluminium AlSi10Mg.

3. Compare the surface integrity, microstructure and residual stress field of as-built SLM aluminium AlSi10Mg samples to the SLM and LSP aluminium AlSi10Mg samples.

Chapter 3: Research Methods, Experimental Equipment Description and Operation

In this section, the research method used is stipulated as well as the description and operation of the experimental equipment are provided. A description of the SLM machine used in the dissertation is provided. The aluminium alloy AlSi10Mg is discussed. The design of the experiment is provided and the LSP setup is described. A description of the surface roughness machine and corresponding equipment such as the sample sectioning machine and the hot mounting machine are provided. The grinding and polishing machine is discussed and a description of the optical microscope is provided. The field-effect scanning electron microscope (FESEM) is described along with the hardness testing machine. Finally, the incremental hole drilling (IHD) equipment is described.

The reasoning behind measuring the surface roughness is to find out if the LSP surface treatment had improved the surface roughness of the SLM samples. The results expected are that the surface roughness had increased according to the literature provided in section 1.5 [53].

The use of the optical microscope was to find the defects in the material after manufacturing by the SLM process, to observe the precipitates that had formed and the cracks that were induced in the samples by the manufacturing process. The results expected was a closer packing of the grains after the LSP of the samples, as noted in section 1.6 [53].

The FESEM was used to see the effect of the LSP on the samples at the surface of the material by observing the grain boundary of the affected region. The results expected was a notation of the different precipitates that had formed as well as clear imaging of the LSP area near the surface of the material, as noted in section 1.7 [53].

Microhardness testing was performed to observe the effect of the LSP on hardness through the depth of the sample in increments of micrometres. The results expected was an increase in hardness through the first 1000 µm as noted in section 1.8 [53].

The utilization of IHD was to observe the change in the residual stress state from an expected tensile residual stress state after manufacturing by SLM and then observe the samples after LSP which would have induced a compressive residual stress state in the samples as noted in section 1.9 [10].

Chapter 3.1: Research Method

The research methods used for this project are listed below.

1. Measure the surface roughness of the as-built AM samples and AM samples with various LSP parameters. Compare the average surface roughness data to published data.
2. Observe if there are any surface defects or features of the as-built AM samples and the samples processed with various LSP parameters.
3. Observe the grain structure of the as-built AM samples and the AM samples processed with various LSP parameters.
4. Measure the microhardness, specifically the Vicker's microhardness of the as-built AM samples and the AM samples with various LSP parameters. Compare the measured data to reference data.
5. Measure the residual stress profiles of as-built AM samples and AM samples with various LSP parameters, using Incremental Hole Drilling (IHD)

In this section, a description of the equipment used in this project is provided.

Chapter 3.2: Description Of The SLM Machine

Figure 28 illustrates the SLM process that was used for the manufacture of the samples required for this project. The baseplate was made of Aluminium 6082-T651. The decision of choosing this material as the base plate was for its weldability characteristics, for the AlSi10Mg to be printed onto the baseplate.

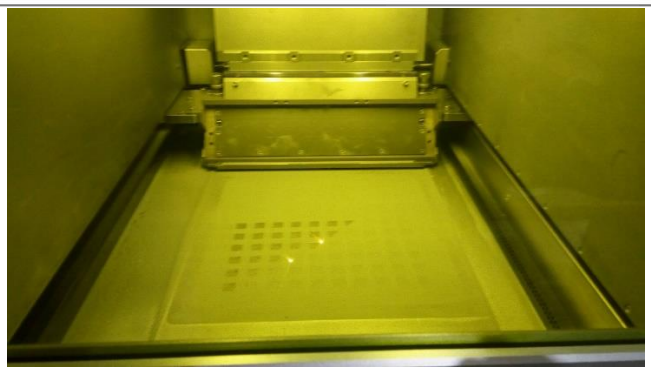

Figure 28: The 3-D printing process

The baseplate had to be manufactured to the size of the moveable surface with the specified bolt pattern from the manufacturer Metal Heart. Appendix A provides the manufacturing drawing of the baseplate with the thicknesses of the printed material. The thicknesses of the samples were 1.6, 3,6, 10, and 14 mm. The sample width and length were a square of 13 mm x 13 mm. The number of samples per thickness was 20. The reason for selecting these dimensions of thicknesses and length was due to the previous work carried out at the University of the Witwatersrand in 2019 on the effects of LSP on aluminium AA 7075 [48]. In the previous work aluminium samples of 1.6, 3, 6, 10, and 14 mm were LSPeened.

An image of the SLM machine that was used in this project is shown below. This machine is owned by a company called Metal Heart based in Roodeport, Johannesburg, South Africa. The project utilises an SLM solutions 280 2.0, machine to produce the required samples

Figure 29: SLM solutions 280 2.0 SLM machine *[69]*

Figure 30 shows the different compartments within the SLM 280 2.0 machine that was used. It is important to note that the build chamber has specific dimensions for the baseplate that cannot be exceeded. These dimensions were discussed in detail with the manufacturer.

Figure 30: SLM 280 machine with compartments open *[70]*

The parameters for the build are listed in Table 2

Table 2: SLM build parameters

Materials	AlSi10Mg
Layer Thickness	0.03 mm
Laser Power	Variable up to 400 W
Processing temperature	150°C
Processing pattern	Stripes
Laser scan speed	10 m/s
Beam focus diameter	80 µm

The laser speed, laser spot diameter, and scanning width of the machining parameters are automatically selected by the SLM 280 2.0 machine, for the 30-micron layer thickness of AlSi10Mg.

Figure 31 shows an image of the AM samples that were manufactured by Metal Heart for this research. The different thicknesses are shown as well as the baseplate. Readers are referred to Appendix A for the manufacturing drawing.

Figure 31: AM samples manufactured by Metal Heart

Chapter 3.2.1: Aluminium Alloy AlSi10Mg

In the automotive, aerospace and domestic industries, aluminium-silicon alloys have found a large number of applications [71]. The benefits of aluminium-silicon alloys are that they can be welded efficiently, the proficiency of casting is great and the alloy provides high corrosion resistance. After alloying magnesium to the Al-Si compound, the precipitation of Mg_2Si is possible. This precipitate strengthens the lattice matrix without decreasing the other benefits of the alloy, mentioned above [72].

The alloy for this research is AlSi10Mg, which has a weight percent of 0.20 – 0.45 of magnesium [73]. This alloy is suitable for Additive Manufacturing via selective laser melting (SLM) [73]. The benefit of using this alloy in SLM is that it provides the possibility to create complex components, such as heat sinks and lightweight applications [74].

The consequences of using this alloy in SLM are that the alloy is highly reflective and has a low melting point [74]. These negatives, adversely affect the SLM process.

The material properties for the alloy are presented in Table 3.

Table 3: Mechanical properties of SLM built parts and cast aged parts *[75]*

x ± s	E GPa	UTS MPa	break %	Hv
XY direction	68 ± 3	391 ± 6	5,55 ± 0,4	127
Z direction		396 ± 8 3	47 ± 0,6	
Conventional cast and aged	71	300-317	2,5-3,5	86

high pressure die casting F	71	300-350	3-5	95-105
high pressure die casting T6	71	330-365	3-5	130-133
SLM AlSi10Mg [73]	75	450	5	125

For this project, Young's modulus of elasticity used was 75 GPa and Poisson's ratio was 0.33. The yield strength was 275 MPa and the Ultimate Tensile Strength (UTS) was 450 MPa [73].

The powder used to produce the test samples was supplied by SLM solutions and has a composition of AlSi10Mg.

Chapter 3.2.2: Sample Design Of Experiment

The machine used the build parameters of laser power 400W, 30 µm layer thickness, a scan speed of 10m/s, beam focus diameter of 80 µm and the scanning strategy was stripes. The samples that were manufactured are square blocks of 13 x 13 mm with 5 different thicknesses of 1.2, 2.6, 5.6, 9.6 and 13.6 mm, as shown in Figure 32: Manufactured AM samples. The number of samples that were manufactured is 100 and the number of samples selected to be LSP'ed was 75, 25 for each LSP power intensity with 3 different power intensities of 1.5, 3.0 and 4.5 GW/cm^2. The total number of samples to be analysed are 20 (5 different thicknesses, 1 as-built sample per thickness and 3 LSP'ed samples per thickness) and the rest are to be kept as backup samples.

Figure 32: Manufactured AM samples

Chapter 3.3: Description Of The LSP Setup And The Procedure

The LSP was performed at the National Laser Centre (NLC) at the Centre for Scientific and Industrial Research (CSIR) in Pretoria, South Africa, under the Rental Pool Program agreement between the University of the Witwatersrand and the CSIR. The specific laser used was a Quanta-Ray Pro Spectra-Physics Nd: YAG laser with the specifications listed below

Table 4: Nd: YAG laser parameters

Wavelength [nm]	1064
Pulse frequency [Hz]	20
Energy Range [J]	0.2 – 1
Spot shape	○ (circle)
Spot size range [mm]	0.5 – 2.5

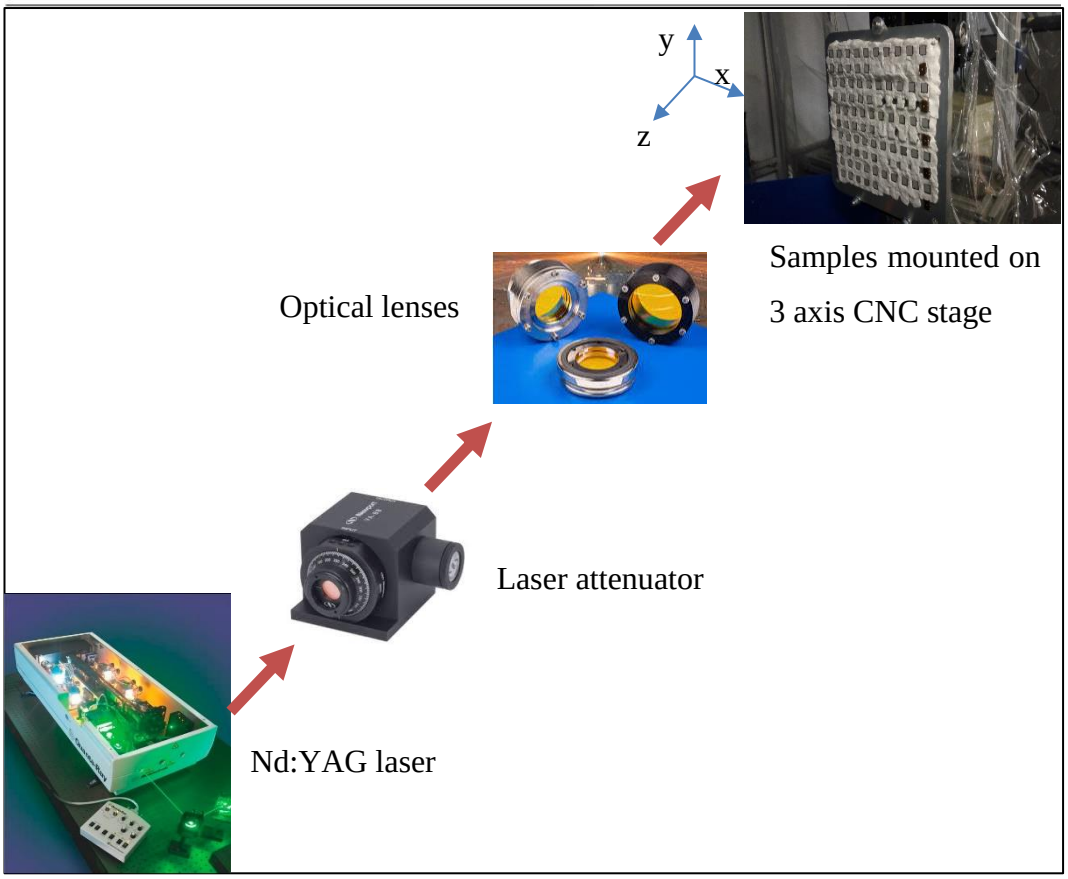

Figure 33: Schematic of LSP system

Figure 33 illustrates a schematic of the LSP system that was used. The energy of the laser, projected from the Nd: YAG laser, is varied to the desired value for experimentation by the laser attenuator. The attenuated laser beam then passes through a series of geometric optical lenses before impacting the surface of the samples. Since the laser is fixed, the samples are moved using a 3 axis CNC stage to get the desired laser peening pattern. The desired spot size for the experimentation is found by adjusting the z-axis of the CNC stage. The desired LSP pattern is performed by programming the CNC machine to move the sample in the X and Y directions of the 3 axis CNC stage.

Chapter 3.3.1: LSP Experimental Procedure

The following procedure was used to perform the peening of the samples.

1. Secure sample to the 3 axis CNC Stage.

2. Check the CNC code has the correct parameters entered into it. Save, build and load the code.
3. Set the laser to pulse and start the water flow and ensure that the water curtain is flowing smoothly over the sample.
4. Run the CNC code.
5. When the CNC code is completed, turn the water and laser off.
6. Adjust the CNC stage to the next sample to be peened.
7. Repeat the above steps for each sample with the correct thickness
8. Once the samples for the correct thickness are completed adjust the z-axis of the CNC stage to the correct focal length for the desired spot size. Then repeat steps 1 through 7.

The following are the precautions taken to ensure that the LSP was performed in a repeatable and precise manner.

• All samples were processed on the same day to avoid fluctuations in the performance of the laser system due to weather changes.

• The position of the sample in the z-direction was monitored and recorded before each sample was peened to ensure that the spot size was correct.

• The energy level was monitored and recorded before each sample was peened to ensure that it was not fluctuating while the LSP was being performed.

As part of the CSIR's health and safety protocols, it was important to wear laser protection goggles, respirator and hearing protection as the LSP process can be harmful to the eyes, ears, and lungs of an individual.

The peened samples are shown in Figure 34: AM samples after LSP. The laser power intensities are written on the masking tape with 0 being the as-built samples and power intensities going from 1.5 GW/cm² to 4.5 GW/cm².

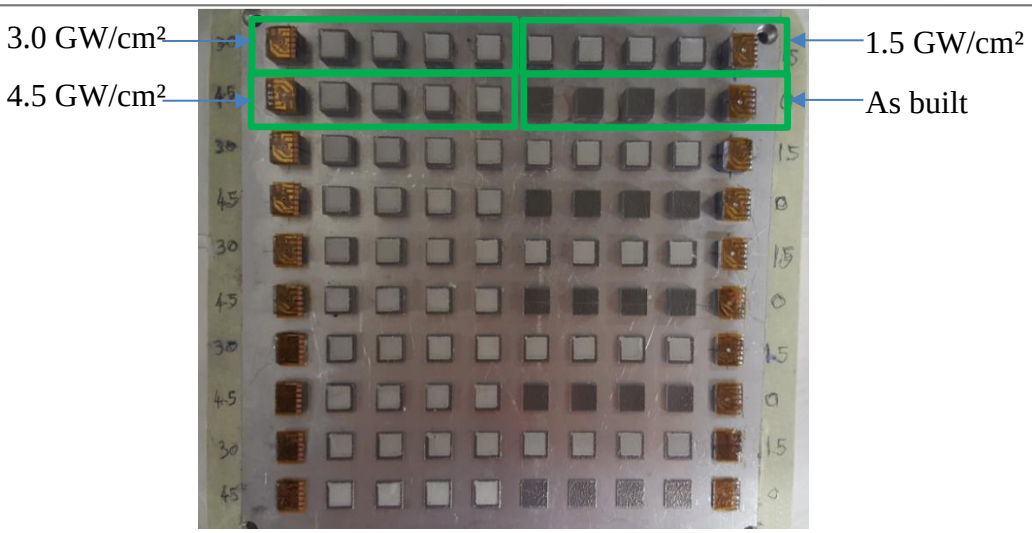

Figure 34: AM samples after LSP

The selection of these power intensities was to correspond with the previous work done in 2019 on AA7075 [48].

Chapter 3.4: Description Of The Surface Roughness Machine

Surface roughness measurements were performed to determine what kind of effect the LSP process had on the surface of the samples. The average roughness (Ra) value was measured in the x-direction on the 5 different thicknesses, the different power intensities and the as-built samples, for a total of 20 measurements.

Chapter 3.4.1: Apparatus

The measurements were performed using the Jenoptik Hommel Etamic T8000 machine, shown in Figure 35: Jenoptik Hommel Etamic T8000 surface roughness machine, which is based at the School of Mechanical Engineering at the University of Johannesburg, This device employs a stylus profilometer to measure the surface profile of a sample from which surface roughness parameters such as Ra can be calculated. The software provided by Hommel can output 3D surface images as well as 2D profiles The specifications of the Jenoptik Hommel Etamic T8000 can be found in Table 5: Surface roughness machine parameters.

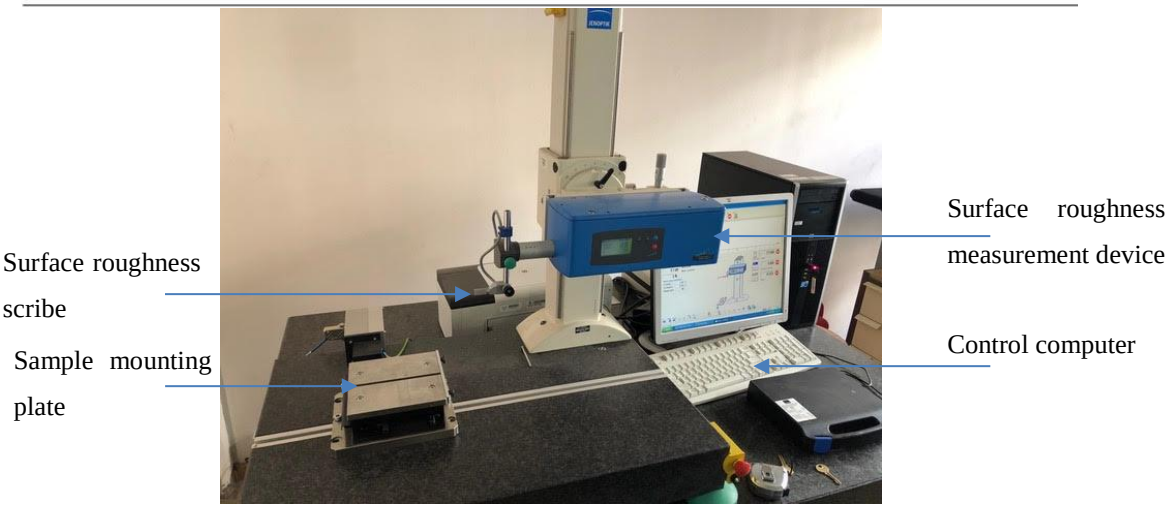

Figure 35: Jenoptik Hommel Etamic T8000 surface roughness machine

Table 5: Surface roughness machine parameters

Ra Measuring Range [µm]	-400 – 400
Resolution [µm]	0.01
Travel Length [mm]	6
Travel speed [mm/s]	0.15
Radius of Stylus Tip [µm]	5

For these experiments, the travel length was set to 6 mm and the travel speed was set to 0.15 mm/s. The surface roughness measurements were performed within the LSP region.

Chapter 3.4.2: Experimental Procedures

The following is the experimental procedure that was followed to perform the surface roughness measurements:

1. Place the sample on the mounting baseplate and ensure it is properly secured and aligned with the stylus pick-up.
2. Using the Hommel software lower the stylus towards the sample. Monitor the height of the probe on the screen and stop lowering when the probe reaches the zero point.
3. Hit “Measure” and allow the stylus to probe the surface.
4. Using the Hommel software, calibrate for the surface level.

5. Output the surface roughness report, the 2D and 3D profiles, using the Hommel software.
6. Convert the outputted surface roughness report to pdf via the pdf creator tool.

Chapter 3.5: Metallographic Sample Preparation

Some of the experiments listed in the sections below required the samples to be prepared in a specific manner. Some of the samples were sectioned, hot mounted and polished; these processes are described in this section.

Chapter 3.5.1: Sample Sectioning Apparatus

The samples were sectioned in half using a Struers Secotom-10, shown in Figure 36: Cutting apparatus, which is located at the School of Chemical and Metallurgical Engineering at the University of the Witwatersrand. A Struers Diamond Cut-off Wheel MOD13 for cutting materials with a hardness of less than HV 800 was used.

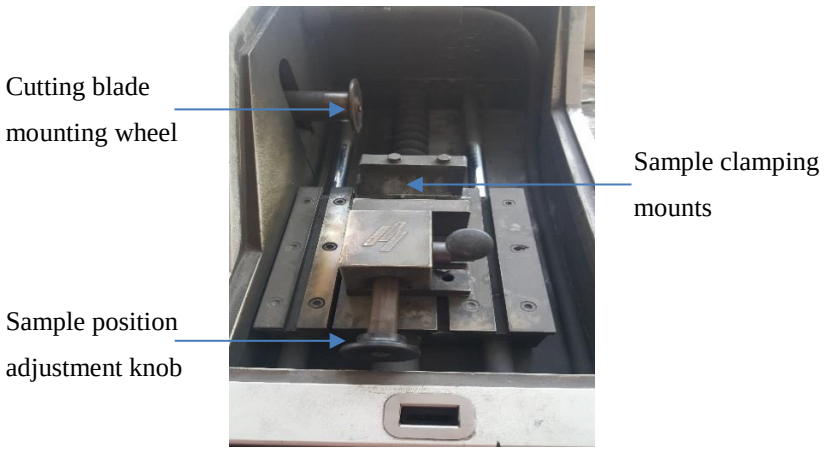

Figure 36: Cutting apparatus

The cutting specifications were as follows:

- Wheel Speed = 3500 RPM
- Feed Speed = 0.050 mm/s
- Cut Length = 50 mm

Chapter 3.5.1.1: Sample Sectioning Procedure

The experimental procedure used to section the samples was as follows:

1. First, mark the sample where the cut is to be made.
2. Place the sample in the mounting brackets of the cutting machine while lining up the marked sample so the blade is aligned
3. Close the clamp of the mounting bracket onto the sample and lock it in place with the clamp lock.
4. Turn the water on while ensuring that the water is flowing smoothly over the cutting disk.
5. Close the lid and start the cut.
6. When the cut is finished, remove and replace the sample, while repeating steps 1 through 5.

Chapter 3.5.2: Hot Mounting Apparatus

Samples were hot-mounted using the ATM OPAL 410 hot mounting machine shown in Figure 37: Hot mounting machine. Which is located at the hardness testing laboratory at the School of Chemical and Metallurgical Engineering at the University of the Witwatersrand

Figure 37: Hot mounting machine

The epoxy used for hot mounting was PolyFast Bakelite.

Chapter 3.5.2.1: Hot Mounting Procedure

The experimental procedure used to hot-mount the samples was as follows:

1. Place the sample onto the sample-holder with the face of interest down. Note that it is possible to mount multiple samples on a single mount as the mounting diameter is 2 cm
2. Lower the sample-holder into the machine.
3. Using a spoon, place enough PolyFast Bakelite powder around the sample so that it just covers the sample.
4. Close the machine and turn it on and wait for the specified curing time for the bakelite which is 5 minutes.
5. Remove the sample from the machine.
6. Etch the sample using sodium hydroxide (NaOH). The etching solution should be 10 millilitres of NaOH and 90 millilitres of distilled water. The etching time should be 30 seconds.

The finished hot mounted samples should appear similar to Figure 38: Hot mounted samples

Figure 38: Hot mounted samples

Chapter 3.5.3: Grinding And Polishing Of Sample

Samples were ground and polished at the material preparation laboratory of the School of Mechanical, Industrial and Aeronautical Engineering at the University of the Witwatersrand. The hand-polishing was performed using the Struers LaboPol-21 machine, shown in Figure 39: Grinding and polishing machine.

Figure 39: Grinding and polishing machine

Struers grinding and polishing disks were used. The lubricant used for grinding was water and for polishing, a diamond emulsion with the roughness corresponding to the polishing disk was used.

Chapter 3.5.3.1: Grinding And Polishing Experimental Procedures

The experimental procedure used to grind and polish the samples was as follows:

1. The order of the grinding and polishing is as follows:
    a. Grinding with 1000 µm
    b. Grinding with 500 µm
    c. Grinding with 100 µm
    d. Polishing with 9 µm
    e. Polishing with 3 µm
    f. Polishing with 1 µm
2. Place the desired grinding paper disk onto the grinding wheel and secure it down with the metal ring.
3. Turn the water on so that it runs smoothly over the disk.
4. Turn the machine on.
5. Carefully hold the sample onto the grinding disk, face down. Keep the sample in a fixed position and grind it until the only marks remaining on the sample face are those created in one direction by the grinding disk.
6. Once the sample is sufficiently ground at a particular level, remove it from the wheel, close the water tap and turn the machine off.

7. Replace the grinding paper with the next one and repeat steps 2 to 6 with each paper in the order stipulated in points 1a – 1c. Rotate sample 90˚ with each new grinding disk so that it will be visible when all the scratches in one direction from the previous step have been ground away and only marks in the new direction are visible.
8. Once all of the grinding steps have been concluded, move on to polishing.
9. Place the desired polishing disk onto the polishing wheel.
10. Place a small amount of the relevant emulsion on the polishing wheel.
11. Carefully hold the sample onto the polishing disk, face down. Rotate it 90◦ from the previous step and polish until the scratches from the previous step have been removed.
12. Once the sample is sufficiently polished at a particular level, remove it from the wheel and turn the machine off.
13. Replace the polishing disk with the next one and repeat steps (9) to (13) until all of the polishing steps have been completed, in the order stipulated in points 1d – 1f.

Chapter 3.6: Description Of The Optical Microscope

The School of Mechanical, Industrial and Aeronautical engineering at the University of the Witwatersrand owns an optical microscope, Nikon SMZ1500, figure 40, which makes use of a light source and lenses with high magnification power to magnify the microscopic features of the material and the damage that is partially induced on the surface of the sample due to machining.

Figure 40: Nikon SMZ1500 optical microscope

Chapter 3.7: Description Of The FESEM

A FESEM, which is based at the School of Chemical and Metallurgical Engineering at the University of the Witwatersrand, was used to obtain high magnification images of the cross-section of the samples. This was used to look for signs of un-melted material, porosity and changes in the microstructure.

Images were obtained for four samples which were the 2.6 mm thick samples with the different power intensities and the as-built sample.

Chapter 3.7.1: Apparatus

A Zeiss Sigma SEM, shown in Figure 41: Zeiss FESEM, was used for these experiments. It is located in the School of Chemical and Metallurgical Engineering at the University of the Witwatersrand. It is equipped with the following detectors:

- A Back-Scatter Detector (BSD) obtains images that show composition.
- An Oxford EDX Detector can be used for material characterisation.
- An in-lens detector which can be used for images of the material

Figure 41: Zeiss FESEM

Chapter 3.7.2: Experimental Set-up

For the cross-section, an in-lens image was each obtained at a magnification of 286X magnification on the surface of the LSP area.

Chapter 3.7.3: Experimental Procedures

The following was the experimental procedure used for obtaining the SEM images.

1. Place the samples on the sample holder and secure them using electrically conductive tape. Note which sample is in which position on the holder.
2. Place the samples onto the sample stage in the evacuation chamber.
3. Evacuate the chamber.
4. From the control panel, move the sample stage so that the sample of interest is in view.
5. Move the sample to the desired position on the sample.
6. At that location, save a BSD image at all of the desired magnifications.
7. Repeat steps (5) and (6) until each position on the sample has been imaged.
8. Perform steps (4) to (7) for each of the samples on the holder.

Chapter 3.8: Description Of The Hardness Testing Machine

The Vicker's microhardness of the samples was measured using a Future Tech microhardness FM 700 machine, shown in Figure 42: Vicker's microhardness machine

which is based in the School of Chemical and Metallurgical Engineering at the University of the Witwatersrand.

Chapter 3.8.1: Apparatus

The Future Tech microhardness testing machine was used to perform the microhardness tests for this project with the assistance of a trained technician.

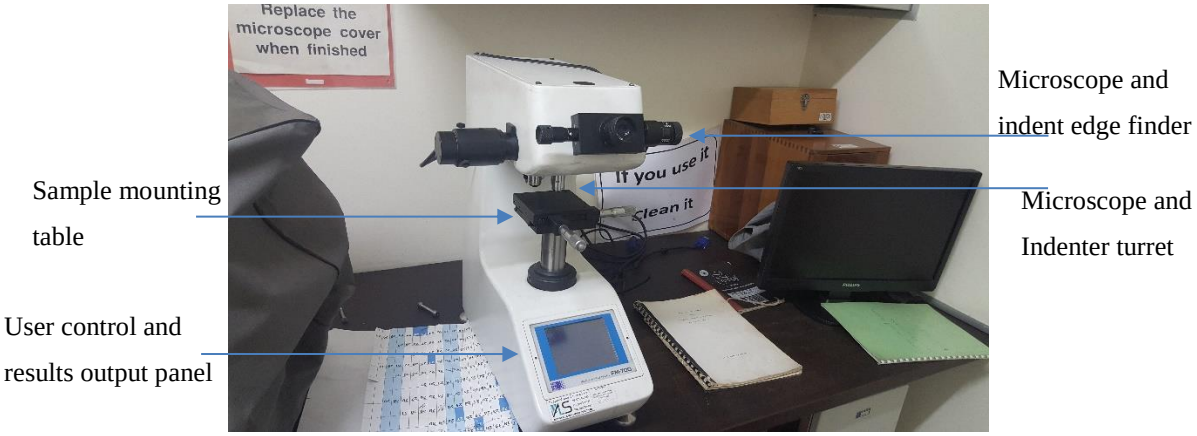

Figure 42: Vicker's microhardness machine

The machine is equipped with a Vicker's Hardness Indentor as well as two optical microscope objective lenses (magnification of 10× and 50×). The objective lenses are used for sample positioning and viewing the indent so that its size can be determined. The sample position can be controlled with a resolution of 0.01 mm using the two-micrometre screw-gauges. The testing parameters microhardness was determined from the depth of LSP previously mentioned in section 1.8. Since it was found from the literature that the depth of the LSP was approximately 1300 µm, it was decided to use a range of 1400 µm to make sure to account for all of the LSP effects. This depth was then divided into 10 indent spacings which corresponded to an indent spacing of 140 µm. As the material is a printed material it was decided to use a slightly higher force of 500 gf. The testing procedure was in line with the ASTM standard E384: Knoop and Vickers microhardness testing.

Chapter 3.8.2: Experimental Set-up

The following was the experimental set-up for these experiments:

- The indent force was 500 gf.
- The dwell time was 10 seconds.
- Measurements were performed at depth steps of 0.14 mm

The distance between measurements of 0.14 mm was greater than 2.5× the indent diameter (which was around 0.03 mm) so the measurements are within the best-practice recommendations.

Chapter 3.8.3: Experimental Procedures

The following is the experimental Procedure for performing micro-hardness tests:

1. Place the sample onto the levelling block and then place it onto the sample stage
2. Set the objective lens to 50× magnification. Move the sample using the micrometre screw gauge so that the left edge is on the centre of the cross-hairs of the microscope lens.
3. Move the sample so that the top-left corner is at the centre of the cross-hairs. Note the values on the micrometres.
4. Calculate the micrometre values for the measurement positions based on the relative location from the top-left corner of the sample.
5. Move the sample to the desired position.
6. Adjust the focus of the sample so that the surface is in focus.
7. Using the control panel of the machine, rotate the revolving turret such that the indenter is over the sample and will then perform an indent with the force and dwell time specified.
8. After performing the indent, rotate the revolving turret via the control panel, so that the objective lens is back over the sample. Position the cross hairs of the microscope over the middle of the sample and then using the knobs position the measurement lines over the edges of the indent in both the height and breadth directions. Then take the measurement
9. The control panel will show the microhardness value. Record this value.
10. Repeat steps (7) to (9) for every measurement position on the sample.
11. Repeat every step for each sample.

Chapter 3.9: Description Of The IHD Machine And The Procedure

IHD was performed using the SINT Technology Restan MTS-3000 Automatic Hole Drilling Machine which is based in the laboratory of the School of Mechanical, Industrial and Aeronautical Engineering at the University of the Witwatersrand.

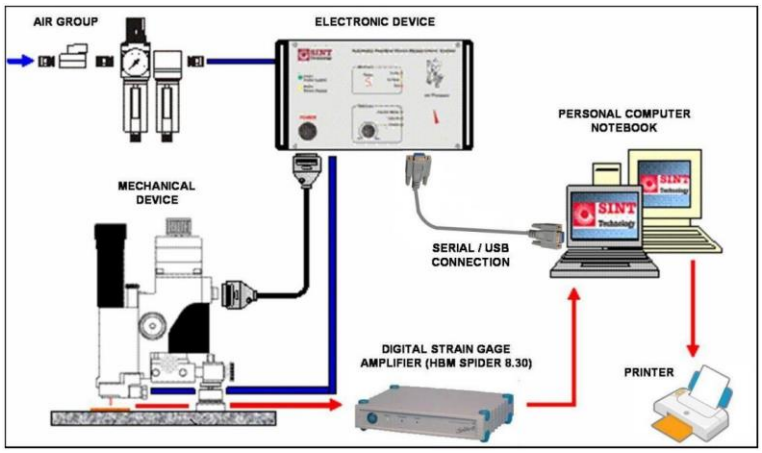

Figure 43: Schematic of the IHD machine

The IHD machine is comprised of a pneumatic drill, optical microscope for hole positioning on the sample, a z - stage motor control, adjustable levelling feet and dial gauges for measuring the hole diameter. The IHD machine is supplied with air from the electronic device and the incremental Z-stage motor control is also supplied from the electronic device. The laptop is used to set the parameters for the IHD and to also collect the data from the data acquisition system (DAQ), which was a Quantum X.

Figure 44: IHD machine setup

The apparatus used to install a strain gauge rosette on a sample are pictured in Figure 45: Equipment for strain gauge application

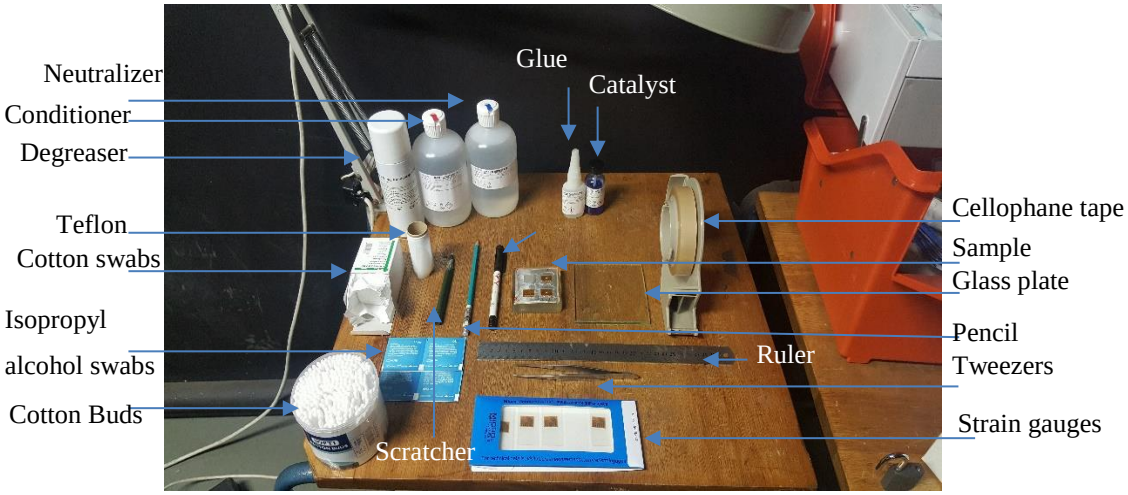

Figure 45: Equipment for strain gauge application

The strain gauge used for this project was manufactured by Vishay Precision Group and purchased from Elexsys. The rosette is shown in Figure 46: Strain gauge rosette and the specifications are listed in Table 6: Strain gauge rosette specifications

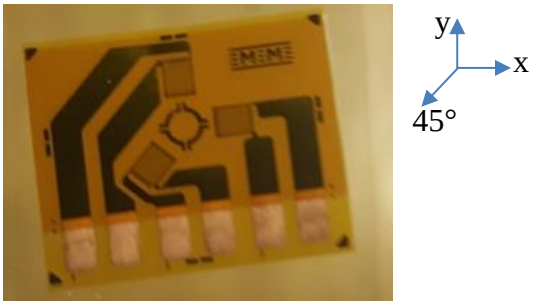

Figure 46: Strain gauge rosette CEA-13-062UL-120

Table 6: Strain gauge rosette specifications

Name	CEA-13-062UL-120
ASTM E837 Type	A
Rosette Diameter [mm]	5.13
Nominal Hole Diameter [mm]	2
Minimum Thickness [mm]	5.13
Minimum Depth Step [mm]	0.02

Drilling Depth [mm]	1.2
Stress Calculation Depth [mm]	1

The hole diameter was controlled by using a drill bit with the appropriate end-mill diameter. The drill bit used was SS White Carbide Burs FG-38 supplied by Millners Dental Suppliers.

The samples were clamped to the laboratory working surface by clamping the ends of the baseplate to the surface during the experiment. This was to prevent the sample from moving during the test.

Chapter 3.9.1: Experimental Procedures

The following is the procedure followed to perform each IHD test:

1. Install the strain gauge rosette on the sample.
   a. Before commencing work, ensure hands and equipment have been thoroughly cleaned.
   b. Decide how the strain gauge rosette will be aligned with the sample. Use a pencil to lightly mark a cross centre on this location.
   c. Use tweezers to carefully lay the rosette onto the glass plate and lay a length of cellophane tape over it.
   d. Clean the sample first with isopropyl alcohol swabs. Then use the three separate cleaning chemicals, in the following order: a de-greaser, a conditioner to slightly etch the surface and a neutraliser to neutralise the conditioner. Apply the chemical to the cleaning swab and wipe the area to be cleaned. Every wipe should be in the same direction to prevent dirt from returning to the clean area. Be extremely careful not to touch anything that has been cleaned to prevent contaminating the sample.
   e. Lift the cellophane tape and the attached rosette from the glass plate and move it over to the sample. Lower the rosette onto the sample in the correct location. Using the marked centre lines as a guide

f. Lift the tape again to reveal the bottom of the rosette and apply a thin layer of catalyst to it. Wait one minute, while gently apply pressure to the strain gauge using the palm of your hand.
g. Place a single drop of the glue onto the sample and carefully lower the rosette back onto the sample and glue and apply a large pressure using the palm of your hand and hold it for three minutes.
h. Remove the tape, secure the sample to the table under the IHD machine and solder the wires from the DAQ to the solder pads on the rosette.

2. Align the drill bit with the rosette.
   a. Level the IHD machine with the sample with the use of the bubble-level.
   b. Align the drill bit with the strain gauge rosette. Using the microscope on the IHD machine, align the cross-hairs of the microscope with the strain gauge rosette. Then turn the drill on and carefully lower it until it just touches the surface of the rosette which is when metallic burs begin to appear on the rosette surface. Use the microscope to check the drill bit is drilling in the correct location and make adjustments as necessary. Then repeat the process until the bit is drilling at the centre of the strain gauge rosette.
   c. Connect the surface detection trigger wires to the IHD machine and the sample and run the command that places the end-mill on the surface.
3. Set up the software to run the test. The following details should be checked:
   a. The drill depth steps and total depth should be those stipulated in Table 6: Strain gauge rosette specifications.
   b. The strain readings should be set to zero.
   c. The “drill delay” and “acquisition delay” (both explained in point 5 below) should be set to 5 s and 15 s, respectively.
   d. Ensure that the software is set to save the raw data to a new file.
4. Perform the test.
5. Each hole is automatically drilled according to the following procedure:
   a. The drill begins spinning.
   b. The drill is advanced one drill step length into the sample.
   c. At the target depth, the drill continues to spin for a stipulated time period, known as the “drill delay”.

d. The drill stops spinning for a stipulated time period, known as the "acquisition delay", which is waited for before a strain reading is taken.
e. Steps (a) to (d) are repeated until the total hole depth is reached.

6. Process the data using the Eval Sint 7.16 software specifying the ASTM 13 a, extend, non-uniform stress gradient calculation method with the Tickonov correction factor applied

Chapter 4: Results

This section has four major parts, the observations of the as-built AM samples and the observations of the LSP samples peened at the different power intensities of 1.5, 3.0 and 4.5 GW/cm^2. It must be noted that this section provides the observation of the results and a detailed discussion of the results is done in chapter 5.

Chapter 4.1: Observations Of As-Built Samples

This section provided the different observations of the as-built sample for the different experiments conducted on the samples.

Chapter 4.1.1: Surface Roughness Analysis Of As-Built AM Sample

The surface roughness report from the Hommel machine provided insightful information for each sample, an extract from one of the reports is provided below showing the surface roughness parameters, a typical 2D profile and the 3D profile.

The table in Figure 47 is an extract from the Hommel report for the as-built 1.2mm thick sample showing the different surface roughness parameters. The Ra value is the one under investigation.

Extracted profile

ISO 4287		
Amplitude parameters - Rougl		
Rp	3.23	µm
Rv	3.29	µm
Rz	6.52	µm
Rc	4.07	µm
Rt	10.9	µm
Ra	1.66	µm
Rq	1.99	µm
Rsk	-0.00559	
Rku	2.35	

Figure 47: Surface roughness parameters

Figure 48 is a 2D profile of the as-built 1.2mm thick sample. The highest peak was at 40µm and the lowest peak was at -38µm.

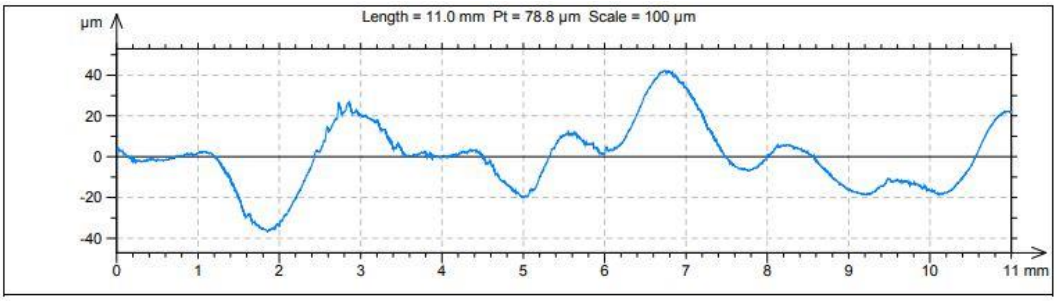

Figure 48: Surface roughness 2D profile

Figure 49 is a 3D profile extracted from the Hommel report for the as-built 1.2mm thick samples.

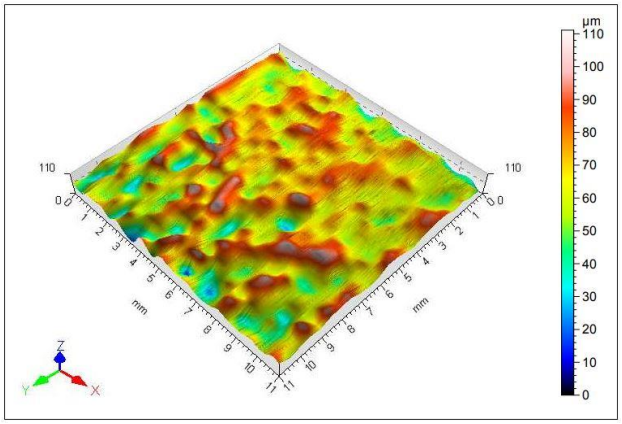

Figure 49: Surface roughness 3D profile

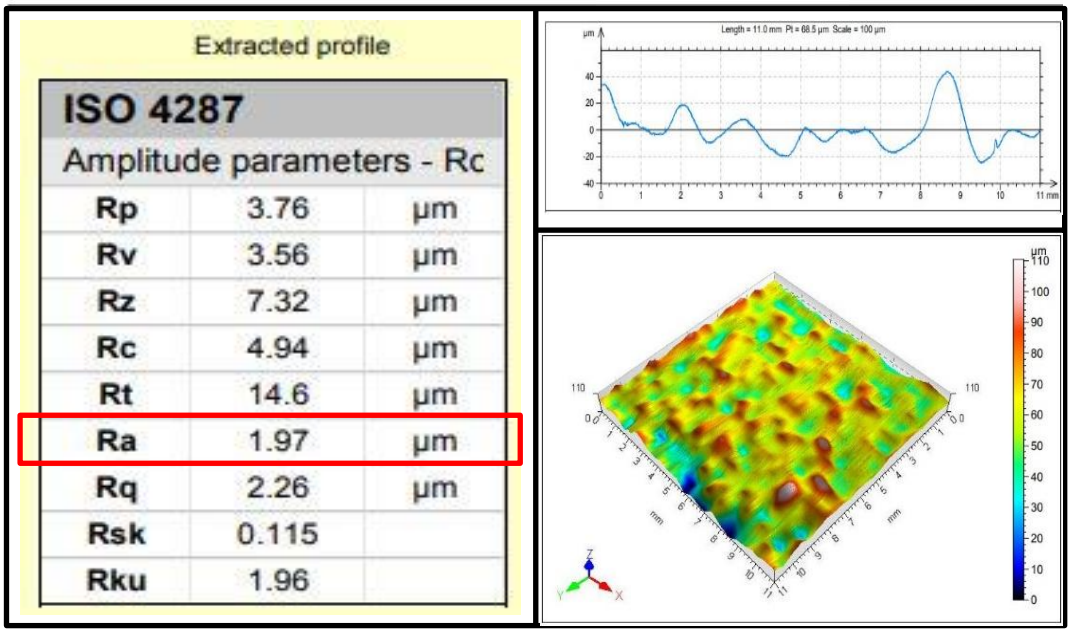

Figure 50: Surface roughness parameters, 2-D and 3-D profiles of 2.6 mm as-built sample

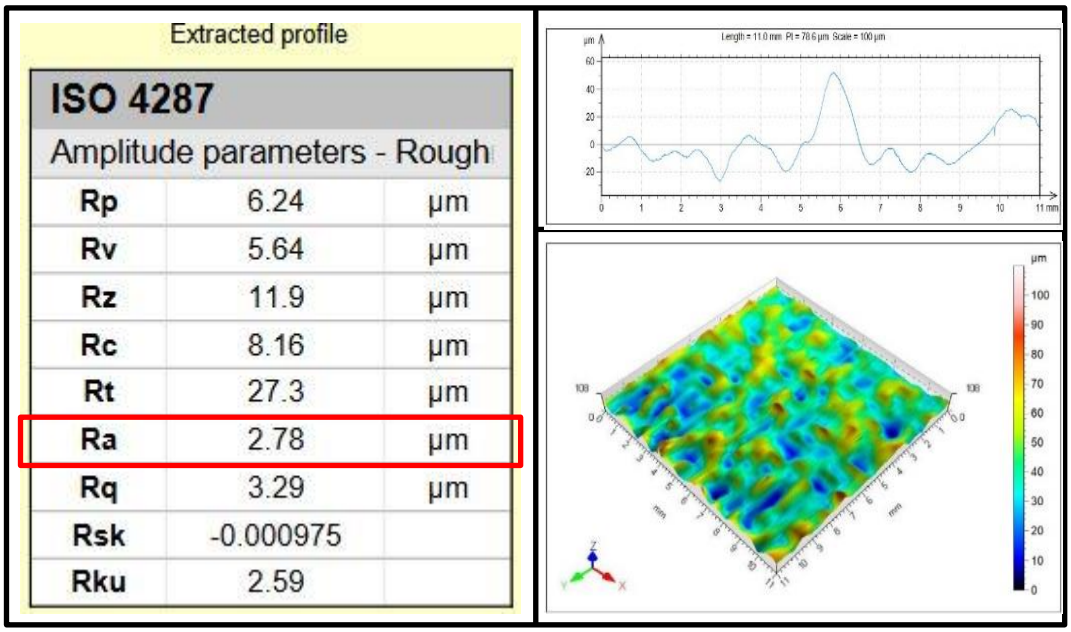

Figure 51: Surface roughness parameters, 2-D and 3-D profiles of 5.6 mm as-built sample

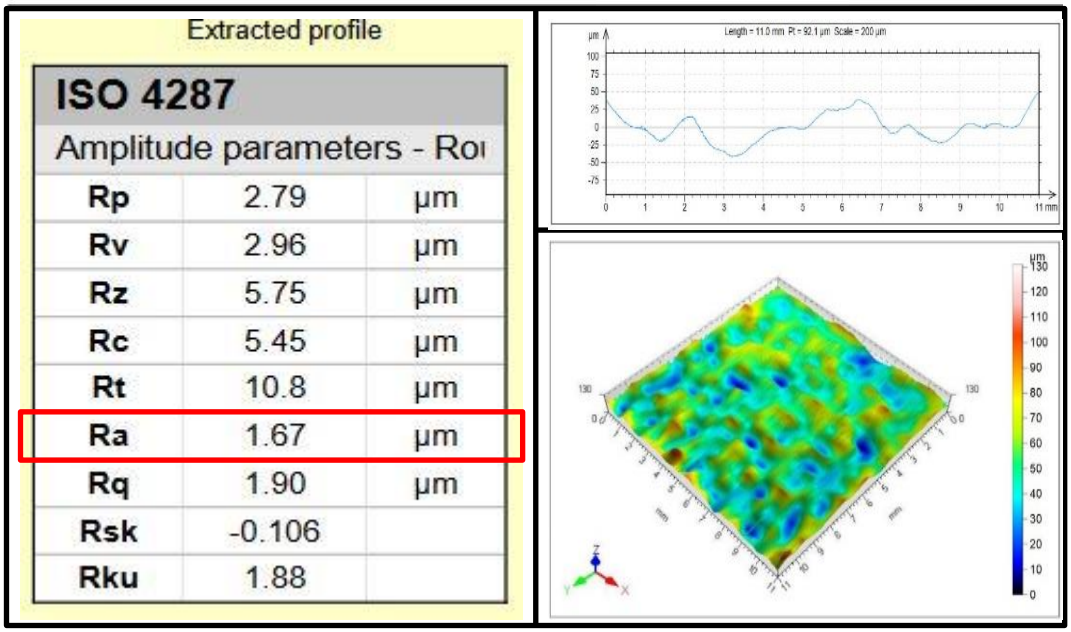

Extracted profile

ISO 4287		
Amplitude parameters - Roı		
Rp	2.79	µm
Rv	2.96	µm
Rz	5.75	µm
Rc	5.45	µm
Rt	10.8	µm
Ra	1.67	µm
Rq	1.90	µm
Rsk	-0.106	
Rku	1.88	

Figure 52: Surface roughness parameter, 2-D and 3-D profiles of 9.6 mm as-built sample

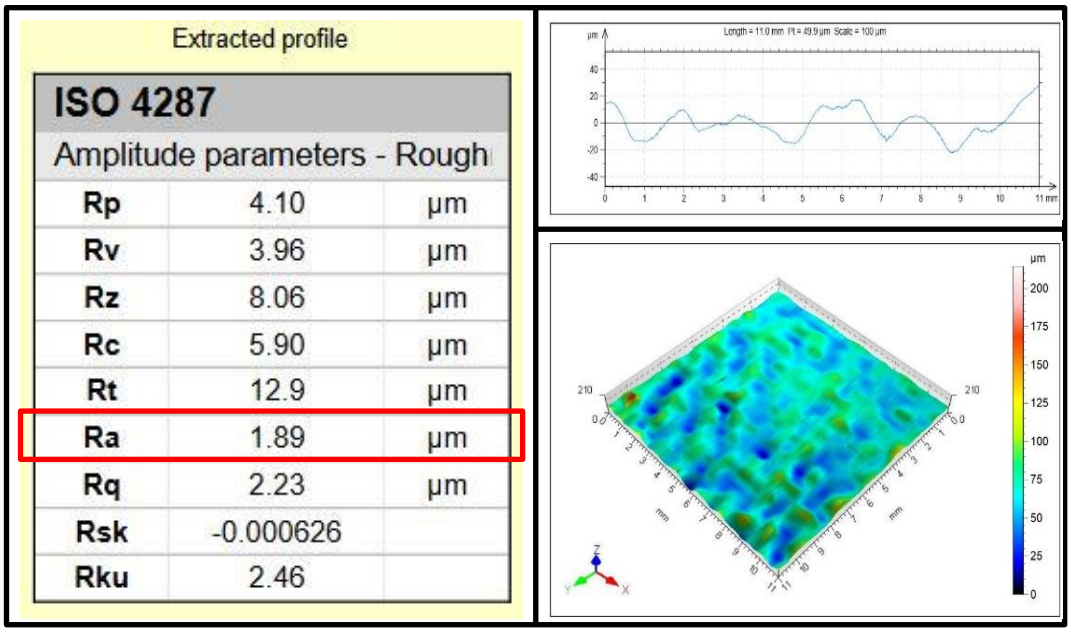

Extracted profile

ISO 4287		
Amplitude parameters - Rough		
Rp	4.10	µm
Rv	3.96	µm
Rz	8.06	µm
Rc	5.90	µm
Rt	12.9	µm
Ra	1.89	µm
Rq	2.23	µm
Rsk	-0.000626	
Rku	2.46	

Figure 53: Surface parameters, 2-D and 3-D profiles of 13.6 mm as-built sample

Chapter 4.1.2: Optical Microscopy Analysis Of As-Built Samples

The optical microscopy of the surface of the as-built samples is shown in Fig. 54, using the Nikon metallographic camera with a magnification of 1x.

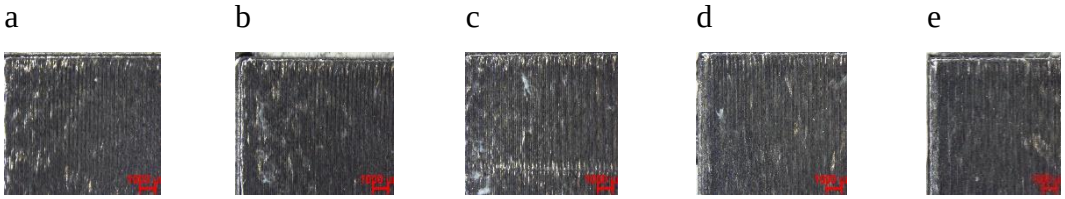

Figure 54: Optical microscopy of surface of as built samples (a) 1.2 mm, (b) 2.6 mm, (c) 5.6 mm, (d) 9.6 mm and (e) 13.6 mm

The optical microscopy of the cross-section near the surface of the as-built samples is shown below, using the Nikon metallographic camera with a magnification of 1x.

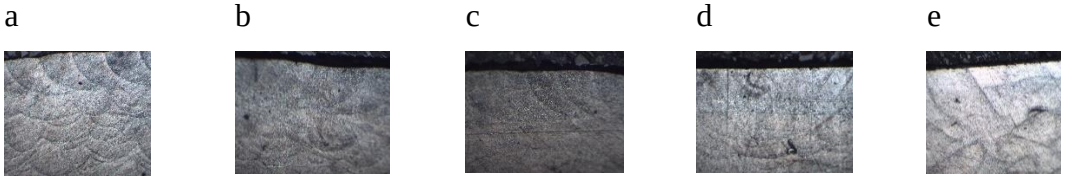

Figure 55: Optical microscopy of cross section of as built samples near the surface (a) 1.2 mm, (b) 2.6 mm, (c) 5.6 mm, (d) 9.6 mm and (e) 13.6 mm

The optical microscopy of the cross-section near the middle of the as-built samples is shown below, using the Nikon metallographic camera with a magnification of 1x.

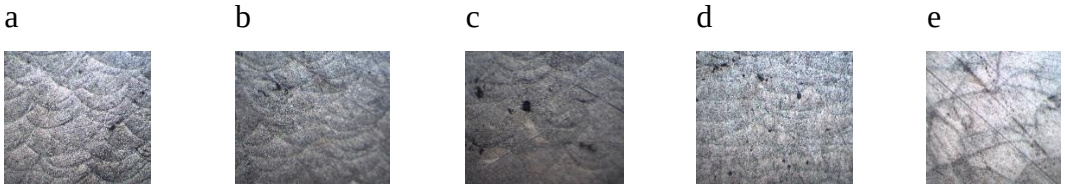

Figure 56: Optical microscopy of cross section of as built samples near the middle (a) 1.2 mm, (b) 2.6 mm, (c) 5.6 mm, (d) 9.6 mm and (e) 13.6 mm

The optical microscopy of the cross-section at the interface between the as-built sample and the baseplate is shown below, using the Nikon metallographic camera with a magnification of 1x.

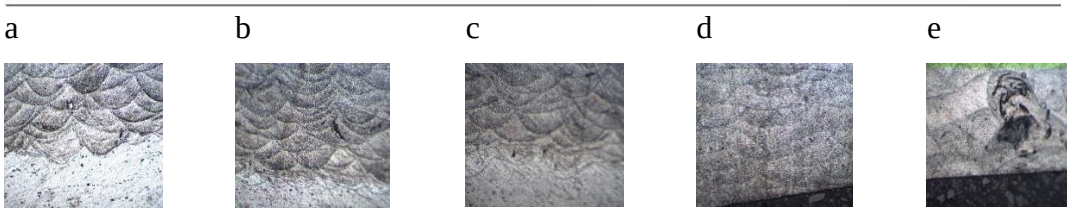

Figure 57: Optical microscopy of cross section of as built samples at the interface (a) 1.2 mm, (b) 2.6 mm, (c) 5.6 mm, (d) 9.6 mm and (e) 13.6 mm

Chapter 4.1.3: Scanning Electron Microscopy Of As-Built Sample

Unfortunately, it was not possible to obtain images of the surface of the samples under the SEM due to glue on the surface from residual stress measurements still being on the samples after ultrasonic cleaning. It was possible to take images of the cross-section of the samples, shown below in Fig. 66.

An image of the cross-section of the surface of the as-built 2.6 mm thick sample is shown. It is interesting to note the pores of the material are only beginning to appear after approximately 100µm from the surface of the sample. Du Plessis et al. [76], noted that with an increase in LSP power intensity there was a closing of the pores which improves fatigue life. The additional images of the samples with 2.6 mm thickness are presented in Appendix E.

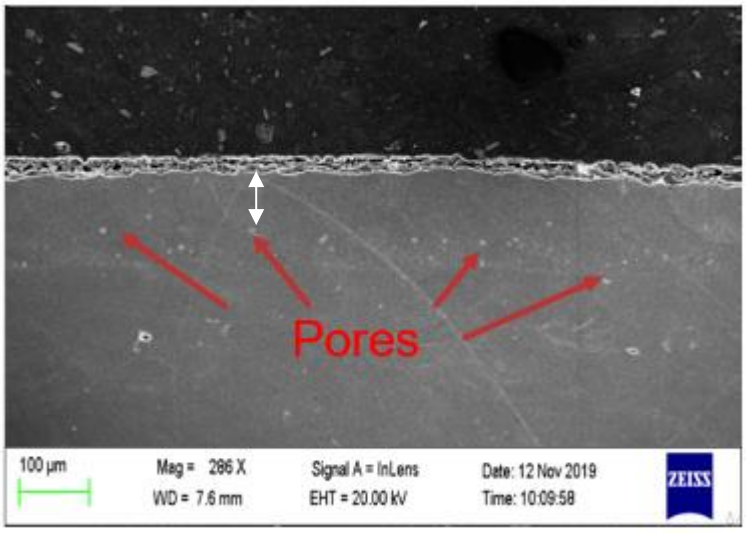

Figure 58: SEM image of sample as built 2.6mm

Chapter 4.1.4: Microhardness Test Analysis Of As-Built Samples

The microhardness of the material was measured for each thickness with an average indent spacing of 140 µm with a 500 gf load applied for 10 seconds. The first indent of the samples corresponded to the surface of the material and the last indent corresponded to the side closest to the interface of the AM material and the base plate. The Vickers microhardness values for the first 10 indents of the as-built samples are shown in Table 7. The total length of the sample is approximately 1.4 mm.

Table 7: Microhardness values of as-built samples.

As-built samples					
Indent	1,2 mm	2,6 mm	5,6 mm	9,6 mm	13,6 mm
1	102,1	111,5	121,8	115,2	126,3
2	111,1	124,4	119,6	115,2	131,9
3	109,4	128,6	132,7	120,3	95,5
4	139,4	126,9	122,4	123,3	126,8
5	139,7	134,7	126,2	104,1	104,9
6	139,8	126,8	121,8	120,5	125,4
7	139,3	126,7	121,3	120,6	125
8	133,3	127	120,8	129,4	120,5
9	133,3	138,8	120,9	129,5	123,8
10	122,4	136,6	122,5	138,6	117,3

Figure 59 shows the microhardness values plotted against the number of indents.

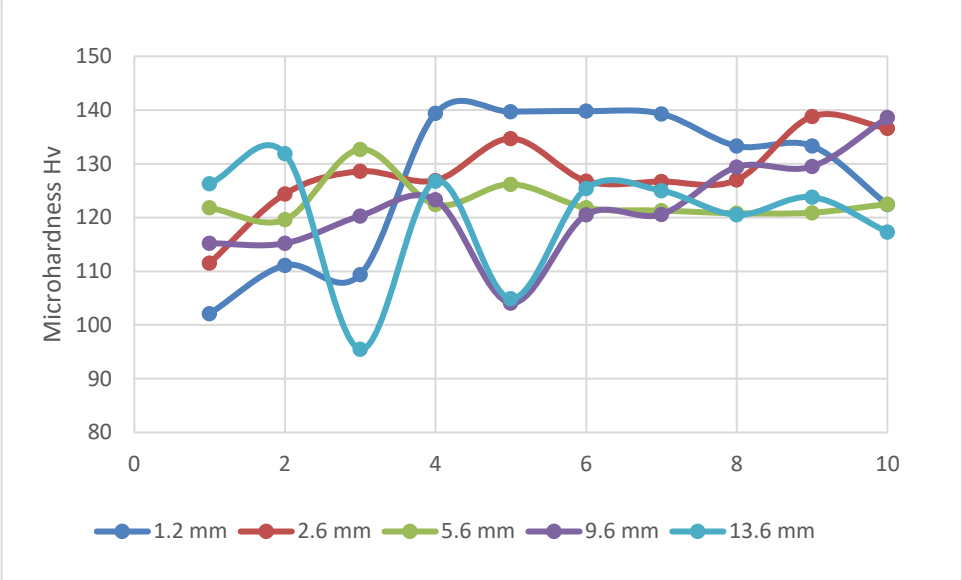

Figure 59: Microhardness values of as-built samples.

The exact values of microhardness and the indent distance is presented in Appendix D.

Chapter 4.1.5: IHD Results Of As-Built Samples

This section provides details of the IHD results that were obtained for the as-built samples. The results are presented with measurements of a hole depth of increment 0.025 mm up until a hole depth of 0.8 mm. The values and corresponding hole depth for all the samples are presented in Appendix E. The five different thicknesses are illustrated.

Table 8: Principal stress values Smax of as-built samples

As-built samples					
Depth [mm]	1,2 mm	2,6 mm	5,6 mm	9,6 mm	13,6 mm
0,025	357,266	175,535	35,08	49,372	140,418
0,075	280,124	215,154	204,068	151,969	149,895
0,125	276,125	251,626	294,998	181,395	163,532
0,175	280,015	271,379	301,177	204,891	179,637
0,225	309,01	266,294	298,977	223,253	193,978
0,275	314,455	248,522	297,5	236,045	205,07
0,325	255,062	233,471	290,946	234,15	209,216

0,375	202,233	222,159	279,407	234,514	205,795
0,425	228,577	213,272	264,086	237,775	200,92
0,475	281,143	208,396	254,782	229,161	200,024
0,525	251,432	207,65	254,454	219,351	205,011
0,575	202,151	209,339	250,62	220,747	219,132
0,625	204,553	210,173	238,603	214,09	240,716
0,675	216,904	207,683	229,783	185,152	255,499
0,725	201,403	204,833	228,672	163,859	257,133
0,775	182,908	204,592	226,443	171,243	272,046

Figure 60 shows the maximum principal stress values plotted against the incremental hole depth.

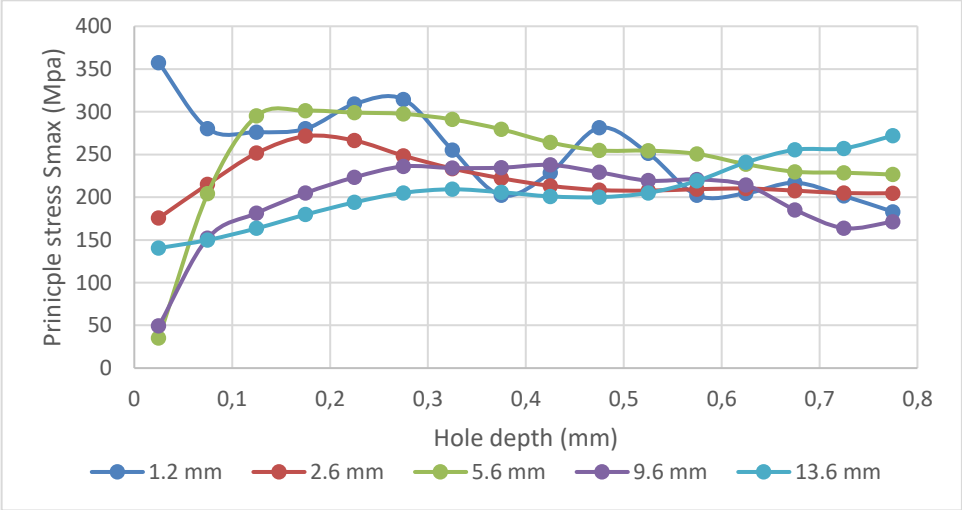

Figure 60: Principal stress Smax of as-built samples

Chapter 4.2: Observations Of 1.5 GW/cm^2 LSP'ed Samples

This section provides the different observations of the 1.5 GW/cm^2 sample for the different experiments conducted on the samples.

Chapter 4.2.1: Surface Roughness Analysis Of The 1.5 GW/cm^2 LSP'ed Sample

The surface roughness report from the Hommel machine provided insightful information for each sample, an extract from one of the reports is provided below showing the surface roughness parameters, a typical 2D profile and the 3D profile.

Figure 61 is an extract from the Hommel report for the 1.5 GW/cm^2 LSP'ed 1.2mm thick sample showing the different surface roughness parameters. The Ra value is the one under investigation.

Extracted profile

ISO 4287		
Amplitude parameters - Rc		
Rp	7.93	µm
Rv	7.14	µm
Rz	15.1	µm
Rc	7.56	µm
Rt	23.4	µm
Ra	2.77	µm
Rq	3.41	µm
Rsk	0.121	
Rku	2.82	

Figure 61: Surface roughness parameters

Figure 62 is a 2D profile of the 1.5 GW/cm^2 LSP'ed, 1.2mm thick sample. The highest peak was at 52 µm and the lowest peak was at -22 µm.

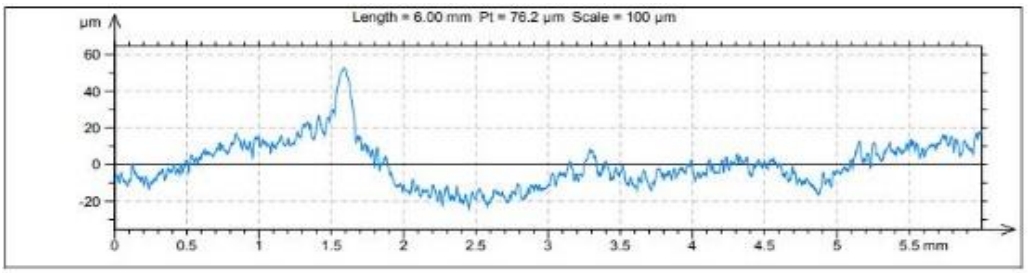

Figure 62: Surface roughness 2D profile

Figure 63 below is a 3D profile extracted from the Hommel report for the as-built 1.2mm thick samples.

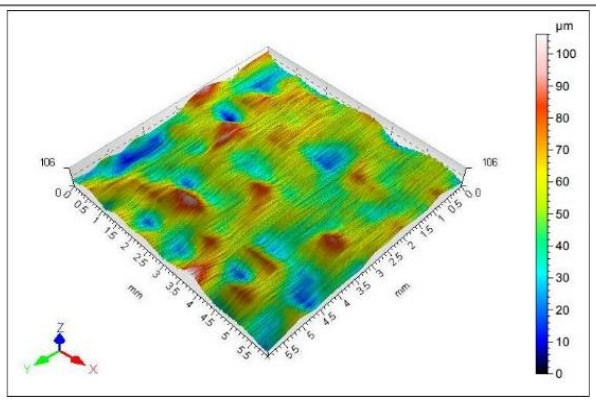

Figure 63: Surface roughness 3D profile

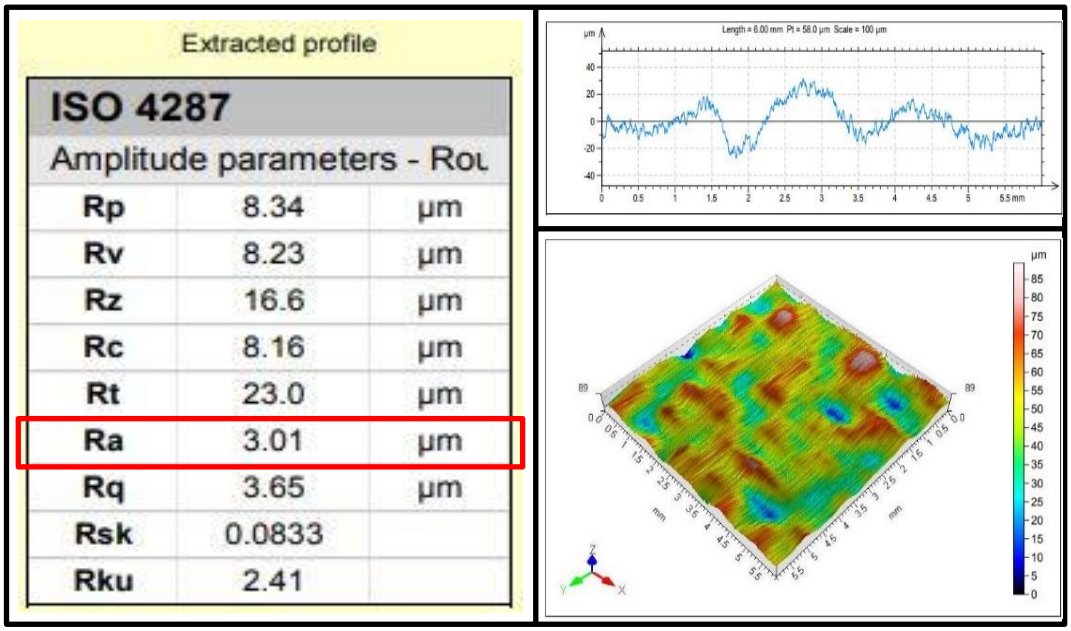

Figure 64: Surface roughness parameters, 2-D and 3-D profiles of 2.6 mm 1.5 GW/cm^2 sample

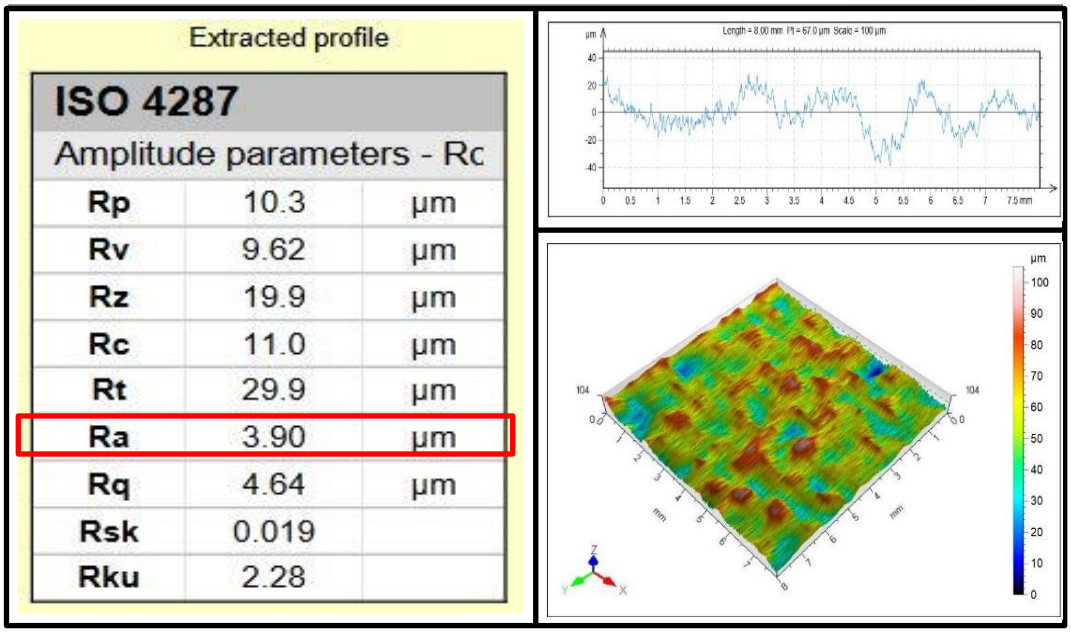

Figure 65: Surface roughness parameters, 2-D and 3-D profiles of 5.6 mm 1.5 GW/cm^2 sample

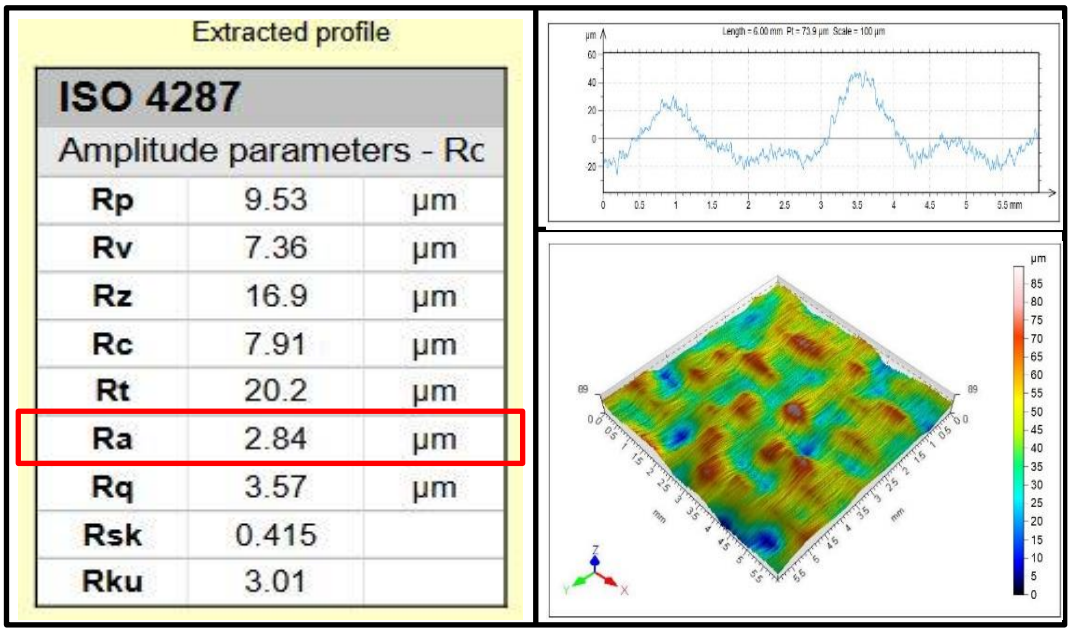

Figure 66: Surface roughness parameters, 2-D and 3-D profiles of 9.6 mm 1.5 GW/cm^2 sample

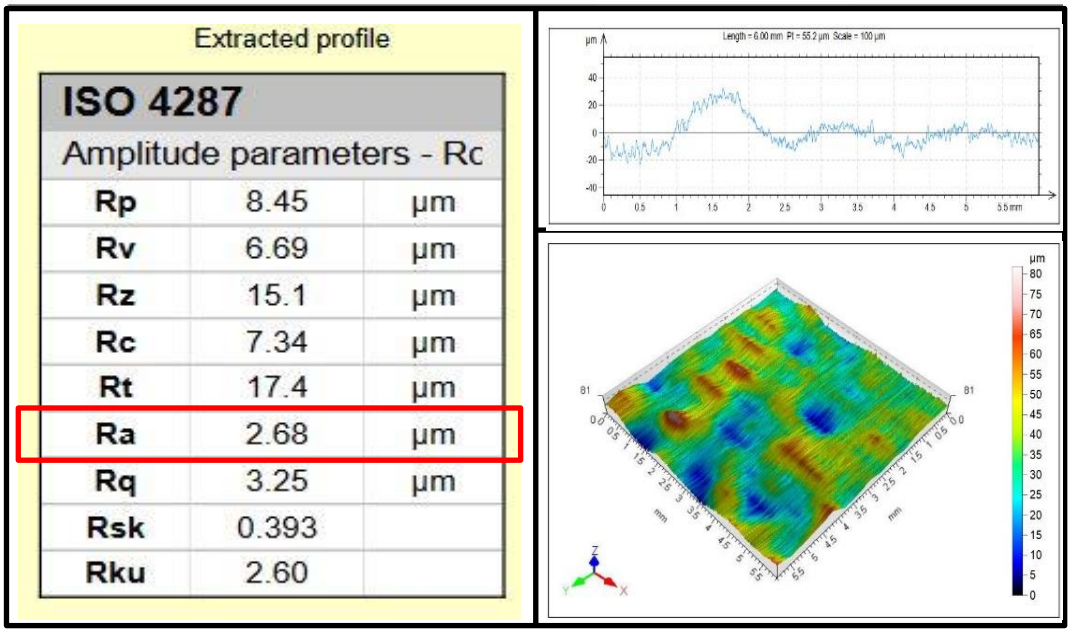

Figure 67: Surface roughness parameters, 2-D and 3-D profiles of 13.6 mm 1.5 GW/cm^2 sample

Chapter 4.2.2: Optical Microscopy Analysis Of 1.5 GW/cm^2 LSP'ed Samples

The optical microscopy of the surface of the as-built samples is shown below, using the Nikon metallographic camera with a magnification of 1x.

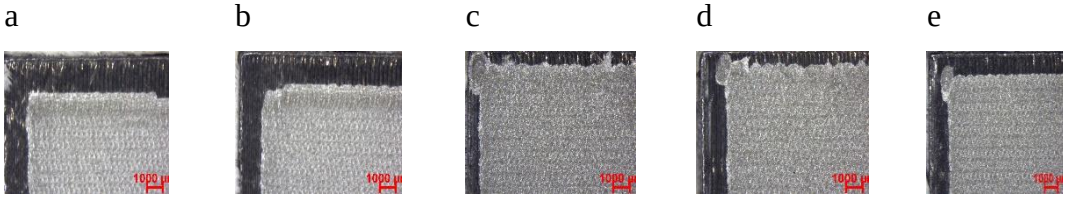

Figure 68: Optical microscopy of surface of 1.5 GW/cm^2 LSP'ed samples (a) 1.2 mm, (b) 2.6 mm, (c) 5.6 mm, (d) 9.6 mm and (e) 13.6 mm

The optical microscopy of the cross-section near the surface of the 1.5 GW/cm^2 LSP'ed samples is shown below, using the Nikon metallographic camera with a magnification of 1x.

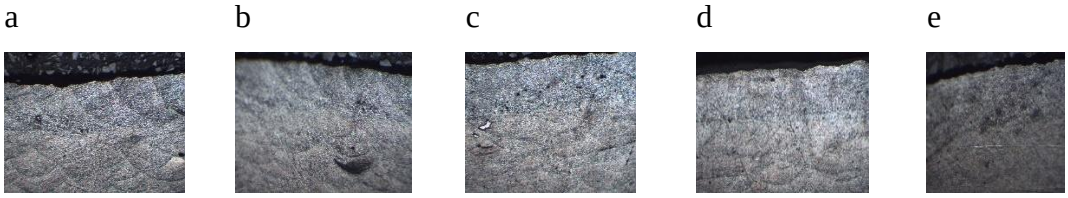

Figure 69: Optical microscopy of cross section of 1.5 GW/cm^2 LSP'ed samples near the surface (a) 1.2 mm, (b) 2.6 mm, (c) 5.6 mm, (d) 9.6 mm and (e) 13.6 mm

The optical microscopy of the cross-section near the middle of the 1.5 GW/cm^2 LSP'ed samples is shown below, using the Nikon metallographic camera with a magnification of 1x.

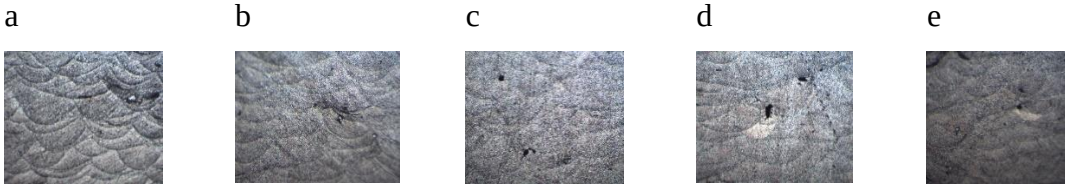

Figure 70: Optical microscopy of cross section of 1.5 GW/cm^2 LSP'ed samples near the middle (a) 1.2 mm, (b) 2.6 mm, (c) 5.6 mm, (d) 9.6 mm and (e) 13.6 mm

The optical microscopy of the cross-section at the interface between the 1.5 GW/cm^2 LSP'ed sample and the baseplate is shown below, using the Nikon metallographic camera with a magnification of 1x.

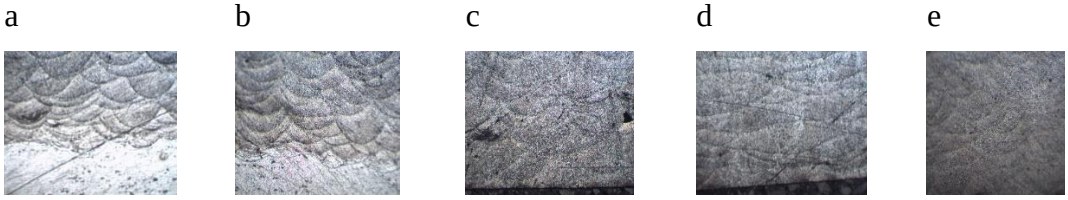

Figure 71: Optical microscopy of cross section of 1.5 GW/cm^2 LSP'ed samples at the interface (a) 1.2 mm, (b) 2.6 mm, (c) 5.6 mm, (d) 9.6 mm and (e) 13.6 mm

Chapter 4.2.3: Scanning Electron Microscopy Of 1.5 GW/cm^2 LSP'ed Sample

Unfortunately, it was not possible to obtain images of the surface of the samples under the SEM due to glue on the surface from residual stress measurements still being on the samples after ultrasonic cleaning. It was also not possible to take

images of the cross-section of the samples, due to the global pandemic of the coronavirus.

Chapter 4.2.4: Microhardness Test Analysis of 1.5 GW/cm^2 LSP'ed Samples

The microhardness of the material was measured for each thickness with an average indent spacing of 140µm. The first indent of the samples corresponded to the surface of the material and the last indent corresponded to the side closest to the interface of the AM material and the base plate. The Vickers hardness values for the first 10 indents of the as-built samples are shown in the table below. The total length of the sample is approximately 1.4 mm. It is unfortunate that during the cutting of the samples to fit as many as possible on an SEM sample block, the 5.6 mm and 9.6 mm were cut short, hence it was not possible to go to the end of the number of indents.

Table 9: Microhardness values of 1.5 GW/cm^2 samples.

1.5 GW/cm^2					
Indent	1,2 mm	2,6 mm	5,6 mm	9,6 mm	13,6 mm
1	107	144,7	123,8	122,5	121,5
2	165,3	136,1	107,2	123,7	129,1
3	152	131,3	128,5	128,6	131
4	152,1	121,4	133,5	125,7	128,6
5	141,3	120,6	131,6	139,8	122,8
6	139,3	120,2	138,3	144,2	122,6
7	129,7	119,5	146		121,3
8	145,3	119,3	145,4		120,3
9	113,3	115,3			120,3
10	111,1	111,5			125,9

Figure 72 shows the microhardness values plotted against the number of indents.

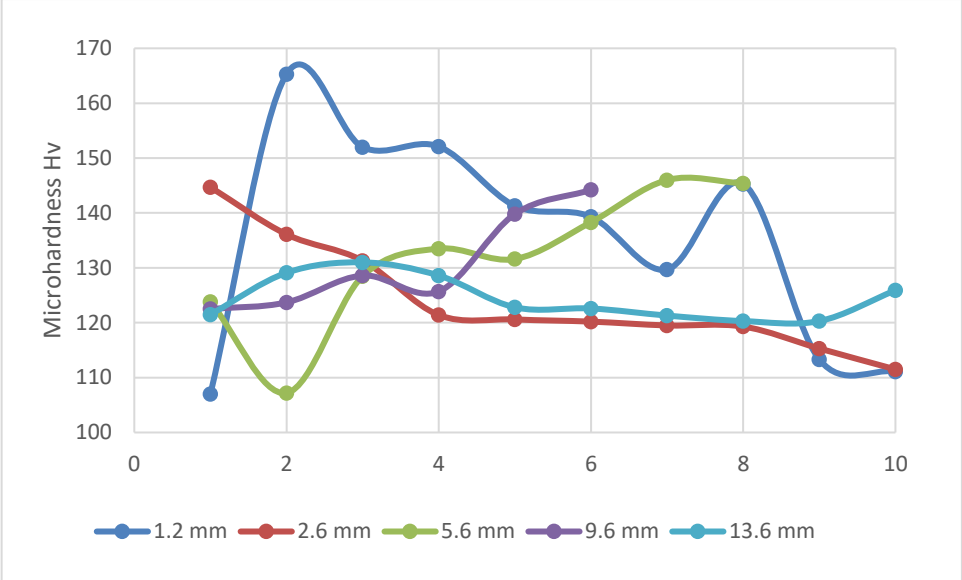

Figure 72: Microhardness values of 1.5 GW/cm^2 LSPeened samples.

The exact values of microhardness and the indent distance is presented in Appendix D.

Chapter 4.2.5: IHD Results Of 1.5 GW/cm^2 LSPeened Samples

This section provides details of the IHD results that were obtained for the as-built samples. The results are presented with measurements of a hole depth of increment 0.025 mm up until a hole depth of 0.8 mm. The values and corresponding hole depth for all the samples are presented in appendix E. The five different thicknesses are shown in table 10 below.

Table 10: Principal stress values Smax of 1.5 GW/cm^2 LSP'ed samples

1.5 GW/cm^2 samples					
Depth [mm]	1,2 mm	2,6 mm	5,6 mm	9,6 mm	13,6 mm
0,025	71,17	-40,972	8,654	-101,358	19,735
0,075	6,676	-65,696	-37,348	-68,692	14,039
0,125	-47,003	-78,931	-79,833	-46,332	4,871
0,175	-82,896	-76,844	-94,729	-35,803	-17,041
0,225	-91,154	-59,763	-86,461	-29,956	-55,515
0,275	-86,797	-47,07	-73,379	-19,184	-91,64
0,325	-77,019	-42,969	-65,318	-2,767	-110,228

0,375	-65,308	-38,727	-62,296	-14,638	-112,55
0,425	-55,95	-31,626	-60,508	-32,753	-106,075
0,475	-43,646	-22,994	-55,46	-34,829	-98,064
0,525	-22,75	-11,226	-44,824	-26,243	-91,455
0,575	3,732	5,83	-25,179	-18,919	-84,741
0,625	25,468	25,685	6,44	-10,275	-74,141
0,675	37,782	41,505	41,192	0,139	-56,532
0,725	45,346	46,238	63,753	16,311	-33,716
0,775	53,738	38,512	67,581	40,608	-10,957

Figure 73 shows the maximum principal stress values plotted against the incremental hole depth.

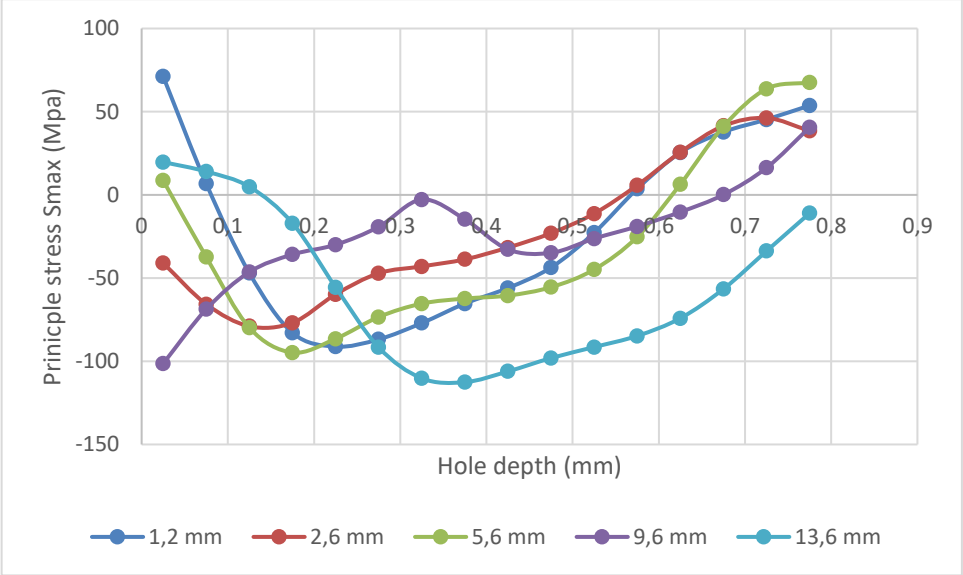

Figure 73: Principal stress Smax of 1.5 GW/cm^2 LSP'ed samples

Chapter 4.3: Observations Of 3.0 GW/cm^2 LSP'ed Samples

This section provided the different observations of the 3.0 GW/cm^2 sample for the different experiments conducted on the samples.

Chapter 4.3.1: Surface Roughness Analysis Of The 3.0 GW/cm^2 LSP'ed Sample

The surface roughness report from the Hommel machine provided insightful information for each sample, an extract from one of the reports is provided below showing the surface roughness parameters, a typical 2D profile and the 3D profile, these surface roughness parameters and profiles are supplied in Appendix D for all the samples.

The table reported in Figure 74 is an extract from the Hommel report for the 3.0 GW/cm^2 LSP'ed 1.2 mm thick sample showing the different surface roughness parameters. The Ra value is the one under investigation.

Extracted profile

ISO 4287		
Amplitude parameters - Rou		
Rp	11.3	µm
Rv	11.6	µm
Rz	22.9	µm
Rc	12.2	µm
Rt	31.2	µm
Ra	4.13	µm
Rq	5.11	µm
Rsk	0.0116	
Rku	2.78	

Figure 74: Surface roughness parameters

Figure 75 is a 2D profile of the 3.0 GW/cm^2 LSP'ed, 1.2mm thick sample. The highest peak was at 52 µm and the lowest peak was at -22 µm.

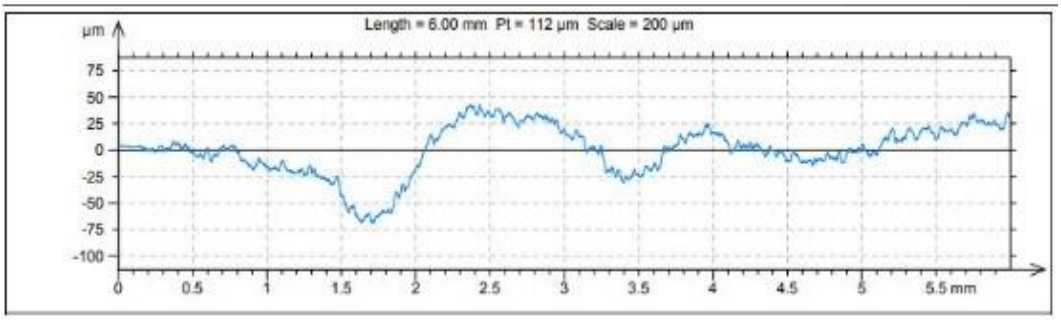

Figure 75: Surface roughness 2D profile

Figure 76 is a 3D profile extracted from the Hommel report for the 3.0 GW/cm^2 LSP'ed 1.2mm thick samples.

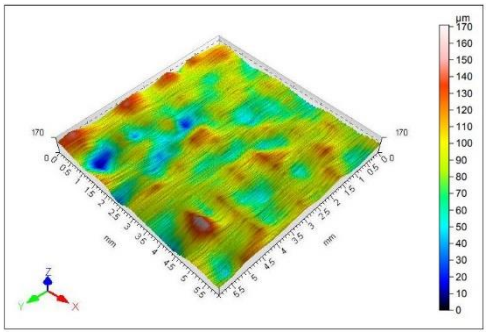

Figure 76: Surface roughness 3D profile

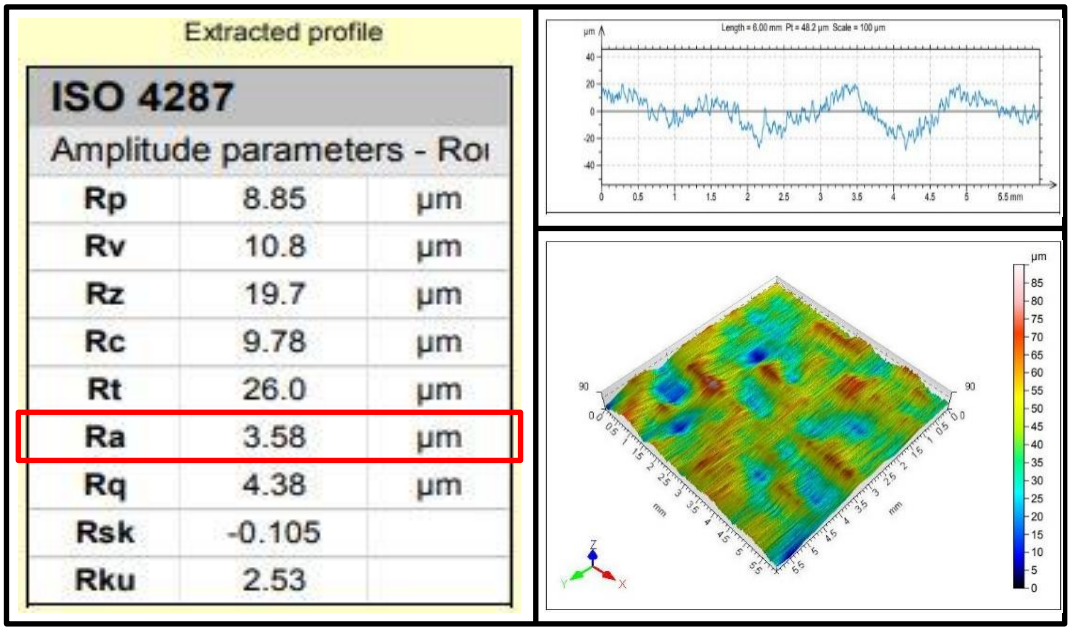

Extracted profile

ISO 4287		
Amplitude parameters - Roı		
Rp	8.85	µm
Rv	10.8	µm
Rz	19.7	µm
Rc	9.78	µm
Rt	26.0	µm
Ra	3.58	µm
Rq	4.38	µm
Rsk	-0.105	
Rku	2.53	

Figure 77: Surface roughness parameters, 2-D and 3-D profiles of 2.6 mm 3.0 GW/cm^2 sample

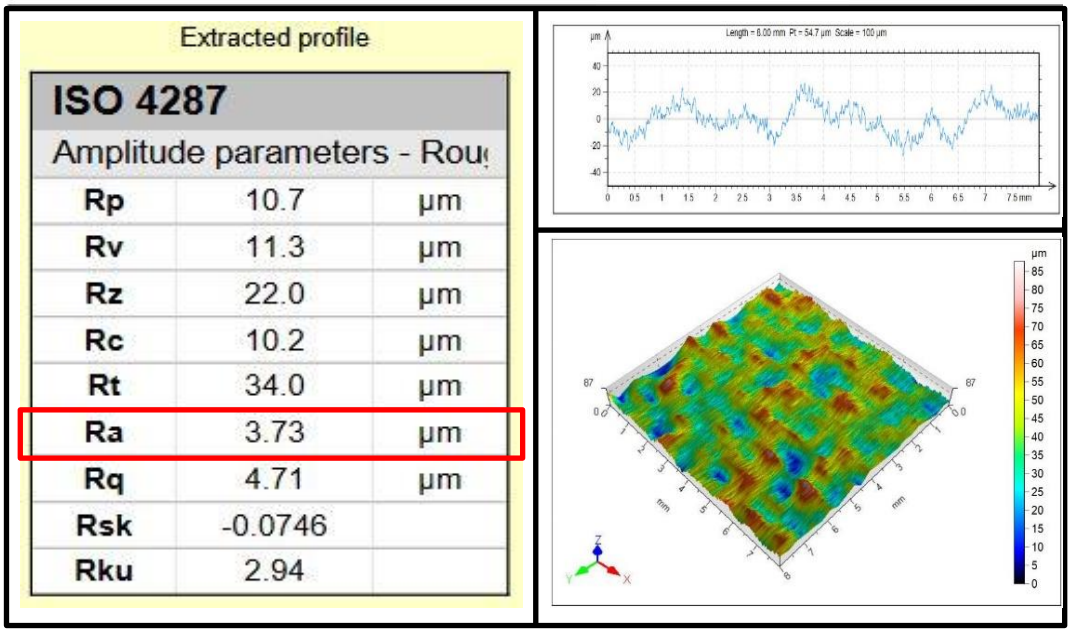

Extracted profile

ISO 4287		
Amplitude parameters - Rou		
Rp	10.7	µm
Rv	11.3	µm
Rz	22.0	µm
Rc	10.2	µm
Rt	34.0	µm
Ra	3.73	µm
Rq	4.71	µm
Rsk	-0.0746	
Rku	2.94	

Figure 78: Surface roughness parameters, 2-D and 3-D profiles of 5.6 mm 3.0 GW/cm^2 sample

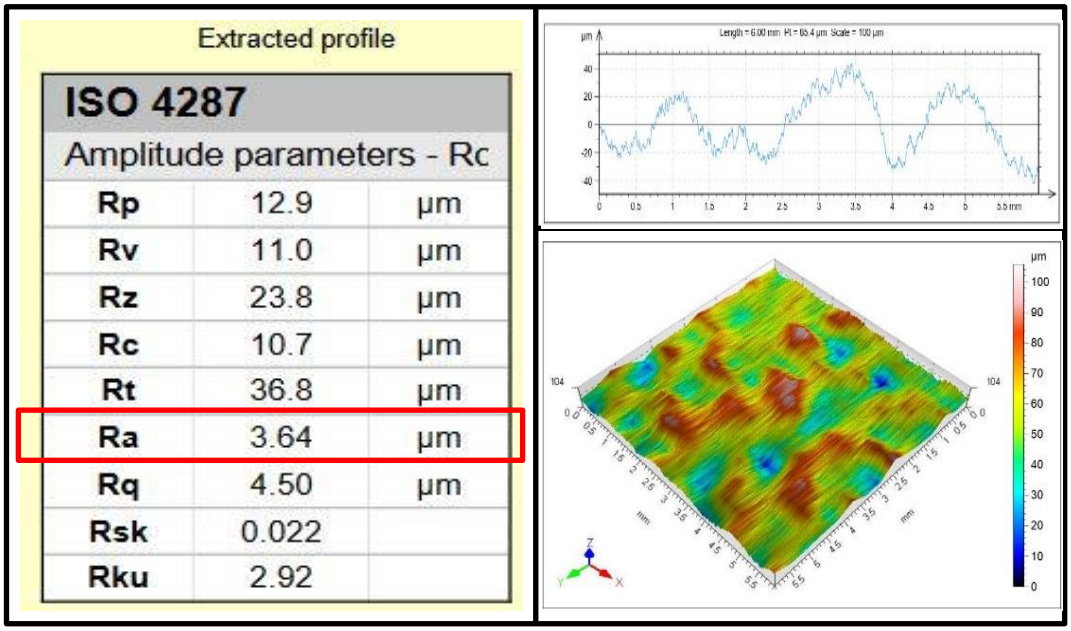

Extracted profile

ISO 4287		
Amplitude parameters - Rc		
Rp	12.9	µm
Rv	11.0	µm
Rz	23.8	µm
Rc	10.7	µm
Rt	36.8	µm
Ra	3.64	µm
Rq	4.50	µm
Rsk	0.022	
Rku	2.92	

Figure 79: Surface roughness parameters, 2-D and 3-D profiles of 9.6 mm 3.0 GW/cm^2 sample

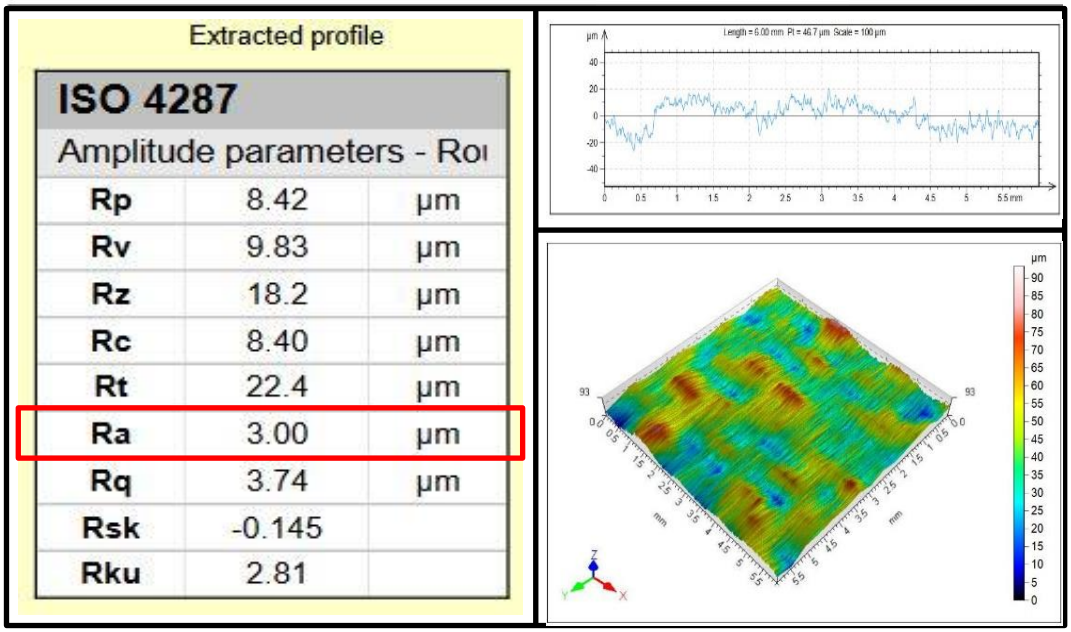

Figure 80: Surface roughness parameters, 2-D and 3-D profiles of 13.6 mm 3.0 GW/cm^2 sample

Chapter 4.3.2: Optical Microscopy Analysis of 3.0 GW/cm^2 LSP'ed Samples

The optical microscopy of the surface of the 3.0 GW/cm^2 LSP'ed samples is shown below, using the Nikon metallographic camera with a magnification of 1x.

a b c d e

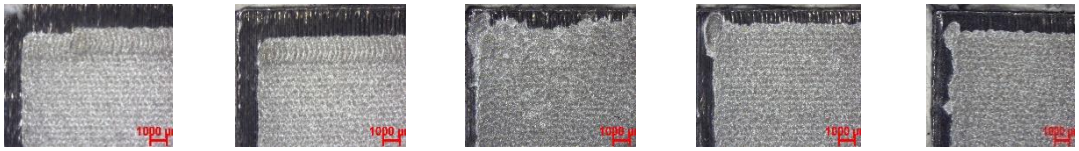

Figure 81: Optical microscopy of surface of 3.0 GW/cm^2 LSP'ed samples (a) 1.2 mm, (b) 2.6 mm, (c) 5.6 mm, (d) 9.6 mm and (e) 13.6 mm

The optical microscopy of the cross-section near the surface of the 3.0 GW/cm^2 LSP'ed samples is shown below, using the Nikon metallographic camera with a magnification of 1x.

a b c d e

Figure 82: Optical microscopy of cross section of 3.0 GW/cm^2 LSP'ed samples near the surface (a) 1.2 mm, (b) 2.6 mm, (c) 5.6 mm, (d) 9.6 mm and (e) 13.6 mm

The optical microscopy of the cross-section near the middle of the 3.0 GW/cm^2 LSP'ed samples is shown below, using the Nikon metallographic camera with a magnification of 1x. The optical microscopy for the 1.2 mm was not available at this time.

a b c d e

Figure 83: Optical microscopy of cross section of 3.0 GW/cm^2 LSP'ed samples near the middle (a) 1.2 mm, (b) 2.6 mm, (c) 5.6 mm, (d) 9.6 mm and (e) 13.6 mm

The optical microscopy of the cross-section at the interface between the 3.0 GW/cm^2 LSP'ed sample and the baseplate is shown below, using the Nikon metallographic camera with a magnification of 1x.

a b c d e

Figure 84: Optical microscopy of cross section of 3.0 GW/cm^2 LSP'ed samples at the interface (a) 1.2 mm, (b) 2.6 mm, (c) 5.6 mm, (d) 9.6 mm and (e) 13.6 mm

Chapter 4.3.3: Scanning Electron Microscopy of 3.0 GW/cm^2 LSP'ed Sample

Unfortunately, it was not possible to obtain images of the surface of the samples under the SEM due to glue on the surface from residual stress measurements still being on the samples after ultrasonic cleaning. It was also not possible to take

images of the cross-section of the samples, due to the global pandemic of the coronavirus.

Chapter 4.3.4: Microhardness Test Analysis of 3.0 GW/cm^2 LSP'ed Samples

The microhardness of the material was measured for each thickness with an average indent spacing of 140µm. The first indent of the samples corresponded to the surface of the material and the last indent corresponded to the side closest to the interface of the AM material and the base plate. The Vickers hardness values for the first 10 indents of the 3.0 GW/cm^2 LSP'ed samples are shown in Table 11. The total length of the sample is approximately 1.4 mm. It is unfortunate that during the cutting of the samples to fit as many as possible on an SEM sample block, the 1.2 mm was cut short, hence it was not possible to go to the end of the number of indents.

Table 11: Microhardness values of 3.0 GW/cm^2 LSP'ed samples.

3,0 GW/cm^2					
Indent	1,2 mm	2,6 mm	5,6 mm	9,6 mm	13,6 mm
1	99,3	103,7	83	94,5	156,9
2	119	102	127,1	108,8	165,1
3	135,1	106,4	131,7	114,1	159
4	129,6	117,5	132,5	112,6	158,3
5	122	115,8	134,3	116,7	143,4
6	126	118,8	126,6	109,2	145,2
7	122,2	123,7	149,4	111	143,7
8	122,6	123,9	137,2	108,4	143,9
9	119	126,5	141,2	110,3	148,5
10		122,6	133,6	110	144,1

Figure 85 shows the microhardness values plotted against the number of indents.

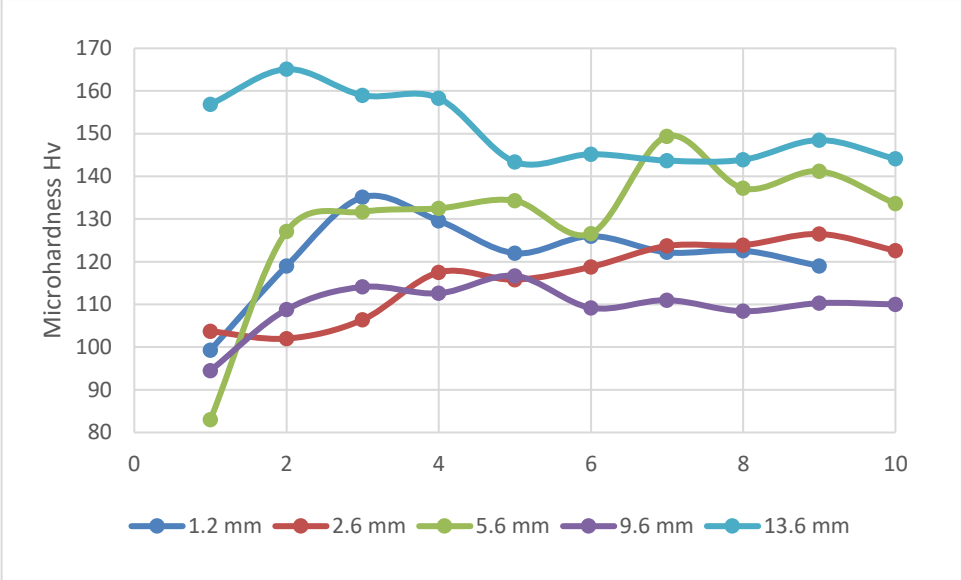

Figure 85: Microhardness values of 3.0 GW/cm^2 LSP'ed samples.

The exact values of microhardness and the indent distance is presented in Appendix D.

Chapter 4.3.5: IHD Results Of 3.0 GW/cm^2 LSP'ed Samples

This section provides details of the IHD results that were obtained for the 3.0 GW/cm^2 samples. The results are presented with measurements of a hole depth of increment 0.025 mm up until a hole depth of 0.8 mm. The values and corresponding hole depth for all the samples are presented in Appendix E. The five different thicknesses are shown in Table 12.

Table 12: Principal stress values Smax of 3.0 GW/cm^2 LSP'ed samples

3.0 GW/cm^2 samples					
Depth [mm]	1,2 mm	2,6 mm	5,6 mm	9,6 mm	13,6 mm
0,025	-113,377	11,261	21,838	17,648	-13,155
0,075	-139,23	-45,481	-45,339	-44,431	-102,074
0,125	-140,723	-98,172	-89,266	-100,008	-153,453
0,175	-114,642	-133,816	-120,741	-138,67	-151,351
0,225	-84,684	-147,535	-139,934	-155,314	-135,892
0,275	-70,238	-146,855	-146,136	-153,74	-128,967
0,325	-63,031	-141,313	-144,313	-140,244	-120,601
0,375	-47,471	-137,556	-141,022	-122,753	-105,116

0,425	-30,931	-134,798	-137,465	-108,262	-88,053
0,475	-29,47	-129,077	-131,455	-98,955	-72,828
0,525	-37,525	-120,062	-120,421	-92,441	-58,461
0,575	-35,225	-108,421	-104,633	-85,607	-45,705
0,625	-22,531	-93,608	-88,461	-76,805	-38,875
0,675	-11,884	-78,14	-75,821	-65,471	-32,173
0,725	-7,52	-65,555	-65,851	-52,111	-22,937
0,775	-5,014	-55,448	-56,594	-38,855	-13,765

Figure 86 shows the maximum principal stress values plotted against the incremental hole depth.

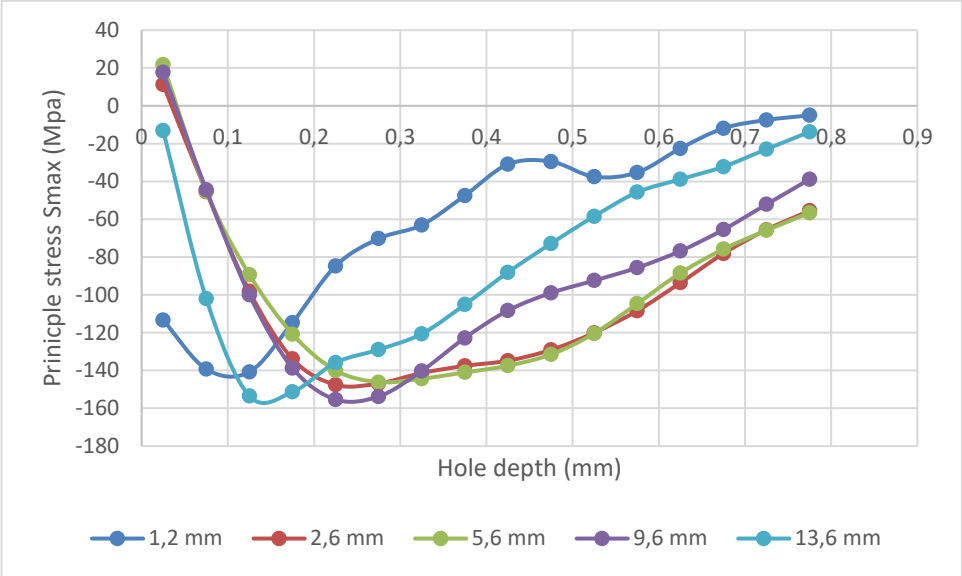

Figure 86: Principal stress Smax of 3.0 GW/cm^2 LSP'ed samples

Chapter 4.4: Observations Of 4.5 GW/cm^2 LSP'ed Samples

This section provided the different observations of the 4.5 GW/cm^2 LSP'ed sample for the different experiments conducted on the samples.

Chapter 4.4.1: Surface Roughness Analysis Of The 4.5 GW/cm^2 LSP'ed Sample

The surface roughness report from the Hommel machine provided insightful information for each sample, an extract from one of the reports is provided below

showing the surface roughness parameters, a typical 2D profile and the 3D profile, these surface roughness parameters and profiles are supplied in Appendix D for all the samples.

Figure 87 shows an extract from the Hommel report for the 4.5 GW/cm^2 LSP'ed 1.2 mm thick sample showing the different surface roughness parameters. The Ra value is the one under investigation.

Extracted profile

ISO 4287		
Amplitude parameters - Rc		
Rp	13.0	µm
Rv	10.6	µm
Rz	23.7	µm
Rc	12.5	µm
Rt	30.5	µm
Ra	4.63	µm
Rq	5.66	µm
Rsk	0.185	
Rku	2.71	

Figure 87: Surface roughness parameters

Figure 88 is a 2D profile of the 4.5 GW/cm^2 LSP'ed, 1.2mm thick sample. The highest peak was at 52 µm and the lowest peak was at -22 µm.

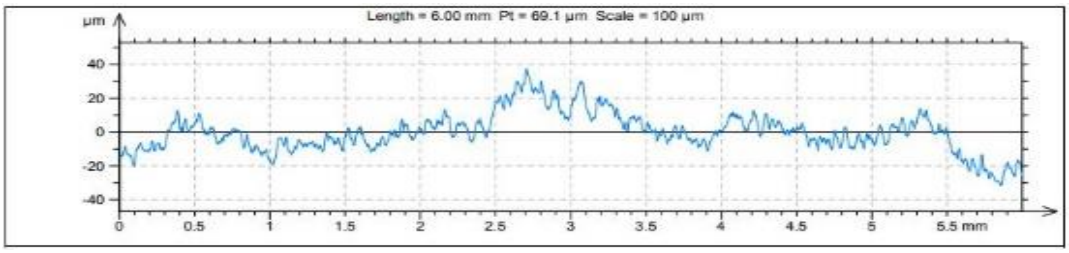

Figure 88: Surface roughness 2D profile

Figure 89 below is a 3D profile extracted from the Hommel report for the 4.5 GW/cm^2 LSP'ed 1.2mm thick samples.

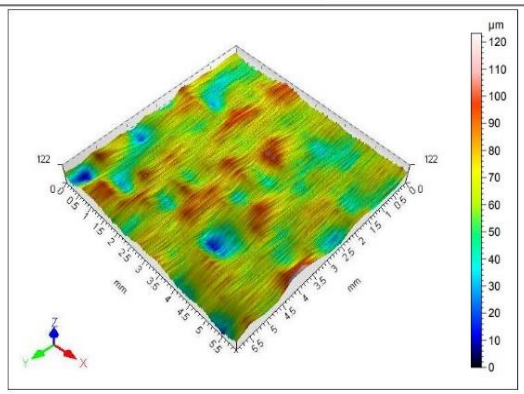

Figure 89: Surface roughness 3D profile

Extracted profile

ISO 4287		
Amplitude parameters - Rc		
Rp	10.9	µm
Rv	9.85	µm
Rz	20.8	µm
Rc	11.2	µm
Rt	27.3	µm
Ra	3.74	µm
Rq	4.50	µm
Rsk	0.152	
Rku	2.54	

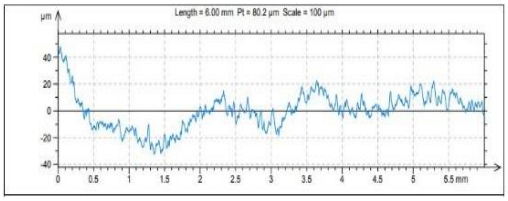

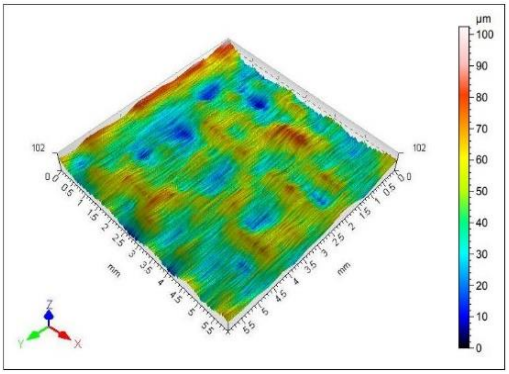

Figure 90: Surface roughness parameters, 2-D and 3-D profiles of 2.6 mm 4.5 GW/cm^2 sample

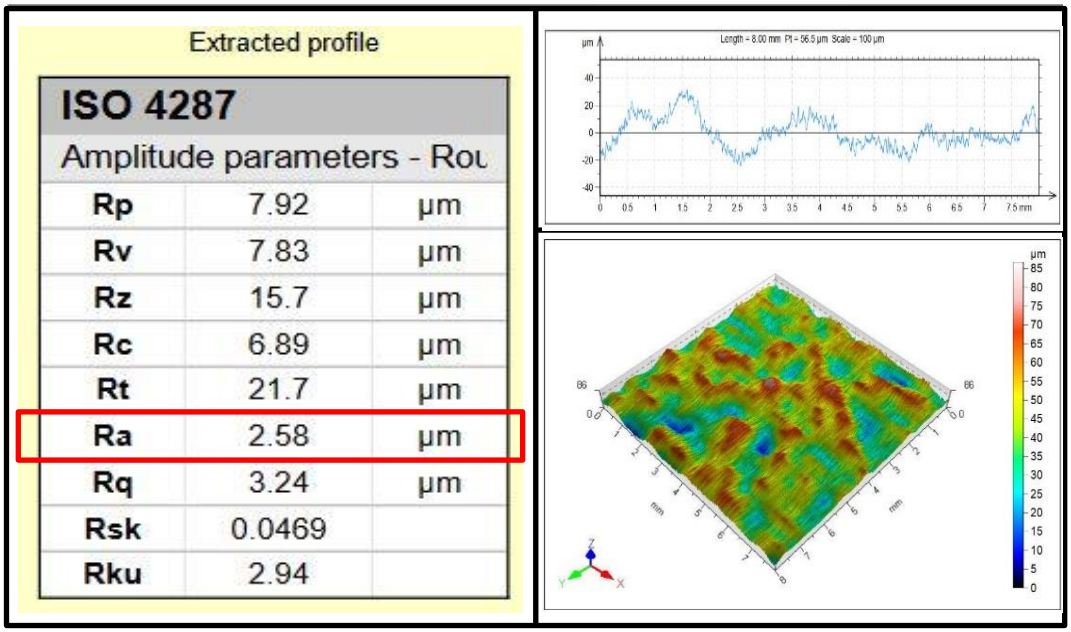

Figure 91: Surface roughness parameters, 2-D and 3-D profiles of 5.6 mm 4.5 GW/cm^2 sample

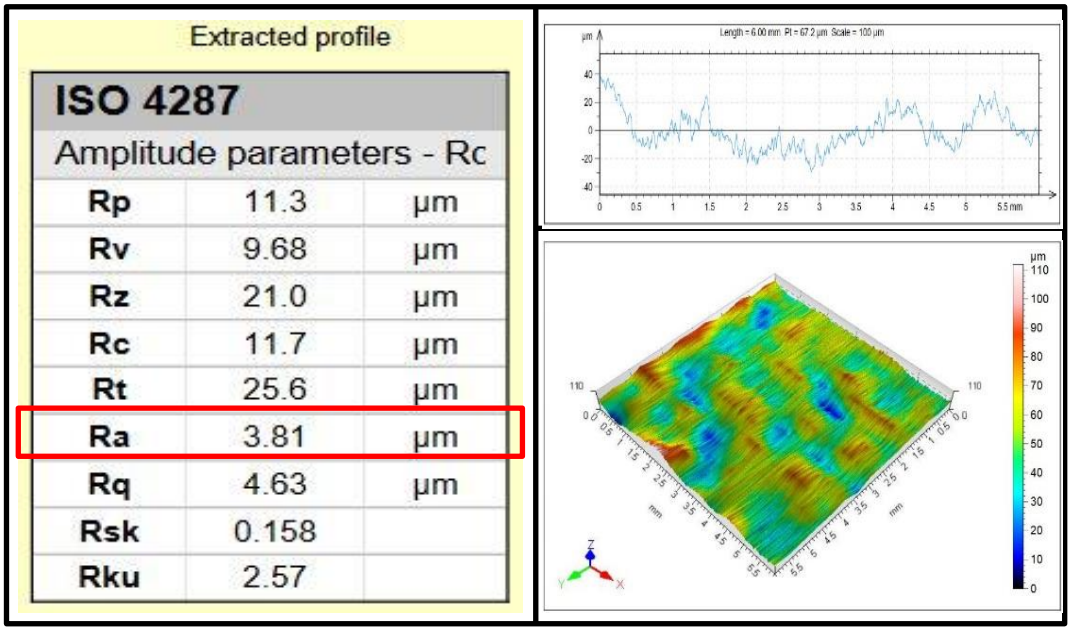

Figure 92: Surface roughness parameters, 2-D and 3-D profiles of 9.6 mm 4.5 GW/cm^2 sample

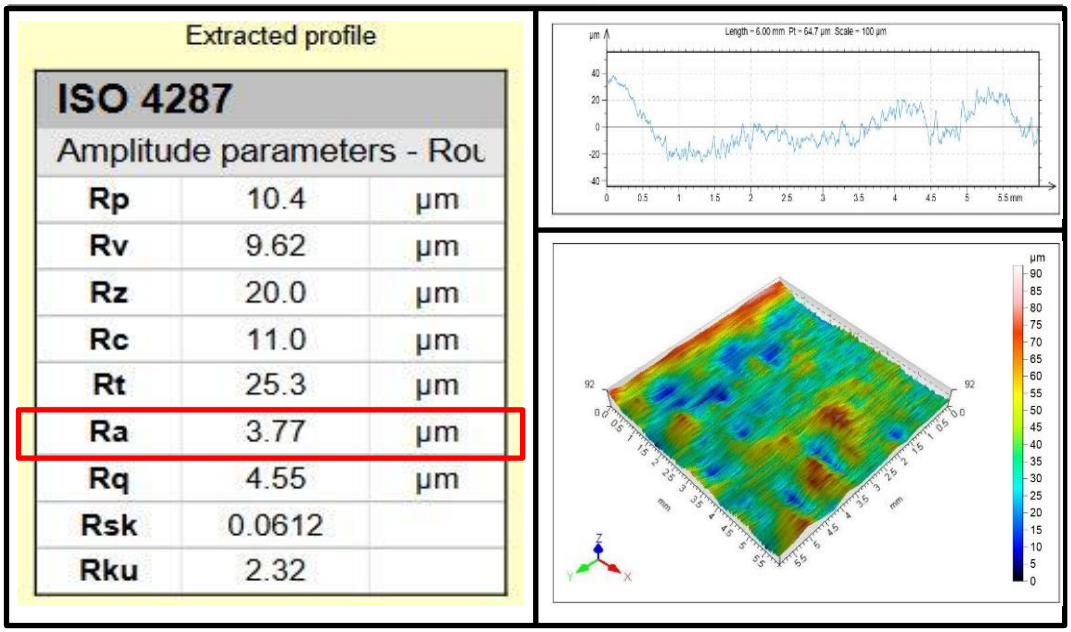

Figure 93: Surface roughness parameters, 2-D and 3-D profiles of 13.6 mm 4.5 GW/cm^2 sample

Chapter 4.4.2: Optical Microscopy Analysis Of 4.5 GW/cm^2 LSP'ed Samples

The optical microscopy of the surface of the 4.5 GW/cm^2 LSP'ed samples is shown below, using the Nikon metallographic camera with a magnification of 1x.

a b c d e

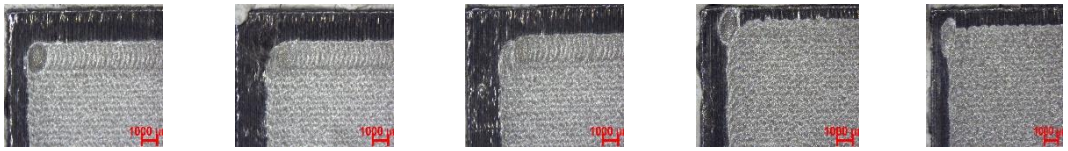

Figure 94: Optical microscopy of surface of 4.5 GW/cm^2 LSP'ed samples (a) 1.2 mm, (b) 2.6 mm, (c) 5.6 mm, (d) 9.6 mm and (e) 13.6 mm

The optical microscopy of the cross-section near the surface of the 4.5 GW/cm^2 LSP'ed samples is shown below, using the Nikon metallographic camera with a magnification of 1x.

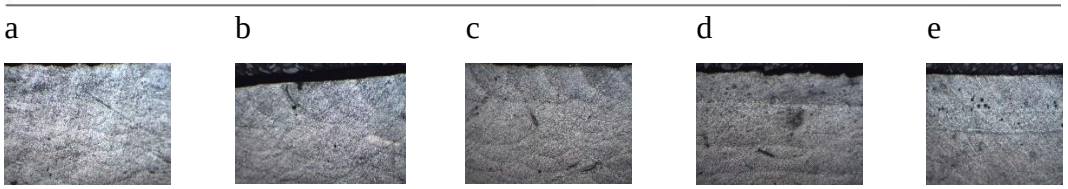

Figure 95: Optical microscopy of cross section of 4.5 GW/cm^2 LSP'ed samples near the surface (a) 1.2 mm, (b) 2.6 mm, (c) 5.6 mm, (d) 9.6 mm and (e) 13.6 mm

The optical microscopy of the cross-section near the middle of the 4.5 GW/cm^2 LSP'ed samples is shown in Figure 96, using the Nikon metallographic camera with a magnification of 1x. The optical microscopy for the 1.2 mm was not available at this time.

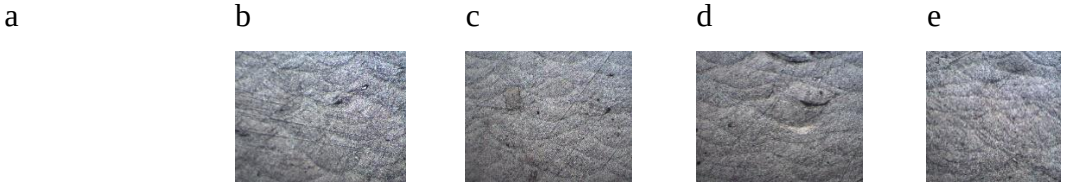

Figure 96: Optical microscopy of cross section of 4.5 GW/cm^2 LSP'ed samples near the middle (a) 1.2 mm, (b) 2.6 mm, (c) 5.6 mm, (d) 9.6 mm and (e) 13.6 mm

The optical microscopy of the cross-section at the interface between the 4.5 GW/cm^2 LSP'ed sample and the baseplate is shown below, using the Nikon metallographic camera with a magnification of 1x.

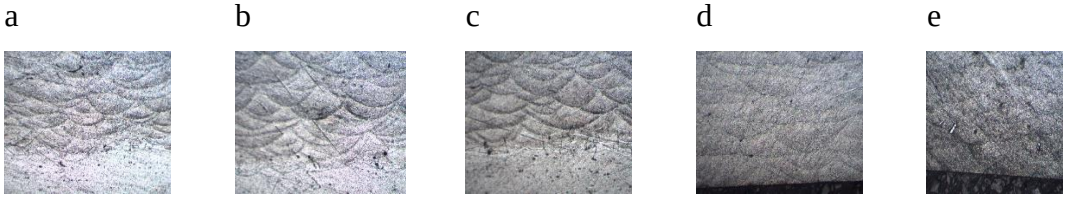

Figure 97: Optical microscopy of cross section of 3.0 GW/cm^2 LSP'ed samples at the interface (a) 1.2 mm, (b) 2.6 mm, (c) 5.6 mm, (d) 9.6 mm and (e) 13.6 mm

Chapter 4.4.3: Scanning Electron Microscopy Of 4.5 GW/cm^2 LSP'ed Sample

Unfortunately, it was not possible to obtain images of the surface of the samples under the SEM due to glue on the surface from residual stress measurements still being on the samples after ultrasonic cleaning. It was also not possible to take

images of the cross-section of the samples, due to the global pandemic of the coronavirus.

Chapter 4.4.4: Microhardness Test Analysis Of 4.5 GW/cm^2 LSP'ed Samples

The microhardness of the material was measured for each thickness with an average indent spacing of 140 µm. The first indent of the samples corresponded to the surface of the material and the last indent corresponded to the side closest to the interface of the AM material and the base plate. The Vickers hardness values for the first 10 indents of the 3.0 GW/cm^2 LSP'ed samples are shown in Table 13. The total length of the sample is approximately 1.4 mm. It is unfortunate that during the cutting of the samples to fit as many as possible on an SEM sample block, the 1.2 mm was cut short, hence it was not possible to go to the end of the number of indents.

Table 13: Microhardness values of 4.5 GW/cm^2 LSP'ed samples.

4.5 GW/cm^2					
Indent	1,2 mm	2,6 mm	5,6 mm	9,6 mm	13,6 mm
1	104,5	114,9	122,5	132,9	147,2
2	106,5	114,4	128,6	130,4	130,5
3	128,8	120,1	145,7	126	130,5
4	124,2	116,9	106,3	129,3	124,7
5	128,7	113,2	136,5	128,6	129,4
6	129,8	118,1	134,9	130,2	133,5
7	126	117,9	146,1	128,9	134,3
8	143,5	116,5	133,2	128,5	131,9
9	143,4	118,9	133,6	126,8	132,3
10	126,5	116,3	126	128,1	124,7

Figure 98 shows the microhardness values plotted against the number of indents.

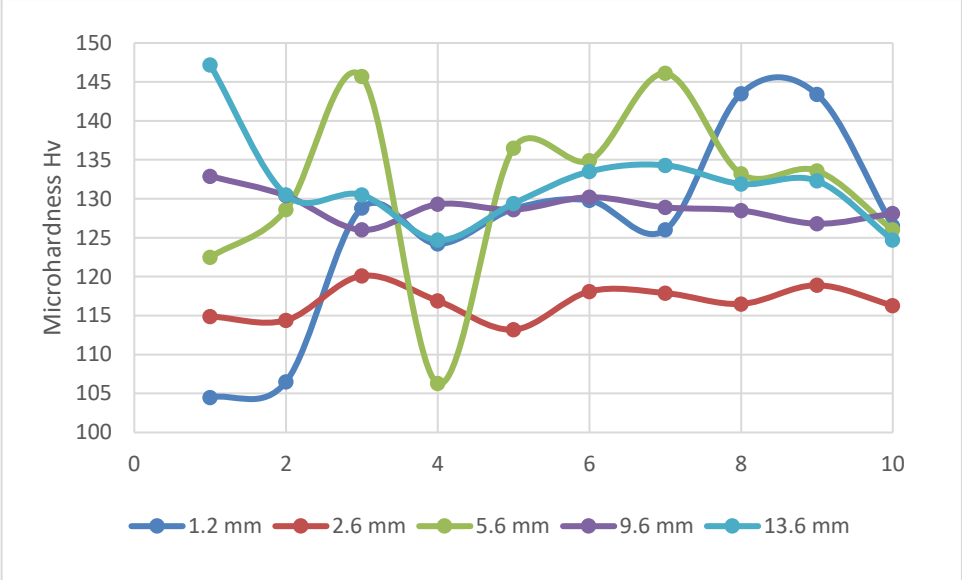

Figure 98: Microhardness values of 4.5 GW/cm^2 LSP'ed samples.

The exact values of microhardness and the indent distance is presented in Appendix D.

Chapter 4.4.5: IHD Results Of 4.5 GW/cm^2 LSP'ed Samples.

This section provides details of the IHD results that were obtained for the 4.5 GW/cm^2 samples. The results are presented with measurements of a hole depth of increment 0.025 mm up until a hole depth of 0.8 mm. The values and corresponding hole depth for all the samples are presented in Appendix E. The five different thicknesses are shown in Table 14.

Table 14: Principal stress values Smax of 4.5 GW/cm^2 LSP'ed samples

4.5 GW/cm^2 samples					
Depth [mm]	1,2 mm	2,6 mm	5,6 mm	9,6 mm	13,6 mm
0,025	19,703	-135,542	34,524	34,524	-0,564
0,075	-58,829	-184,909	-55,179	-55,179	-77,643
0,125	-122,028	-153,36	-141,063	-141,063	-132,255
0,175	-157,415	-132,421	-190,22	-190,22	-165,12
0,225	-172,69	-128,404	-197,357	-197,357	-170,491
0,275	-178,017	-120,594	-189,164	-189,164	-154,931
0,325	-180,399	-97,971	-192,115	-192,115	-140,908

0,375	-181,501	-73,876	-198,926	-198,926	-136,25
0,425	-178,371	-62,046	-188,229	-188,229	-135,895
0,475	-169,506	-56,077	-161,897	-161,897	-131,639
0,525	-156,233	-46,168	-142,428	-142,428	-116,593
0,575	-140,975	-27,679	-136,391	-136,391	-92,441
0,625	-127,218	-3,749	-133,247	-133,247	-72,534
0,675	-116,89	3,62	-124,059	-124,059	-67,725
0,725	-107,365	-13,895	-112,344	-112,344	-70,721
0,775	-93,931	-26,218	-102,876	-102,876	-66,544

Figure 99 shows the maximum principal stress values plotted against the incremental hole depth.

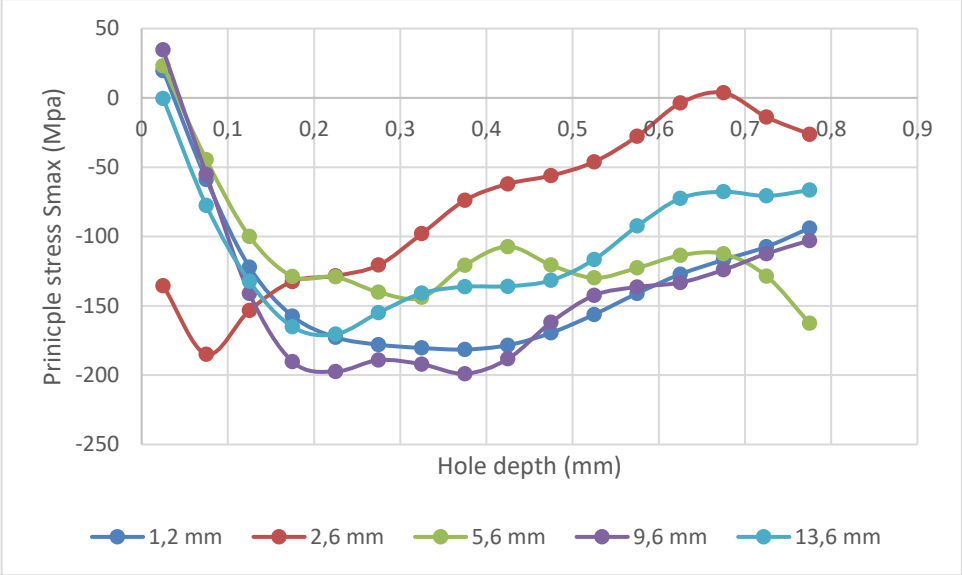

Figure 99: Principal stress Smax of 4.5 GW/cm^2 LSP'ed samples

Chapter 5: Discussion

This section is divided into different sections as listed below and the relevant results discussed

- SLM manufacturing process
- LSP processing
- Surface roughness
- Optical microscope

- FESEM
- Microhardness
- Incremental hole drilling

Chapter 5.1: SLM Manufacturing Process

During the SLM manufacturing process, the baseplate got stuck to the side of the machine which resulted in the heights of the samples being off by approximately 0.4 mm. This discrepancy between manufactured samples and the requested design of the samples did not affect the material behaviour or the LSP surface treatment.

Chapter 5.2: LSP Processing

During the LSP processing, the samples were mounted to the 3axis CNC stage and the focal length was fixed for a fixed spot size. To account for the different thicknesses and to maintain the fixed spot size, the samples needed to be moved along the z-direction of the CNC stage, as this Z-stage is prone to moving in a distorted direction it was important to make sure that the samples remained perpendicular to the laser beam. This was achieved by using a fixed rod relative to the aperture of the laser. It was also important to perform the LSP of all the samples at the same time due to the fluctuation of LSP parameters due to weather effects. Changes in the weather would have changed the laser power which would have affected the peening parameters such as Power Intensity.

Figure 100 shows the side by side comparison of the samples after LSP processing with the different power intensities.

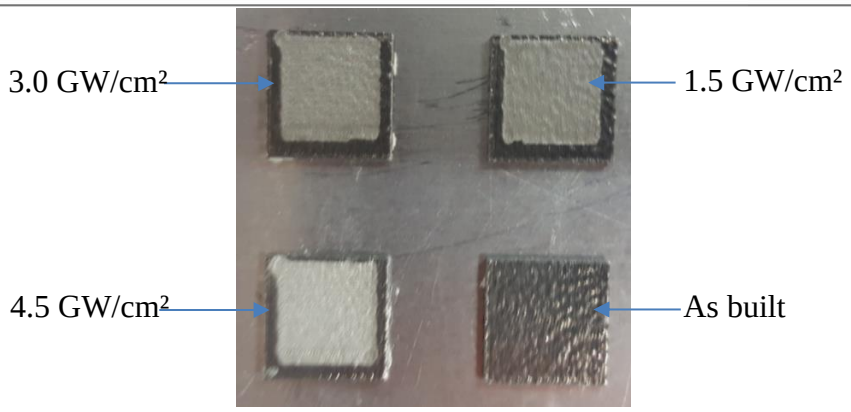

Figure 100: Side by side comparison of LSP

It must be noted that the laser energy during the sample processing remained relatively constant and readers are referred to Appendix B for the tables of the laser energy (mJ) during the processing.

Chapter 5.3: Surface Roughness

The surface roughness of the samples increased with an increase of the power intensity of the LSP process and this corresponds to the literature for AM and LSP [53] and aluminium alloy [48]. It has been noted that for aeronautical applications this increase in surface roughness may not be desirable and that additional post-processing may be needed to improve this surface roughness.

The average surface roughness values (Ra) for each sample is listed in Table 15: Average surface roughness values (Ra).

Table 15: Average surface roughness values (Ra)

Ra Values (um)				
Thickness (mm)	As built	1,5 GW/cm²	3,0 GW/cm²	4.5 GW/cm²
1,2	1,66	2,77	4,13	4,63
2,6	1,97	3,01	3,58	3,74
5,6	2,78	3,9	3,73	2,58
9,6	1,67	2,84	3,64	3,81
13,6	1,89	2,68	3	3,77

Figure 101 is an illustration of the table above of all the average surface roughness (Ra) values for all the samples measured. It is apparent that with an increase in laser power intensity the roughness of the material increased, which is also noted in the

literature [48], [53]. In comparison to previous research conducted, the surface roughness for a peened sample with a power intensity of 6.0 GW/cm^2 was 14.50 µm, while the as-built sample had an average surface roughness of 0.34 µm. The increase in surface roughness for the as-built samples from literature to the samples used in this dissertation indicates that there may have been differences in the SLM process, such as a different powder being used with different chemical composition and the SLM build parameters that the samples were manufactured with.

The trend of the increase of surface roughness by an increase in power intensity of the LSP corresponds to literature as noted in section 1.5 [48], [53]. where the Ra increased from 1.8 µm for a 1.5 GW/cm^2 AA7075-T6 sample to 2.1 µm for a 3.0 GW/cm^2 AA7075-T6 sample.

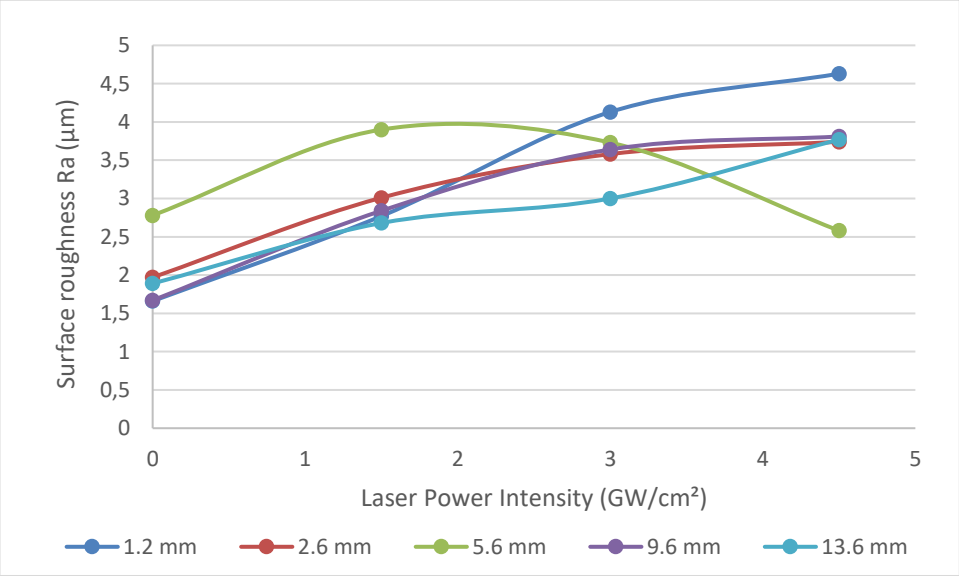

Figure 101: Surface roughness Ra values for each sample

The 2-D profiles of the surface roughness of the as-built samples had a sinusoidal type pattern due to the effect of the SLM finishing process once the material is built to the specification.

For the peened samples, the 1.5 GW/cm^2, 3.0 GW/cm^2 and 4.5 GW/cm^2 samples, the 2-D profiles shared a similarity of having a sinusoidal type pattern which shows the peening effect on the surface of the samples.

The 3-D profiles of the surface roughness of the as-built samples had a sinusoidal type pattern due to the effect of the SLM finishing process once the material is built to the specification.

For the peened samples, the 1.5 GW/cm^2, 3.0 GW/cm^2 and 4.5 GW/cm^2 samples, the 2-D profiles shared a similarity of having a sinusoidal type pattern which shows the peening effect on the surface of the samples.

Chapter 5.4: Optical Microscopy

From the images taken of the surface of each one of the samples, it was noted that there was an increase in the depth of the craters created on the surface with an increase in power intensity. This corresponds to the literature [48] which noted that these impact craters created different material oxides on the surface of the material.

The images of the cross-section of the samples show that there was material that had not properly melted and upon cooling it created defects within the material, as shown in Figures 102, 103 and 104.

An image of the cross-section of the 5.6 mm thick sample that was peened at 4.5 GW/cm^2, at 20X magnification, shows that there is a material that was not properly heated during the SLM process. It is important to note that the cross-section of the material has a semi-circular patterning material build-up to it which corresponds to the literature [55]. After discussion with the manufacturer, it was noted that this is due to the SLM process itself for aluminium and the way that tracks of melted material are formed and only appears for aluminium and is not present in other materials such as titanium.

Figure 102 is an image of the cross-section, at the middle of the 5.6mm, 4.5 GW/cm^2 sample under 20X magnification. It shows the solidified defect within the sample. It is theorised that this defect is due to the material not decomposing correctly during the SLM process and that it formed after solidification.

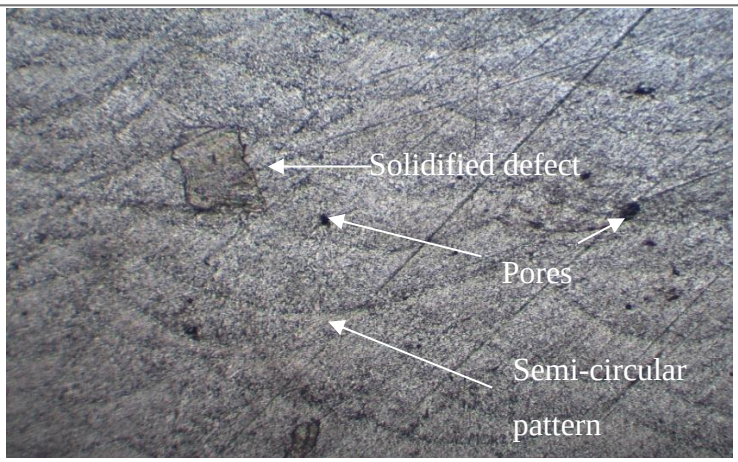

Figure 102: Cross-section of sample 5.6mm 4.5 GW/cm²

Figure 103 is an image of the cross-section, at the interface between the baseplate and the AM material which was the 2.6 mm, 3.0 GW/cm² sample under 20X magnification. It shows the typical semi-circular pattern as noted from the literature [55] for AM AlSi10Mg as well as a solidified defect within the sample.

Figure 103: Cross-section of sample 2.6mm 3.0 GW/cm² interface

Figure 104 is an image of the middle of the cross-section of the 2.6mm 3.0 GW/cm², under 20X magnification. The image shows cracking within the sample after manufacturing as well as defects. It is theorized that the cracks are due to the residual stress from manufacturing.

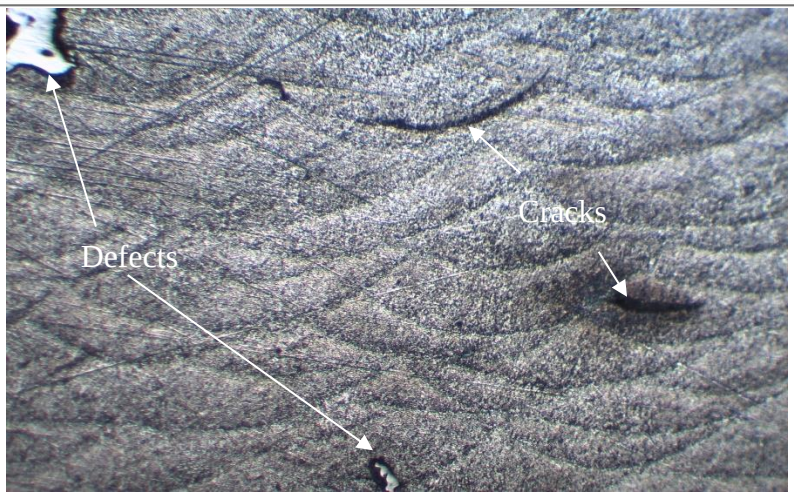

Figure 104: Cross-section of sample 2.6mm 3.0 GW/cm² middle

As mentioned previously the semi-circular patterning on the material is due to the track formation during the SLM process and is not present in other materials. It is speculated that this is due to the materials low melting and cooling point as compared to materials such as titanium and tool steel.

Comparing the as-built sample to the LSPeend samples it is noticed that there is a packing of the grains as shown in Figure 105, for an increase in power intensity of the LSP.

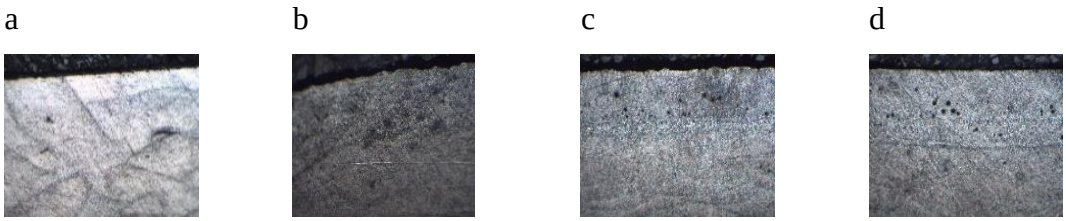

Figure 105: Optical microscopy comparison of 13.6 mm thickness samples, as-built (a), 1.5 GW/cm^2 (b), 3.0 GW/cm^2 (c) and 4.5 GW/cm^2

From the metallographic images for the peened samples, there appears to be a slight discolouration at the surface which corresponds to the LSPeened affected portion of the sample. This trend of the packing of the grains corresponds to the images of section 1.6 specifically Figure 16 [53].

Chapter 5.5: FESEM

It was unfortunate that surface images of the samples could not be taken due to the remainder of glue on the samples, which was not removed by the ultrasonic bath. Also due to the global pandemic of the coronavirus, it was not possible to take images of the cross-sections at this time. For the image obtained it was apparent to see the pores within the 2.6 mm thick as-built sample.

Chapter 5.6: Microhardness

Analysing the as-built samples' microhardness profiles the average of the Vickers microhardness was approximately 124 Hv, at 500 gf, which corresponds to the material data sheet supplied by SLM [77], which had a hardness of 125 Hv for AlSi10Mg. Comparing this value of the average Vickers hardness to the sample used in the literature [53], 88.79 Hv, at 200 gf, it is apparent that the samples for this work were harder than published literature.

Comparing the data for the 1.5 GW/cm^2 samples, the highest value of Vickers hardness was 165 Hv at a depth of 280 µm from the surface, for the 1.2 mm thick sample, indicating an increase of 41 Hv from the as-built samples, which is a 33% increase. The other samples experienced an increase of 9% for the 2.6 mm thick sample, a decrease of 13.6% for the 5.6 mm sample, 0% for the 9.6 mm sample and a 5% increase for the 13.6 mm sample, at the 280 µm depth respectively. It is suspected that for the 5.6 mm the indenter had hit a defect within the material resulting in a 13.6% decrease in microhardness. For the 1.2 mm, 2.6 mm and 13.6 mm it is theorized that the LSP had an effect of packing the grains which increased the hardness.

Comparing the data for the 3.0 GW/cm^2 samples the highest value of Vickers microhardness was 165 Hv at a depth of 280 µm from the surface, for the 13.6 mm sample, indicating an increase of 41 Hv from the as-built samples, which is a 33% increase. The other samples experienced a decrease of 4% for the 1.2 mm thick sample, a decrease of 17% for the 2.6 mm sample, an increase of 2% for the 5.6 mm sample and a 12% decrease for the 9.6 mm sample, at the 280 µm depth

respectively. It is postulated that the 2.6- and 9.6-mm samples themselves were not as hard as the as-built samples before peening and that the trend of the hardness through the samples indicated an increase in hardness through the depth of the samples.

Comparing the data for the 4.0 GW/cm^2 samples the highest value of Vickers hardness was 147 Hv at a depth of 140 µm from the surface, for the 13.6 mm sample, indicating an increase of 23 Hv from the as-built sample, which is an 18% increase. The other samples experienced a decrease of 15% for the 1.2 mm thick sample, a decrease of 7% for the 2.6 mm sample, a decrease of 1% for the 5.6 mm sample and a 7% increase for the 9.6 mm sample, at the 140 µm depth respectively. It is postulated that the 2.6 mm sample was not as hard as the as-built samples before peening and that the trend of the hardness through the sample was relatively constant through the depth of the sample. It is postulated that the effect of the LSP was not noticeable on this sample for microhardness.

Comparing the increase in hardness to the published literature (the hardness had an increase of 25.9% for an LSP of 6 GW/cm^2 [53]), it is apparent that there is an increase of microhardness due to LSP. However, it does not appear to be a linear relationship where an increase in PI corresponds to a higher increase of microhardness. The microhardness had an increase of 33% for the 1.5 and 3.0 GW/cm^2 peening parameters and an 18% increase in microhardness for the 4.5 GW/cm^2. From literature [53] there was an increase of 25% for a 6 GW/cm^2 peening parameter.

In general, the increase in microhardness is attributed to an increase in the dislocation density and changes in the grain structure caused by the deformation done by the LSP induced shock wave.

Chapter 5.7: Incremental Hole Drilling

The results for the IHD are very interesting as the residual stress from the as-built manufactured samples has an inherent tensile residual stress which corresponds to the literature in Chapter 1. The oscillating nature of the stress that Salmi et al. [10]

reported was not noticed except for the 1.2 mm thick as-built sample. For the 1.2 mm thick as-built sample, the maximum tensile stress was approximately 350 MPa at the hole depth of 0.025 mm and continued decreasing in an oscillating fashion to 180 MPa at a hole depth of 0.775 mm.

The maximum tensile residual stress for the as-built samples was 350 MPa for the 1.2 mm thick sample at the surface of the sample. The other as-built samples peaked at 271 MPa for the 2.6 mm thick, 301 MPa for the 5.6 mm thick, 237 MPa for the 9.6 mm thick and 272 MPa for the 13.6 mm thick samples. In the first 0.15 mm of the depth of the as-built samples, the tensile stress increases rapidly from about 150 MPa to around 300 MPa. Thereafter the residual stresses become gradually less tensile but remain so through the entire depth of the measurement for all the different thicknesses.

Peening the samples at 1.5 GW/cm^2 resulted in the tensile residual stresses being removed and compressive residual stresses being induced in the samples for all thicknesses. In the first 0.15 mm of depth, the compressive stress increases rapidly from about 60 MPa to around -90 MPa for the 1.2 mm thick sample and gradually became less in compression until approximately 0.55 mm of hole depth. For the 2.6, 5.6 and 9.6 mm samples the samples remained in compression until a hole depth of approximately 0.55 – 0.6 mm. For the 13.6 mm thick sample, the residual stress remained in compression through the 0.8 mm hole depth.

The maximum compressive residual stress was 112 MPa for the 13.6 mm thick sample at 0.375 mm from the surface of the sample. The other samples had a maximum compressive residual stress of 91 MPa for the 1.2 mm thick, 78 MPa for the 2.6 mm thick, 94 MPa for the 5.6 mm thick and 101 MPa for the 9.6 mm thick samples. Comparing the 13.6 mm thick samples, there was a reduction from 272 MPa tensile stress in the as-built sample to -112 MPa in the 1.5 GW/cm^2 sample, which is a change of 384 MPa.

Peening the samples at 3.0 GW/cm^2 resulted in the tensile residual stresses being removed and compressive residual stresses being induced in the samples for all thicknesses. In the first 0.25 mm of hole depth, the compressive stress increases

rapidly from about 20 MPa to around -160 MPa for the 2.6, 5.6 and 9.6 mm thick samples and gradually became less in compression for the remainder of the test. For the 13.6 mm thick sample, the residual stress shot to a maximum compressive stress of 153 MPa at approximately 0.15 mm of hole depth, before gradually decreasing in compressive stress for the remainder of the test.

The maximum compressive residual stress was 155 MPa for the 9.6 mm thick sample at 0.225 mm from the surface of the sample. The other samples had a maximum compressive residual stress of 140 MPa for the 1.2 mm thick, 147 MPa for the 2.6 mm thick, 146 MPa for the 5.6 mm thick and 153 MPa for the 13.6 mm thick samples. Comparing the 9.6 mm thick samples, there was a reduction from a 237 MPa tensile stress in the as-built sample to maximum-compressive residual stress of 155 MPa in the 3.0 GW/cm^2 sample, which is a change of 392 MPa.

Peening the samples at 4.5 GW/cm^2 resulted in the tensile residual stresses being removed and compressive residual stresses being induced in the samples for all thicknesses. In the first 0.2 mm of hole depth, the compressive stress increases rapidly from about 30 MPa to around -200 MPa for the 1.2, 5.6, 9.6 and 13.6 mm thick samples and gradually became less in compression for the remainder of the test. For the 2.6 mm thick sample, the residual stress shot to a minimum of -181 MPa at approximately 0.05 mm of hole depth, before gradually decreasing in compressive stress for the remainder of the test.

The maximum compressive residual stress was 198 MPa for the 9.6 mm thick sample at 0.375 mm from the surface of the sample. The other samples had a maximum compressive residual stress of 181 MPa for the 1.2 mm thick, 184 MPa for the 2.6 mm thick, 162 MPa for the 5.6 mm thick and 170 MPa for the 13.6 mm thick samples. Comparing the 9.6 mm thick samples, there was a reduction from 237 MPa tensile stress in the as-built sample to 198 MPa compressive stress in the 4.5 GW/cm^2 sample, which is a change of 435 MPa.

Comparing the 9.6 mm thick samples the as-built sample had a maximum tensile residual stress of 237 MPa and had a maximum compressive residual stress of 101 MPa for the 1.5 GW/cm^2, 155 MPa for the 3.0 GW/cm^2 and 198 MPa for the 4.5

GW/cm^2. The change in stress was 143% for the 1.5 GW/cm^2, 165% for the 3.0 GW/cm^2 and 183% for the 4.5 GW/cm^2. This shows a trend of an increase in power intensity there is a corresponding increase in compressive residual stress. This pattern was noticed in all the other thicknesses.

Comparing the trend of the 9.6 mm thick sample, figure 106, it is apparent that the curve of the residual stress after peening shifted upward which is attributed to the fact that there is less elastic material to respond to the plastic deformation induced by LSP. This corresponded to the trend for AA7075 [48].

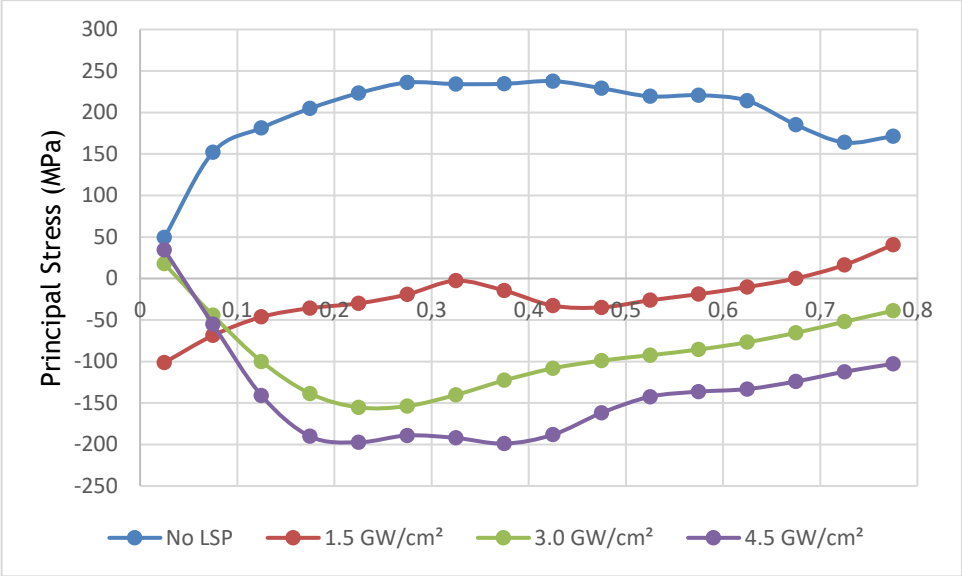

Figure 106: Principal stress Smax of 9.6 mm thick sample

Chapter 6: Conclusions

This section provided concluding remarks of the project.

- LSP improved the material properties such as microhardness of the AM AlSi10Mg samples.
- The surface roughness of AM samples increased with an increase in the laser power intensity of the LSP.
- There were no surface defects of the AM samples that were processed after LSP.

- There were defects within the cross-section of the AM samples, such as material not properly melting before resolidification, pores and cracks within some samples.
- The microhardness at the surface of AM samples was improved by an increase of 33% for the 1.5 and 3.0 GW/cm^2 peening parameters and an 18% increase in microhardness for the 4.5 GW/cm^2.
- The residual stress of the as-built AM samples was in a tensile state and after the LSP processing, the residual stress improved to a compressive state.
- The change in stress was 143% for the 1.5 GW/cm^2, 165% for the 3.0 GW/cm^2 and 183% for the 4.5 GW/cm^2 for the 9.6 mm thick sample.
- An increase in laser power intensity corresponded to an increase in compressive residual stress.

Chapter 7: Future Work And Recommendations

The LSP should be performed with a coating such as vinyl tape to improve the surface roughness of the samples. The inclusion of the vinyl tape coating could have the effect of reducing the surface roughness after LSP.

A post-processing method that is not subtractive, such as milling, should be found to improve the surface roughness of the samples for aeronautical applications. By finding a different post-processing method instead of LSP, to improve the surface roughness would benefit the study to conform to the aviation standards of surface roughness for SLM parts.

A side by side comparison of the cross-section of the as-built AM samples and the AM samples after LSP should be done under the FESEM at a constant magnification of 100X, to better illustrate the improvement of the porosity of the material due to LSP.

An alternative etching agent which can illustrate the microstructure of the additive manufacturing sample under the FESEM should be found.

An XRD analysis of the samples may prove insightful to observe the improvement of the residual stress due to LSP at the surface of the samples.

Chapter 8: Contribution To Knowledge

Part of this work was presented at the 20th Annual International Conference of Rapid Product Development Association of South Africa (RAPDASA) in November 2019. The abstract of the conference presentation is presented in Appendix F.

References

[1] "Spot light metal," [Online]. Available: https://www.spotlightmetal.com/what-is-additive-manufacturing-a-796337/. [Accessed 28 April 2021].

[2] [Online]. Available: Additive manufacturing (AM) or additive layer manufacturing (ALM) is the industrial production name for 3D printing, a computer controlled process that creates three dimensional objects by depositing materials, usually in layers.. [Accessed 28 April 2021].

[3] S. Kumar, A. K. Choudray, A. Singh and A. K. Gupta, "A Comparison of Additive Manufacturing Technologies," *International Journal for Innovative Research in Science & Technology,* vol. 3, no. 1, pp. 147-152, 2016.

[4] D. Bourell, J. P. Kruth, L. Ming, G. Levy, D. Rosen, M. A. Beese and A. Clare, "Materials for additive manufacturing," *CIRP Annals - Manufacturing Technology,* vol. 1, no. 66, pp. 659-681, 2017.

[5] "3D Printing / Additive Manufacturing Using Polymers - Complete Guide," Omnexus Special Chem, [Online]. Available: https://omnexus.specialchem.com/selection-guide/3d-printing-and-additive-manufacturing-polymers-and-processes. [Accessed 28 April 2021].

[6] "What is Additive Layer Manufacturing (ALM)?," Farinia Group, [Online]. Available: https://www.farinia.com/blog/what-additive-layer-manufacturing-alm. [Accessed 28 April 2021].

[7] C. K. Chua, K. F. Leong and C. S. Lim, Rapid prototyping: principles and applications, Singapore: World Scientific Publishing Co , 2003.

[8] D. Kazmer, "Three-Dimensional Printing of Plastics," in *Applied Plastics Engineering Handbook,* Lowell, Massachusetts, University of Massachusetts, pp. 617 - 633.

[9] "Selective Laser Melting (SLM) – 3D Printing Simply Explained," All 3D, [Online]. Available: https://all3dp.com/2/selective-laser-melting-slm-3d-printing-simply-explained/. [Accessed 28 April 2021].

[10] A. Salmi, E. Atzeni, L. Iuliano and M. Galati, "Experimental analysis of residual stresses on AlSi10Mg parts produced by means of Selective Laser Melting (SLM)," *10th CIRP Conference on Intelligent Computation in Manufacturing Engineering - CIRP ICME '16,* pp. 458 - 463, 2017.

[11] X. Yu and L. Wang, "T6 heat-treated AlSi10Mg alloys additive-manufactured by selective laser melting," *Procedia Manufacturing,* vol. 15, p. 1701–1707, 2018.

[12] J. P. Kruth, J. Deckers, E. Yasa and R. Wauthle, "Assessing and comparing influencing factors of residual stresses in selective laser melting using a novel analysis method," *Proceedings of the Institution*

of Mechanical Engineers,Part B: Journal of Engineering Manufacture, vol. 226, no. 6, pp. 980-991, 2012.

[13] X. Gan, G. Fei, J. Wang, Z. Wang, M. Lavorgna and H. Xia, "Powder quality and electrical conductivity of selective laser sintered polymer composite components," in *Structure and Properties of Additive Manufactured Polymer Components*, Woodhead Publishing, 2020, pp. 149-185.

[14] "Rapid Made," 10 7 2015. [Online]. Available: https://www.rapidmade.com/rapidmade-blog/2015/7/10/whats-the-difference-between-selective-laser-sintering-sls-and-selective-laser-melting-slm. [Accessed 1 2 2021].

[15] "How the Next Gen of Affordable Systems Is Making PBF 3D Printing Available to All," AMS 3-D, 11 March 2018. [Online]. Available: https://www.ams3d.co.za/news/how-the-next-gen-of-affordable-systems-is-making-pbf-3d-printing-available-to-all. [Accessed 28 April 2021].

[16] "What is Laminated Object Manufacturing?," Live Science, 2014. [Online]. Available: https://www.livescience.com/40310-laminated-object-manufacturing.html. [Accessed 28 April 2021].

[17] "Star rapid," [Online]. Available: https://www.starrapid.com/blog/top-7-methods-for-making-3d-rapid-prototypes/. [Accessed 1 2 2021].

[18] "How to Compare the Various Metal 3D Printing Processes," Fabbaloo, 10 November 2017. [Online]. Available: https://www.fabbaloo.com/blog/2017/11/10/how-to-compare-the-various-metal-3d-printing-processes. [Accessed 28 April 2021].

[19] B. Dutta, S. Palaniswamy, J. Choi, L. J. Song and J. Mazumder, "Additive Manufacturing by Direct Metal Deposition," *Advanced materials and processes,* pp. 33-36, May 2011.

[20] "Open learn," [Online]. Available: https://www.open.edu/openlearn/science-maths-technology/engineering-technology/manupedia/direct-metal-deposition-dmd. [Accessed 1 2 2021].

[21] "Engineering 360," [Online]. Available: https://www.globalspec.com/reference/46877/203279/Purpose-of-Making-Alloys. [Accessed 1 2 2021].

[22] N. T. Aboulkhair, M. Simonelli, L. Parry, I. Ashcroft, C. Tuck and R. Hague, "3D printing of Aluminium alloys: Additive Manufacturing of Aluminium alloys using selective laser melting," *Progress in material science,* vol. 106, 2019.

[23] J. J. Lewandowski and M. Seifi, "Metal additive manufacturing: a review of mechanical properties," *Annual revision of materials research,* vol. 46, pp. 151-186, 2016.

[24] N. Kaufman, "Influence of process parameters on the quality of aluminium alloy EN AW 7075 using selective laser melting (SLM).," *Physucs Procedia,* vol. 83, pp. 918-926, 2016.

[25] M. Alimardani, E. Toyserkani, J. P. Huissoon and C. P. Paul, "On the delamination and crack formation in a thin wall fabricated using laser solid freeform fabrication process," *Optics and Lasers in engineering,* vol. 47, pp. 1160-1168, 2009.

[26] J. Bradbury, "Aerospace and Defense Technology," 1 December 2017. [Online]. Available: https://www.aerodefensetech.com/component/content/article/adt/features/articles/27957?start=1. [Accessed 11 November 2019].

[27] Polese, "CPAM Proposal 2019-2020," University of the Witwatersrand, Johannesburg, 2019.

[28] Wikipedia, "Hot Isostatic Pressing," [Online]. Available: https://en.wikipedia.org/wiki/Hot_isostatic_pressing. [Accessed 15 November 2019].

[29] S. o. M. Engineers, "Shot Peening," in *Tool and manufacturing engineers handbook*, 1985.

[30] S. s. p. a. c. international, "Finishing treatments ultrasonic shot peening," Superior shot peening and coating international, [Online]. Available: https://superiorshotpeening.com/services/finishing-treatments/ultrasonic-shot-peening. [Accessed 15 November 2019].

[31] Wikipedia, "Laser peening," [Online]. Available: https://en.wikipedia.org/wiki/Laser_peening. [Accessed 15 November 2019].

[32] P. Shukla, P. Swanson and C. Page, "Laser Shock Peening and Mechanical Shot Peening Processes Applicable for the Surface Treatment of Technical Grade Ceramics: A Review..," *Journal of Engineering Manufacture,* vol. 10, 2014.

[33] G. K. Abdullahi and M. Mamoun, "Laser Peening Process and Its Impact on Materials Properties in Comparison with Shot Peening and Ultrasonic Impact Peening," *Materials (Basel),* vol. 7, no. 12, p. 7925–7974, 2014.

[34] P. Xinlei, L. Xiang, Z. Liucheng, F. Xiaotai, L. Sihai and H. Weifeng, "Effect of Residual Stress on S–N Curves and Fracture Morphology of Ti6Al4V Titanium Alloy after Laser Shock Peening without Protective Coating," *Materials (Basel),* vol. 12, no. 22, p. 3799, 2019.

[35] M. M. Ayman, H. F. Mohamed and O. S. Salah, "Effect of laser shock peening on the hardness of AL-7075 alloy," *Journal of King Saud University – Science,* vol. 31, pp. 472-478, 2019.

[36] A. Kanjer, L. Lavisse, V. Optasanu, P. Berger, C. Gorny, P. Peyre, F. Herbst, O. Heintz, N. Geoffroy, T. Montesin and M. C. Lucas, "Effect of laser shock peening on the high temperature oxidation resistance of titanium.," *Surface and Coatings Technology,* vol. 326, 2017.

[37] H. Lim, P. Kim, H. Jeong and S. Jeong, "Enhancementofabrasion and corrosion resistance of duplex stainless steel by laser shock peening,," *Journal of Materials Processing Technology,* vol. 10, 2010.

[38] A. King, A. Steuwer, C. Woodward and P. J. Withers, "Effects of fatigue and fretting on residual stresses introduced by laser shock peening," *Materials Science and Engineering* , vol. 12, no. 18, p. 435–436 , 2006.

[39] M. James, D. Hughes, Z. Chen, H. Lombard, D. G. Hattingh, D. Asquith, J. R. Yates and P. Webster, "Residual stresses and fatigue performance," *Engineering Failure Analysis*, vol. 14, pp. 384-395, 2006.

[40] R. Gould, ""The LASER, Light Amplification by Stimulated Emission of Radiation".," in *The Ann Arbor Conference on Optical Pumping, the University of Michigan*, Michigan, 1959.

[41] "College Physics," [Online]. Available: https://opentextbc.ca/physicstestbook2/chapter/limits-of-resolution-the-rayleigh-criterion/. [Accessed 19 02 2020].

[42] "Photonics Mecia," [Online]. Available: https://www.photonics.com/Articles/Lasers_Understanding_the_Basics/a25161. [Accessed 19 02 2020].

[43] Y. Sano, N. Mukai, K. Okazaki and M. Obata, "Residual stress improvement in metal surface by underwater laser irradiation," *Nuclear Instruments and Methods in Physics Research Section B: Beam Interactions with Materials and Atoms*, vol. 121, pp. 432-436, 1997.

[44] J. Daly, J. R. Harrison and L. Hackel, "New laser technology makes lasershot peening commercially affordable," *The Seventh International Conference on Shot Peening*, pp. 379- 386, 1999.

[45] S. Physics, *Quanta Ray ND:Yag laser family*, Spectra Physics.

[46] K. Ding and L. Ye, Laser shock peening Performance and process selection, Cambridge: Woodhead Publishing , 2006.

[47] A. Arif, " Numerical prediction of plastic deformation and residual stresses induced by laser shock processing," *Materials Processing Technology*, vol. 136, no. 120, p. 38, 2003.

[48] S. v. Sean, Residual Stress Measurement and Parametric Analysis of Laser Shock Peening of Aluminium Alloy 7075 with Different Thicknesses, Johannesburg: University of the Witwatersrand, 2018.

[49] "LSP Technologies," [Online]. Available: https://www.lsptechnologies.com/why-laser-peening/shot-peening-vs-laser-peening/. [Accessed 01 02 2021].

[50] H. Xuesong, Z. Haihong, X. Nie, G. Wang and X. Zeng, "Investigation on Selective Laser Melting AlSi10Mg Cellular Lattice Strut: Molten Pool Morphology, Surface Roughness and Dimensional Accuracy," *MDPI*, vol. 11, no. 392, pp. 2 -13, 2019.

[51] A. Charles , A. Elkaseer, L. Thijs, V. Hagenmeyer and S. Scholz, "Effect of Process Parameters on the Generated Surface Roughness of Down-Facing Surfaces in Selective Laser Melting," *Applied Sciences*, vol. 9, p. 1256, 2019.

[52] Y. Sano, K. AKITA, . K. MASAKI, Y. OCHI, I. ALTENBERGER and . B. SCHOLTES, "Laser Peening without Coating as a Surface Enhancement Technology," *Journal of Laser Micro/Nanoengineering* , vol. 1, no. 3, pp. 161-166, 2006.

[53] N. N. Kumar and A. C. Yadav, "Laser Shock Peening on Al-Si10-Mg Produced by DMLS Technique," *Materials Today: Proceedings*, vol. 22, no. 1, p. 2916–2925, 2020.

[54] "Wikipedia," [Online]. Available: https://en.wikipedia.org/wiki/Optical_microscope. [Accessed 19 02 2020].

[55] A. H. Maamoun, M. Elbestawi, G. K. Dosbaeva and S. C. Veldhuis, "Thermal Post-processing of AlSi10Mg parts produced by Selective Laser Melting using recycled powder," *Additive Manufacturing*, vol. 21, pp. 234-247, 2018.

[56] S. Huang, Z. Wang, J. Sheng, E. Boateng, M. Lui, X. Yang and J. Zhou, "Residual Stress Distribution and Microstructure Evolution of AA 6061-T6 Treated by Warm Laser Peening," *Metals*, vol. 6, no. 11, p. 292, 2016.

[57] C. Donley, "Corsera," Research Triangle Nanotechnology Network, [Online]. Available: https://www.coursera.org/lecture/nanotechnology/scanning-electron-microscopy-basic-function-WE2fL. [Accessed 19 02 2020].

[58] R. Zhu, H. Xie, J. Zhu, Y. Li, Z. Che and S. Zou, "A micro-scale strain rosette for residual stress measurement by SEM Moir method," *Science China Physics, Mechanics and Astronomy*, vol. 57, 2014.

[59] K. Ding and L. Ye, Laser Shock Peening Performance and Process Simulation, Cornwall: Woodhead Publishing Limited, 2006.

[60] L. P. Lam, D. Q. Zhang, Z. H. Liu and C. K. Chua, "Phase analysis and microstructure characterization of AlSi10Mg parts produced by Selective Laser Melting," *Virtualand Physical Prototyping*, vol. 10, no. 1, 2015.

[61] S. Sathyajith, S. Kalainathan and S. Swaroop, "Laser Peening Without Coating on Aluminum Alloy Al-6061-T6 Using Low Energy Nd:YAG Laser," *Optics & Laser Technology*, vol. 45, no. 1, p. 389–394, 2012.

[62] "Non Destructive Testing Resource Centre," [Online]. Available: https://www.nde-ed.org/EducationResources/CommunityCollege/Materials/Mechanical/Hardness.htm. [Accessed 19 02 2020].

[63] "Wikipedia," [Online]. Available: https://en.wikipedia.org/wiki/Hardness. [Accessed 19 02 2020].

[64] "Encyclopedia of Britannica," [Online]. Available: https://www.britannica.com/science/Vickers-hardness. [Accessed 19 02 2020].

[65] "Engineering Clicks," [Online]. Available: https://www.engineeringclicks.com/vickers-hardness-test/. [Accessed 19 02 2020].

[66] M. F. Hameed and S. Obayya, "Effect of Laser Shock Peening on the Hardness of AL-7075 Alloy," *Journal of King Saud University - Science*, 2017.

[67] F. A. Kandil, J. D. Lord and P. V. Grant, A Review of Residual Stress Measurement Methods, 1st ed., Teddington: Controller o fHMSO, 2001.

[68] A. International, *Standard Test Method for Determining Residual Stresses by the Hole-Drilling Strain-Gauge Method*, 2013.

[69] "Perfection Machinery," [Online]. Available: https://www.perfectionmachinery.com/used-inventory/slm-slm-280-hl-38170/. [Accessed 19 02 2020].

[70] "Multi station," [Online]. Available: https://www.multistation.com/second-life/slm-280/. [Accessed 19 02 2020].

[71] H. Ye, "An Overview of the Development of Al-Si-Alloy Based Material for Engine Applications.," *Journal of Materials Engineering and Performance*, vol. 12, pp. 288-297, 2003.

[72] A. K. Gupta, D. J. Lloyd and S. Court, "Precipitation hardening in Al–Mg–Si alloys with and without excess Si.," *Materials Science and Engineering*, vol. 316, p. 11–17, 2001.

[73] S. Solutions, *3D Metals Discover the variety of Metal Powders*, SLM Solutions.

[74] C. Y. Yap, C. Chua, Z. Dong, Z. Liu, D. Zhang, L. E. Loh and S. L. Sing, "Review of selective laser melting: Materials and applications," *Applied Physics Reviews*, vol. 2, 2015.

[75] K. Kempen, L. Thijs, J. Van Humbeeck and J. P. Kruth, "Mechanical properties of AlSi10Mg produced by Selective Laser Melting," *Physics Procedia* , 2012.

[76] A. du Plessis, D. Glaser, H. Moller, N. Mathe , L. Tshabalala, B. Mfusi and R. Mostert, "Pore closure effect of laser shock peening of additively manufactured AlSi10Mg," 2019.

[77] S. Solutions, *Material Data Sheet Al Alloy AlSi10Mg,* SLM Solutions.

[78] A. H. Chilver and J. Case, Strenght of materials and structures, 2nd ed., London: Edward Arnold, 1971.

[79] R. C. Hibbeler, Mechanics of Materials, 2nd ed., Jurong: Prentice-Hall, 2005.

[80] R. C. Marshek and K. M. Juvinall, Fundamentals of machine component design, 3rd ed., Hoboken: John Wiley and sons, 2000.

[81] S. Nathan, "The engineer," 15 October 2015. [Online]. Available: https://www.theengineer.co.uk/aerospace-takes-to-additive-manufacturing/. [Accessed 11 November 2019].

[82] G. Electric, "What is additive manufacturing," General Electric, [Online]. Available: https://www.ge.com/additive/additive-manufacturing. [Accessed 15 November 2019].

[83] H. Technology, "Horizon Technology," Horizon Technology, 4 April 2019. [Online]. Available: https://www.horizontechnology.biz/blog/pros-and-cons-of-additive-manufacturing-vs-powder-metallurgy. [Accessed 15 November 2019].

[84] "SPI Lasers," [Online]. Available: https://www.spilasers.com/application-additive-manufacturing/selective-laser-sintering-and-melting/. [Accessed 1 Feb 2021].

[85] I. Gibson, D. Rosen and B. Stucker, Additive Manufacturing Technologies, New York: Springer, 2015.

[86] Bekkelund, "Fabricating metal objects using laser manufacturing technologies and powder metallurgy science," *Annals of CIRP,* vol. 46, no. 1, pp. 135-138, 1997.

[87] G. N. Levy, R. Schindel and J. P. Kruth, "Rapid manufacturing and rapid tooling with layer manufacturing (LM),state of the art and future perspectives.," *Annals of CIRP-Manufacturing Technology,* vol. 52, no. 2, pp. 589-609, 2003.

[88] P. F. Jacobs and D. T. Reid, Rapid prototyping and manufacturing: fundamentals of stereolithography, Dearborn, MI, USA: Society of Manufacturing Engineers., 1992.

[89] D. King and T. Tansey, "Rapid tooling: selective laser sintering injection tooling.," *Journal of Materials Processing Technology,* vol. 132, no. 1, pp. 42-48, 2003.

[90] F. R. Colins and J. H. Dudas, "Preventing weld cracks in high-strength aluminum," *Journal of welding,* vol. 45, p. 241, 1966.

Appendix A: AM Production

This section provides the CAD drawing used for the manufacture of the samples for the project.

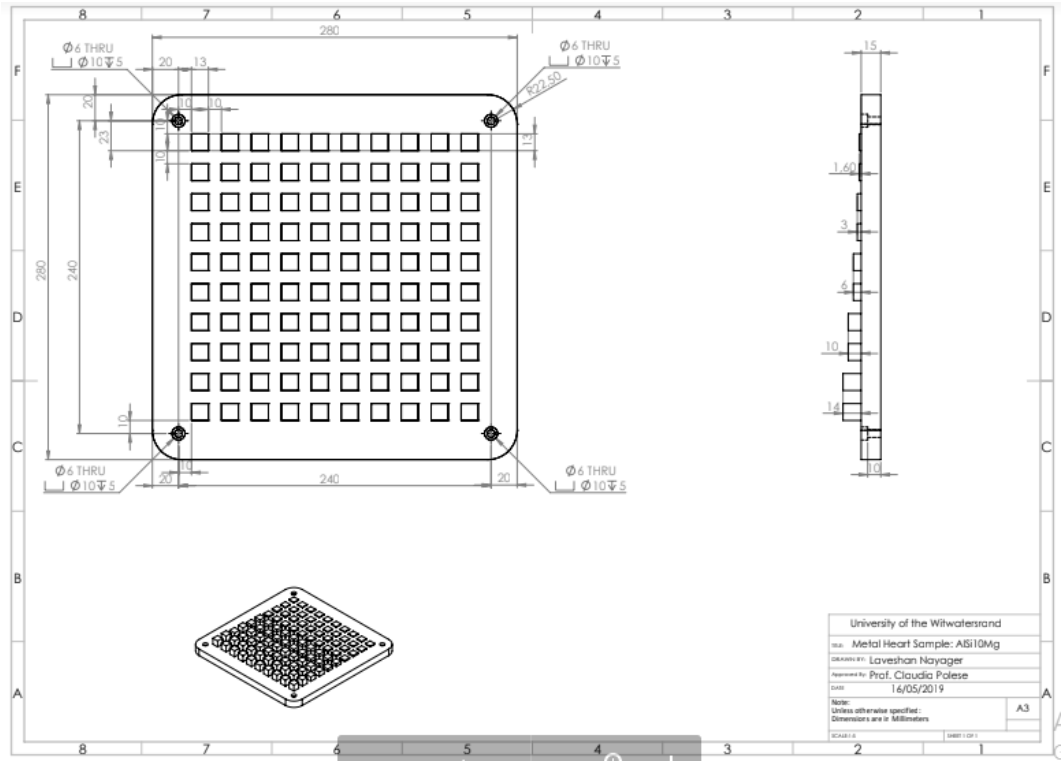

Figure 107: Manufacturing draw for AM samples

It is important to note the discrepancy between the manufactured drawing thickness and the actual manufactured thickness. This discrepancy was due to the plate being stuck within the machine during the SLM process. It is recommended that the width of the square baseplate be reduced to 277mm instead of 280mm while maintaining the bolt hole dimensions.

Appendix B: Laser Shock Peening Processing

This section shows the manufactured baseplate with Bosstick prestick applied to the gaps between the samples. The use of prestick was to mould the samples in such a way as to achieve laminar water flow over the samples during the LSP of the samples.

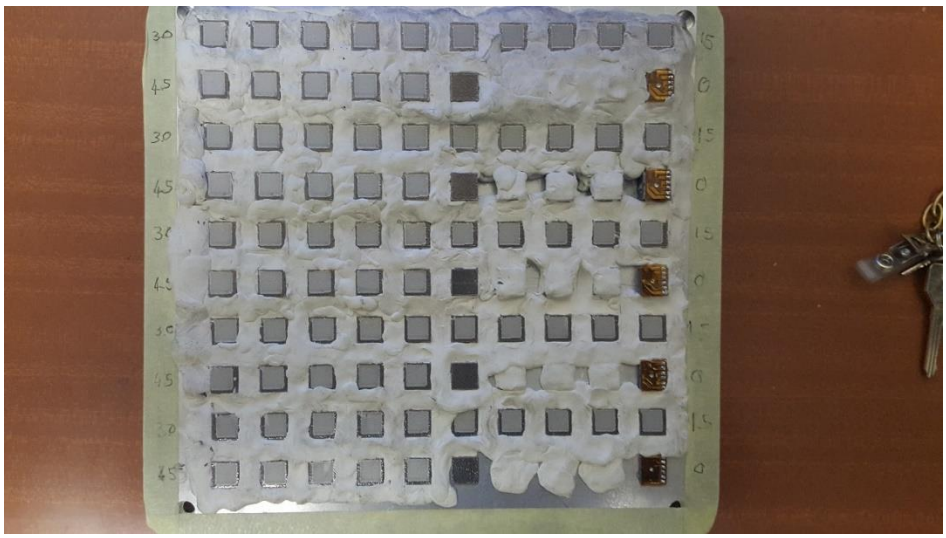

Figure 108: Samples after LSP

The following tables show the variation of the laser power during the processing of the samples. It must be noted that there was no major fluctuation as the processing of the samples occurred during the same day and weather effects were negligible.

Table 16: Laser energy for 1.2mm thick samples

Sample Thickness 1.2 mm			
Samples	Laser Energy [mJ]		
1	0,77	1,37	2,11
2	0,78	1,36	2,1
3	0,77	1,37	2,11
4	0,77	1,34	2,1
5	0,78	1,34	2,11

Table 17: Laser energy for 2.6mm thick sample

Sample Thickness 2.6 mm			
Samples	Laser Energy [mJ]		
1	0,77	1,35	2,08
2	0,76	1,36	2,08
3	0,77	1,35	2,09
4	0,76	1,36	2,09
5	0,76	1,34	2,1

Table 18: Laser energy for 5.6mm thick sample

Sample Thickness 5.6 mm			
Samples	Laser Energy [mJ]		
1	0,77	1,36	2,1
2	0,78	1,36	2,11
3	0,76	1,35	2,09
4	0,77	1,35	2,09
5	0,78	1,35	2,09

Table 19: Laser energy for 9.6mm thick samples

Sample Thickness 9.6 mm			
Samples	Laser Energy [mJ]		
1	0,77	1,36	2,1*
2	0,76	1,35	2,08
3	0,76	1,36	2,08
4	0,76	1,36	2,09
5	0,76	1,36	2,09

*Sample peened twice

Table 20: Laser energy for 13.6mm thick samples

Sample Thickness 13.6 mm			
Samples	Laser Energy [mJ]		
1	0,76	1,36	2,11
2	0,77	1,37	2,12
3	0,76	1,34*	2,1
4	0,77	1,32	2,1
5	0,75	1,36	2,1

*Sample peened twice

Appendix C: FESEM Images

This section provides the images that were taken using the FESEM at different magnifications in order to investigate the grain structure of the samples.

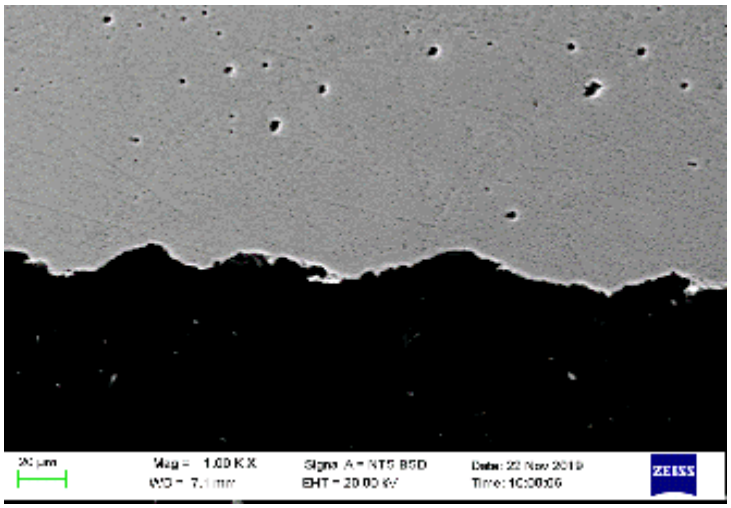

Figure 109: FESEM of 2.6mm 3.0 GW/cm² sample at 1000X magnification

The following image is a backscatter image of 2.6mm thick 4.5 GW/cm² sample

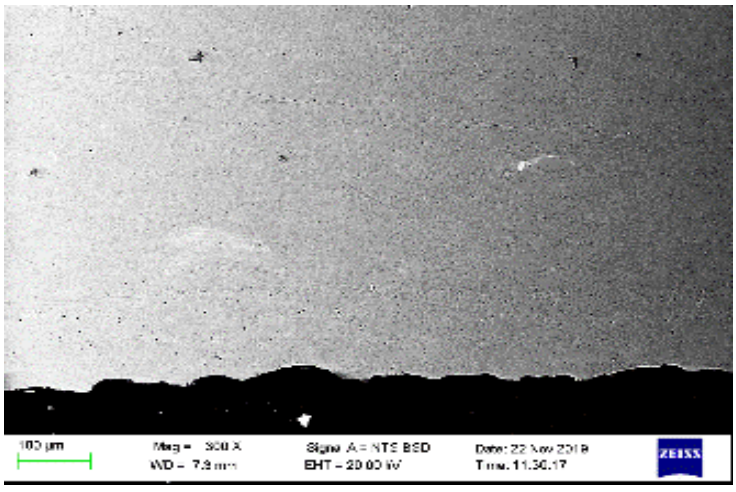

Figure 110: FESEM of 2.6mm 4.5 GW/cm sample at 200X magnification

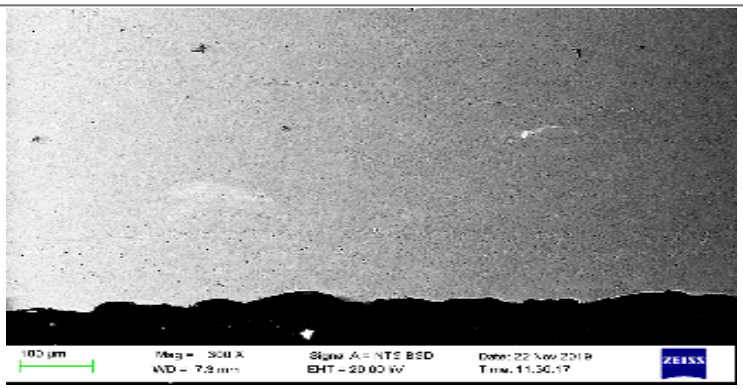

Figure 111: FESEM of 2.6mm 4.5 GW/cm sample at 200X magnification

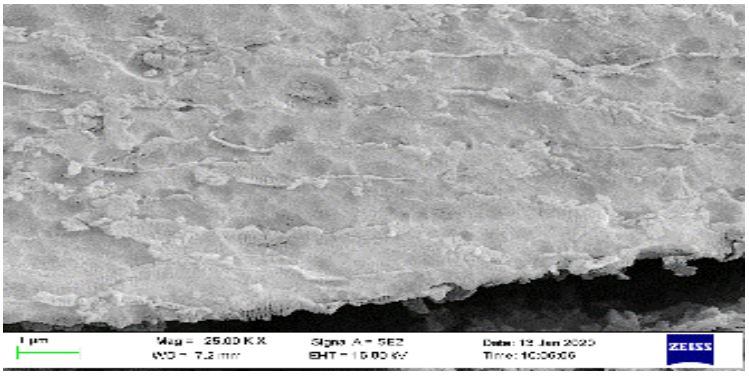

Figure 112: FESEM of 2.6mm 1.5 GW/cm sample at 20kX magnification

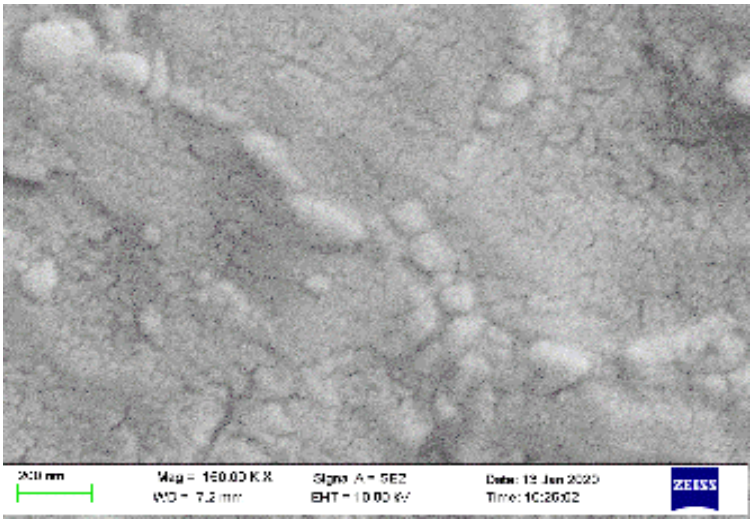

Figure 113: FESEM of 2.6mm 1.5 GW/cm sample at 160kX magnification

Appendix D: Microhardness Testing Values

This section provides the raw data of the hardness testing machine.

Table 21: Hardness values of 1.2mm thick sample

1.2 mm Hv				
Indent	As-built	1.5 GW/cm²	3.0 GW/cm²	4.5 GW/cm²
1	102,1	107	99,3	104,5
2	111,1	165,3	119	106,5
3	109,4	152	135,1	128,8
4	139,4	152,1	129,6	124,2
5	139,7	141,3	122	128,7
6	139,8	139,3	126	129,8
7	139,3	129,7	122,2	126
8	133,3	145,3	122,6	143,5
9	133,3	113,3	119	143,4
10	122,4	111,1		126,5
11	114			112,3

Table 22: Hardness values of 2.6mm thick sample

2.6mm Hv				
Indent	As-built	1.5 GW/cm²	3.0 GW/cm²	4.5 GW/cm²
1	111,5	144,7	103,7	114,9
2	124,4	136,1	102	114,4
3	128,6	131,3	106,4	120,1
4	126,9	121,4	117,5	116,9
5	134,7	120,6	115,8	113,2
6	126,8	120,2	118,8	118,1
7	126,7	119,5	123,7	117,9
8	127	119,3	123,9	116,5
9	138,8	115,3	126,5	118,9
10	136,6	111,5	122,6	116,3
11	128,5	113,5	125,7	117,4
12	127,4	115	120,3	115,5
13	136	116,2	119,4	119,2
14	136	117,1	122,2	122,1
15	131,5	132,1	124,2	77
16	129,7	117,4	126,7	128,4
17	134,2	107,5	128,6	126,2

18	94	106,4	132,3	125
19	111,9		116,1	111,3
20	113,2			
21	109,8			
22	109,6			
23	111,4			
24	110,6			
25	109,8			

Table 23: Hardness values of 5.6mm thick sample

5.6mm Hv				
Indent	As-built	1.5 GW/cm²	3.0 GW/cm²	4.5 GW/cm²
1	121,8	123,8	83	122,5
2	119,6	107,2	127,1	128,6
3	132,7	128,5	131,7	145,7
4	122,4	133,5	132,5	106,3
5	126,2	131,6	134,3	136,5
6	121,8	138,3	126,6	134,9
7	121,3	146	149,4	146,1
8	120,8	145,4	137,2	133,2
9	120,9		141,2	133,6
10	122,5		133,6	126
11	116		133	126,3
12	110,9		133,1	132,3
13	113,3		126,8	130,9
14	112,5		136,8	131,6
15	124		135	129,1
16	124		121,1	134,8
17	116,8		125,8	126,6
18	115,6		121,9	133,7
19	121,2		130,1	134,6
20	121		140,3	132,9
21	114,9		141,6	131,1
22	115,6		138	147,7
23	122,5		144,4	133,3
24	122,5		132	147,7
25	129,5		137	137,5
26	125,7		140,2	133,1
27	135,6		126,4	139,2
28	133,7		143,4	129,4
29	134,5		138,9	145,3

30	127,2		130,7	132,8
31	140,9		133,3	131,6
32	147,5		130,7	131,2
33	137		133,4	128,6
34	135,4		126,4	134,3
35	140,4		118,6	118,8
36	129,6		121,3	112,5
37	129,6		123,1	112,2
38	135		114,4	
39	130,8		119,2	
40	134,1		109,2	
41	137,4			
42	132,1			
43	130,8			

Table 24: Hardness values of 9.6mm thick sample

9.6mm Hv				
Indent	As-built	1.5 GW/cm²	3.0 GW/cm²	4.5 GW/cm²
1	115,2	122,5	94,5	132,9
2	115,2	123,7	108,8	130,4
3	120,3	128,6	114,1	126
4	123,3	125,7	112,6	129,3
5	104,1	139,8	116,7	128,6
6	120,5	144,2	109,2	130,2
7	120,6		111	128,9
8	129,4		108,4	128,5
9	129,5		110,3	126,8
10	138,6		110	128,1
11	122,8		106,7	124,1
12	126,5		109	120,7
13	127,5		109	127,2
14	124,6		112,5	126,2
15	119,3		111,9	126,9
16	109,6		111,5	126
17	112,7		97	123,7
18	119,2		113,6	123,9
19	118		106,6	
20	114,4		110,6	
21	111,8		107,9	

Table 25:Hardness values of 13.6mm thick sample

13.6mm Hv				
Indent	As-built	1.5 GW/cm²	3.0 GW/cm²	4.5 GW/cm²
1	126,3	121,5	156,9	147,2
2	131,9	129,1	165,1	130,5
3	95,5	131	159	130,5
4	126,8	128,6	158,3	124,7
5	104,9	122,8	143,4	129,4
6	125,4	122,6	145,2	133,5
7	125	121,3	143,7	134,3
8	120,5	120,3	143,9	131,9
9	123,8	120,3	148,5	132,3
10	117,3	125,9	144,1	124,7
11	120,2	119,2	144,5	128
12		124,2	142,8	131,1
13		120,5	145,6	130,5
14		120,5	146,8	116,4
15		120,5	146	107,7
16		152,6	135,3	

Appendix E: Incremental Hole Drilling Results

This section provides the IHD results in tabulated format

Table 26: IHD values of 1.2mm thick samples

1,2mm Sigma max				
Depth [mm]	As-built	1.5 GW/cm²	3.0 GW/cm²	4.5 GW/cm²
0,025	357,266	71,17	-113,377	19,703
0,075	280,124	6,676	-139,23	-58,829
0,125	276,125	-47,003	-140,723	-122,028
0,175	280,015	-82,896	-114,642	-157,415
0,225	309,01	-91,154	-84,684	-172,69
0,275	314,455	-86,797	-70,238	-178,017
0,325	255,062	-77,019	-63,031	-180,399
0,375	202,233	-65,308	-47,471	-181,501
0,425	228,577	-55,95	-30,931	-178,371
0,475	281,143	-43,646	-29,47	-169,506
0,525	251,432	-22,75	-37,525	-156,233
0,575	202,151	3,732	-35,225	-140,975
0,625	204,553	25,468	-22,531	-127,218
0,675	216,904	37,782	-11,884	-116,89
0,725	201,403	45,346	-7,52	-107,365
0,775	182,908	53,738	-5,014	-93,931

Table 27: IHD values of 2.6mm thick sample

2,6mm Sigma max				
Depth [mm]	As built	1.5 GW/cm²	3.0 GW/cm²	4.5 GW/cm²
0,025	175,535	-40,972	11,261	-135,542
0,075	215,154	-65,696	-45,481	-184,909
0,125	251,626	-78,931	-98,172	-153,36
0,175	271,379	-76,844	-133,816	-132,421
0,225	266,294	-59,763	-147,535	-128,404
0,275	248,522	-47,07	-146,855	-120,594
0,325	233,471	-42,969	-141,313	-97,971
0,375	222,159	-38,727	-137,556	-73,876
0,425	213,272	-31,626	-134,798	-62,046
0,475	208,396	-22,994	-129,077	-56,077
0,525	207,65	-11,226	-120,062	-46,168

0,575	209,339	5,83	-108,421	-27,679
0,625	210,173	25,685	-93,608	-3,749
0,675	207,683	41,505	-78,14	3,62
0,725	204,833	46,238	-65,555	-13,895
0,775	204,592	38,512	-55,448	-26,218

Table 28: IHD values of 5.6mm thick sample

5,6mm Sigma max				
Depth [mm]	As built	1.5 GW/cm²	3.0 GW/cm²	4.5 GW/cm²
0,025	35,08	8,654	21,838	34,524
0,075	204,068	-37,348	-45,339	-55,179
0,125	294,998	-79,833	-89,266	-141,063
0,175	301,177	-94,729	-120,741	-190,22
0,225	298,977	-86,461	-139,934	-197,357
0,275	297,5	-73,379	-146,136	-189,164
0,325	290,946	-65,318	-144,313	-192,115
0,375	279,407	-62,296	-141,022	-198,926
0,425	264,086	-60,508	-137,465	-188,229
0,475	254,782	-55,46	-131,455	-161,897
0,525	254,454	-44,824	-120,421	-142,428
0,575	250,62	-25,179	-104,633	-136,391
0,625	238,603	6,44	-88,461	-133,247
0,675	229,783	41,192	-75,821	-124,059
0,725	228,672	63,753	-65,851	-112,344
0,775	226,443	67,581	-56,594	-102,876

Table 29: IHD values of 9.6mm thick sample

9,6mm Sigma max				
Depth [mm]	As built	1.5 GW/cm²	3.0 GW/cm²	4.5 GW/cm²
0,025	49,372	-101,358	17,648	34,524
0,075	151,969	-68,692	-44,431	-55,179
0,125	181,395	-46,332	-100,008	-141,063
0,175	204,891	-35,803	-138,67	-190,22
0,225	223,253	-29,956	-155,314	-197,357
0,275	236,045	-19,184	-153,74	-189,164
0,325	234,15	-2,767	-140,244	-192,115
0,375	234,514	-14,638	-122,753	-198,926

0,425	237,775	-32,753	-108,262	-188,229
0,475	229,161	-34,829	-98,955	-161,897
0,525	219,351	-26,243	-92,441	-142,428
0,575	220,747	-18,919	-85,607	-136,391
0,625	214,09	-10,275	-76,805	-133,247
0,675	185,152	0,139	-65,471	-124,059
0,725	163,859	16,311	-52,111	-112,344
0,775	171,243	40,608	-38,855	-102,876

Table 30: IHD values of 13.6mm thick sample

13,6mm Sigma max				
Depth [mm]	As built	1.5 GW/cm²	3.0 GW/cm²	4.5 GW/cm²
0,025	140,418	19,735	-13,155	-0,564
0,075	149,895	14,039	-102,074	-77,643
0,125	163,532	4,871	-153,453	-132,255
0,175	179,637	-17,041	-151,351	-165,12
0,225	193,978	-55,515	-135,892	-170,491
0,275	205,07	-91,64	-128,967	-154,931
0,325	209,216	-110,228	-120,601	-140,908
0,375	205,795	-112,55	-105,116	-136,25
0,425	200,92	-106,075	-88,053	-135,895
0,475	200,024	-98,064	-72,828	-131,639
0,525	205,011	-91,455	-58,461	-116,593
0,575	219,132	-84,741	-45,705	-92,441
0,625	240,716	-74,141	-38,875	-72,534
0,675	255,499	-56,532	-32,173	-67,725
0,725	257,133	-33,716	-22,937	-70,721
0,775	272,046	-10,957	-13,765	-66,544

Appendix F: Contribution To Knowledge

TAILORING RESIDUAL STRESS PROFILES AND SURFACE FINISH OF AERONAUTICAL ADDITIVE MANUFACTURED PARTS BY LASER SHOCK PEENING

L. Nayager[1] & C. Polese[1, 2*]

[1]School of Mechanical, Industrial and Aeronautical Engineering, University of the Witwatersrand, South Africa

[2]DST-NRF Centre of Excellence in Strong Materials, University of the Witwatersrand, South Africa, Claudia.Polese@wits.ac.za

ABSTRACT

Aluminium alloy AlSi10Mg samples were manufactured by Selective Laser Melting in various thicknesses of 1.2 mm, up to 13.6 mm and then surface treated with Laser Shock Peening, with 3 different power intensities of 1.5 GW/cm^2, 3.0 GW/cm^2 and 4.5 GW/cm^2 and a fixed spot diameter of 1 mm. The residual stresses were measured using the Incremental Hole Drilling technique following the ASTM E837-13a standard. The results compared favourably and it was concluded that Laser Shock Peening had not only the beneficial effect of removing the tensile residual stress of the as-built samples, but also inducing compressive residual stress.

INTRODUCTION

It has been observed that during the additive manufacturing process by Selective Laser Melting (SLM) the material deforms, warps or cracks due to tensile residual stress [1, 2, 3, 4]. Laser Shock Peening (LSP) is a surface treatment method that induces in metal components beneficial compressive residual stress that penetrate deeper than other conventional surface treatments such as shot peening [5] and it has been investigated extensively for different wrought alloys, e.g. aluminium, titanium and tool steels. Therefore the adverse tensile residual stress within an additive manufactured aeronautical component can potentially be entirely removed or reduced by LSP [6]. However, optimised LSP parameters, e.g. Power Intensities (PI), spot size, coverage and scanning strategy, have still to be identified to achieve high compressive residual stresses at large depths within aeronautical additive manufactured alloys.

METHODOLOGY AND RESULTS

SLM AlSi10Mg samples of varying thicknesses were LSPeened with PI of 1.5 GW/cm^2, 3.0 GW/cm^2 and 4.5 GW/cm^2, with a fixed round spot diameter of 1 mm, 70% overlap using raster scanning strategy. Residual stresses were measured by the Incremental Hole Drilling (IHD) method using a SINT Technologies MTS3000-Restan system, while following the ASTM E837-13a standard [7]. The residual stresses profiles in the thickness direction, see the following graphs, were calculated using the extended, non-uniform procedure with the Tikhonov correction factor applied. The results were processed using EVAL 7.16 software commercially available from SINT Technologies.

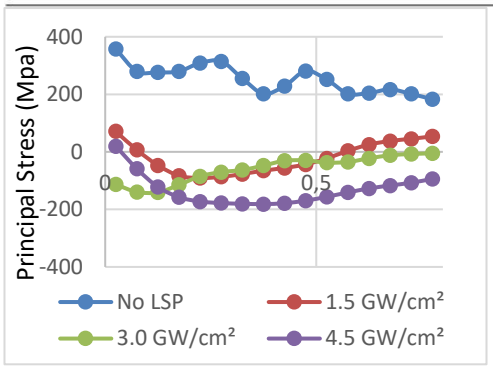

Figure 1: Residual stress profile for 1.2 mm

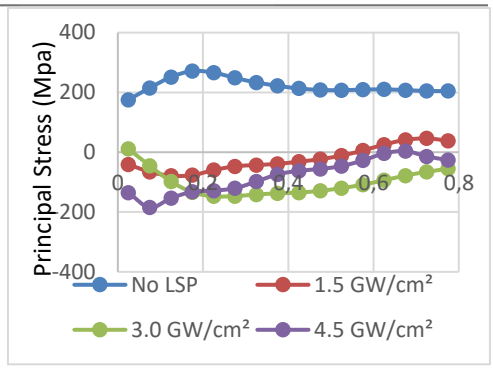

Figure 2: Residual stress profile for 2.6 mm

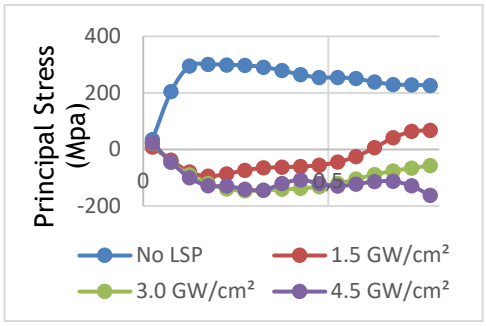

Figure 3: Residual stress profile for 5.6 mm

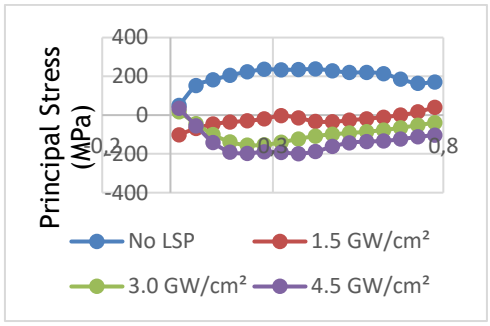

Figure 4: Residual stress profile for 9.6 mm

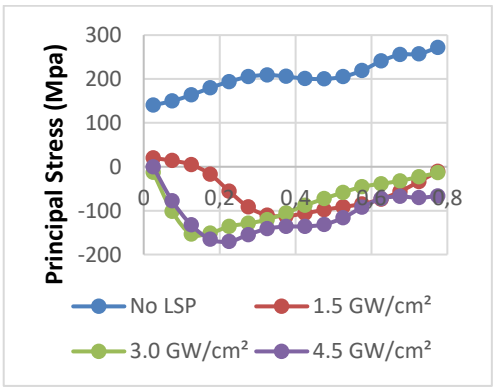

Figure 5: Residual stress profile for 13.6mm

CONCLUSION

From the results obtained so far it has been found that LSP, irrespective of the LSP power intensity values, not only removed the tensile residual stress, but it also induced beneficial compressive residual stress. The as-built samples had an average maximum tensile residual stress of 275 MPa. After the surface treatment the residual stress was altered to a compressive state with a minimum

average value of -198MPa. Further surface integrity and microstructure investigations, i.e. surface roughness measurements, Scanning Electron Microscopy, Vickers microhardness testing, are currently underway as well as comparative residual stress measurements, i.e. X-ray Diffraction testing.

REFERENCES

[1] Kempen, K., Vrancken, B., Buls, S., Thijs, L., Van Humbreeck, J., Kruth, J. P. 2014. Selective laser melting of crack-free high density M2 high speed steel parts by baseplate preheating, *Journal of Manufacturing Science and Engineering*, 136(6), pp 061026_1-6.

[2] Alimardani, M., Toyserkani, E., Huissoon, J. P., Paul, C. P. 2009. On the delamination and crack formation in a thin wall fabricated using laser solid freeform fabrication process, *Optics and Lasers in Engineering,* 47(11), pp 1160-1168.

[3] Olakanmi, E. O., Cochrane, R. F., Dalgarno, K. W. 2015. A review on selective laser sintering/melting (SLS/SLM) of aluminium alloy powders, *Progress in Materials Science*, 74, pp 401-477.

[4] Vrancken, B., Cain, V., Knutsen R., Van Humbeeck J. 2014. Residual stress via the contour method in compact tensions specimens produced via selective laser melting, *Scripta Materialia*, 87, pp 29-32.

[5] Kalentics, N., Boillat, E., Peyre, P., Ciric-Kostic S., Bogojevi N., Loge, R. E. 2017. Tailoring residual stress profile of Selective Laser Melted parts by Laser Shock Peening, *Additive Manufacturing*, 16, pp 90-97.

[6] Charles T. W., Montross S. 2002. Laser shock processing and its effects on microstructure and properties of metal alloys: a review, *Internation Journal of Fatigue*, 24(10), pp 1021-1036.

[7] ASTM E837-13a 2013. Standard Test Method for Determining Residual Stresses by the Hole-Drilling Strain-Gage Method, *ASTM International*, 03.01.